PHENOMENA AND MECHANISMS OF PHOTOVOLTAIC EFFECTS IN FERROELECTRIC $BiFeO_3$ THIN FILMS

JI WEI

(B. Eng.) Nanyang Technological University

A THESIS SUBMITTED

FOR THE DEGREE OF DOCTOR OF PHILOSOPHY

DEPARTMENT OF ELECTRICAL & COMPUTER ENGINEERING

NATION UNIVERISTY OF SINGAPORE

2013

Acknowledgements

I would like to acknowledge those who have helped to make this project possible.

Foremost, to my supervisor Associate Professor Yung C. Liang and co-supervisor Dr. Yao Kui, I would like to express my sincere thanks for their advice, encouragement, and support throughout this project.

I would like to thank all the staff members in Dr. Yao Kui's group, including Ms. Gan Bee Keen, Ms. Alicia Huang, Dr. Goh Poh Chin, Dr. Tan Chin Yaw, Ms. Tan Sze Yu, Ms. Christina Tan, Mr. Chen Yifan, Dr. Santiranja Shannigrahi, Dr. Premnath Ramesh Nath, Ms. Oh Su Yin, Dr. Lim Yee Fun, and Mr. Tan Chee Kiang, for the fruitful discussions and help.

I would like to acknowledge the fabrication and characterization support from the SnFPC of IMRE. I would also like to thank the staff in IMRE for their assistance and help. I would specially thank Mr. Lim Poh Chong, Mr. Chum Chang Choy, Mr. Wang Weide, Ms. Teo Siew Lang, Ms. Lai Doreen, Ms. Shen Lu, and Dr Ke Lin for their technical assistance.

Finally, I would like to express my gratitude to my parents and my wife who have been behind me at every stage, providing unwavering support.

Table of Contents

Summary

Ferroelectric materials exhibit unique photovoltaic (PV) properties, including photovoltages that can be much larger than the bandgap of the material and switchable photocurrents. Although previous studies in ferroelectric bulk materials showed very limited PV efficiencies, recent reports suggest that the PV efficiency can be significantly enhanced in ferroelectric thin films. However, very little was understood about the PV effects in the ferroelectric thin film. Ferroelectric $BiFeO_3$ (BFO), with a large remanent polarization and a bandgap corresponding to the visible spectral region, is a suitable material for the studies on the mechanisms of PV effects in ferroelectric materials and for the development of potential energy harvesting devices. Furthermore, as the only known single phase multiferroic material at room temperature, the PV effect in BFO could be used in conjunction with other effects in novel multifunctional devices. In this study, high quality epitaxial BFO films are fabricated by sputter deposition. The PV property of the BFO films and its mechanisms are systematically investigated.

It is found that both the ferroelectric depolarization field and the bulk photovoltaic effect play a role in the observed photovoltaic responses in the BFO thin films. In a sandwich structure, the ferroelectric-electrode interfaces show Fermi level pinning and form back-to-back Schottky barriers. The Schottky barrier height is insensitive to the ferroelectric polarization, but the direction of the photovoltaic current can be switched by poling the films in different directions.

The study also clearly shows the existence of the bulk photovoltaic effect (BPVE) in ferroelectric thin films. By measuring the photocurrent in the plane perpendicular to the ferroelectric polarization with symmetric electrodes, the effect of the

depolarization field and interfacial energy barriers are eliminated. For the first time, evidence of a strong BPVE is shown in epitaxial BFO films as thin as 40 nm. The bulk photovoltaic tensor coefficient β_{22} in BFO is obtained. Remarkably it is about five orders of magnitude larger than that of other typical ferroelectric materials such as $LiNbO_3$:Fe and $LiTaO_3$ at visible light wavelength.

The results show that both depolarization field and the BPVE contribute to the observed PV processes in BFO films with sandwich structures. The photocurrents from these two mechanisms in BFO are probably opposite to each other and partially cancel out. This could be one of the factors that limit the efficiency in these samples.

The photoelectrolytic reaction of water splitting using BFO as the photoelectrode is investigated. Significant anodic photocurrents are observed. A possible monolithic water splitting cell based on BFO is proposed.

The results from this study show that the PV effects in ferroelectric materials can be used to achieve unique functionalities in novel devices, and even possibly contribute to energy harvesting.

List of Publications

W. Ji, K. Yao, Y. C. Liang, "Bulk photovoltaic effect at visible wavelength in epitaxial ferroelectric $BiFeO_3$ thin films," *Adv. Mater.*, vol. 22, pp. 1763-1766, 2010.

W. Ji, K. Yao, Y. C. Liang, "Evidence of bulk photovoltaic effect and large tensor coefficient in ferroelectric $BiFeO_3$ thin films," *Phys. Rev. B*, vol. 84, pp. 094115, 2011.

W. Ji, K. Yao, Y. C. Liang, "Photovoltaic properties of epitaxial ferroelectric $BiFeO_3$ thin films," *IMF-12 & ISAF-18*, Xi'an, China, 2009. [Oral Presentation]

W. Ji, K. Yao, Y. C. Liang, "Evidence of bulk photovoltaic effect in $BiFeO_3$ ferroelectric thin films," *ISIF 2012*, Hong Kong, China, 2012. [Poster]

List of Figures

List of Tables

List of Abbreviations

Materials

a-Si	Amorphous silicon
a-Si:H	Hydrogen-passivated amorphous silicon
BHF	Buffered hydrofluoric acid
BFO	$BiFeO_3$
c-Si	Crystalline silicon
SRO	$SrRuO_3$
STO	$SrTiO_3$
LNO	$LiNbO_3$
LAO	$LaAlO_3$
BTO	$BaTiO_3$
PTO	$PbTiO_3$
ITO	Tin-doped indium oxide
FTO	Fluorine-doped tin oxide
PZT	$Pb(ZrTi)O_3$
YSZ	Yttria-stabilized zirconia
PLWZT	WO_3-modified $(Pb_{0.97}La_{0.03})(Zr0_{.52}Ti_{0.48})O_3$
PVA	Polyvinyl alcohol

Acronyms

AC	Alternating current
AFM	Atomic force microscopy
AM	Air mass
BPVE	Bulk photovoltaic effect
DC	Direct current
DSSC	Dye-sensitized solar cell

FWHM	Full-width at half-maximum
FRAM	Ferroelectric random access memory
F.C.S.	Franck-Condon state
FESEM	Field emission scanning electron microscopy
G.S.	Ground state
MIGS	Metal-induced gap state
LSV	Laser scanning vibrometer
PSPD	Position-sensitive photodiode
PV	Photovoltaic
QNR	Quasi-neutral region
R.E.S.	Relaxed excited state
RF	Radio frequency
RSM	Reciprocal space mapping
SCR	Space charge region
UBM	Short form for Nanofilm Unbalanced Magnetron Sputtering System
XPS	X-ray photoelectron spectroscopy
XRD	X-ray diffraction

Parameters

A	Area
A^*	Richardson constant
$\vec{a}$	Basis vector
a_o	In-plane lattice constants of the fully-relaxed material
$a_{//}$	In-plane lattice constants of the strained material
abs	Absorbance
D	Electric flux density
d	Lattice spacing
d_{33}	Longitudinal piezoelectric coefficient

E	Electric field
E_b	Built-in field at the bottom electrode interface
E_t	Built-in field at the top electrode interface
E_{bi}	Built-in field
E_c	Coercive field
E_{oc}	Open-circuit electric field
E°	Standard electrode potential
e	Euler's number
$\hat{e}$	Unit vector
e_i	Directional cosine of the optical electric field along the i^{th} axis
F	Faraday's constant
G	Glass coefficient
G°	Standard Gibbs free energy
ΔG°	Change of standard Gibbs free energy
h	Planck constant
I	Current
I_L	Light intensity
$\hat{i}$	Unit vector of the i^{th} axis
J	Current density
J_d	Displacement current density
J_e	Photocurrent density due to excitation
J_r	Photocurrent density due to recombination
$J_{P\text{-}F}$	Poole-Frenkel emission current density
J_{SCLC}	Space charge limited current density
J_{SC}	Fowler-Nordheim tunneling current density
J_s	Reverse saturation current density
J_{sc}	Short-circuit photocurrent density
J_{OR}	Optical rectification current density
k	Extinction coefficient

k_B	Boltzmann constant
k_{wn}	Wavenumber
k_o	Ordinary wavenumber
k_e	Extraordinary wavenumber
k_{vac}	Wavenumber in vacuum
l	Electrode gap
m^*	Effective electron mass
N_A	Avogadro constant
n	Refractive index
n_o	Ordinary refractive index
n_e	Extraordinary refractive index
n_i	Ideality factor
P	Polarization
P_r	Remanent polarization
P_s	Saturated polarization
P_t	Period
Q_{GS}	Gap state charges
q	Elementary charge
$\vec{R}$	Lattice vector
R_a	Root-mean-square roughness
S	BPVE photocurrent oscillation period
s	Length of electrode
T	Absolute temperature
T_c	Curie temperature
T_N	Néel temperature
t	Time
V_{bi}	Built-in potential
V_{OC}	Open-circuit voltage
$V_{OC,p}$	Switchable component of the photovoltage

$V_{OC,bi}$	Unswitchable component of the photovoltage
V_{+}	Open-circuit voltage after positive poling
V_{-}	Open-circuit voltage after negative poling
Z	Atomic number
a, b, c	Crystallographic axes
x, y, z	Cartesian axes
α	Absorption coefficient
$\boldsymbol{\alpha}$	Transformation matrix
β	Bulk photovoltaic effect tensor coefficient
δ	Thickness
ε	Energy
ε_c	Minimum of conduction band
ε_g	Bandgap energy
ε_v	Maximum of valence band
ε_F	Fermi level
ε_{Fn}	Quasi-Fermi level for electrons
ε_{Fp}	Quasi-Fermi level for holes
ε_r	Complex relative dielectric constant
ε'	Real part of the relative dielectric constant
ε''	Imaginary part of the relative dielectric constant
ε_0	Vacuum permittivity
ε_a	Dielectric constant perpendicular to the polar axis
ε_c	Dielectric constant parallel to the polar axis
ε_∞	Optical frequency dielectric constant
ε_s	Epitaxial strain
ω	Angular frequency
λ	Wavelength
λ_{vac}	Wavelength in vacuum
λ	Wavelength

η	Piezoelectric dilation
σ	Conductivity
μ	Charge mobility
τ	Charge lifetime
χ_{ijk}	Second-order nonlinear optical susceptibility
Φ_{B}	Barrier height
Φ_{t}	Trap ionization energy
Φ_{SB}	Schottky barrier height

Chapter 1. Introduction

1.1. Ferroelectric materials

Ferroelectrics constitute an important family of functional materials. Many of the materials in this group exhibit a variety of useful properties, such as high dielectric constants and large piezoelectric coefficients. As a result, they have found applications in numerous areas, including sensors, actuators, electro-optic devices, nonvolatile memories and many other integrated systems [1-3].

This research work focuses on the photovoltaic (PV) effect in ferroelectrics, motivated by the demand for new mechanisms for device functions and energy harvesting. Hopefully the knowledge gained through this work will advance our understanding and even lead to new device applications.

1.1.1. Properties of ferroelectrics

The defining feature of a ferroelectric is a spontaneous switchable bi-stable electric polarization. Under a zero electric field, a ferroelectric material possesses two or more discrete stable or metastable states of nonzero electric polarization, which can be switched with an applied electric field [4]. Neumann's Principle states that the symmetry of any physical property of a crystal must include the symmetry elements of the point group of the crystal. Consequently, ferroelectricity can only exist in a polar material. There are 32 crystallographic point groups, of which 11 are centrosymmetric. The remaining 21 groups do not possess a center of symmetry. With the exception of the point group 432 (the Hermann-Mauguin notation is adopted in this thesis), they all show piezoelectricity (i.e., the generation of electricity by mechanical pressure or vice versa). Ten out of these 21 point groups, 1, 2, m, mm2, 3,

3m, 4, 4mm, 6, 6mm, plus the two Curie group of ∞m and ∞, have a unique rotational axis without any mirror plane perpendicular to this axis. As a result, the atomic arrangement at one end of this rotational axis is different from the other. Materials of these polar point groups show pyroelectricity, where the electric polarization under zero electric field (i.e., spontaneous polarization) changes in response to a change in the temperature. If the polarization direction of a pyroeletric material can be switched by an external electric field, it falls under the category of ferroelectrics.

The switching of the spontaneous polarization is a key signature of ferroelectricity. Experimentally it can be observed as a polarization-electric field (*P*-*E*) hysteresis loop. An example of the *P*-*E* hysteresis loop is shown in Fig. 1.1 [5]. In the virgin state, a ferroelectric material usually contains domains in random orientations and thus does not possess a macroscopic polarization (point A). Under an external electric field, domains will be switched until all have been aligned in the direction of this external field (point C). Further increase of the field strength does not induce any more domain switch but only a linear dielectric response (point C to D). The intercept of the extrapolated line CD on the polarization axis is the saturated polarization P_s. When the external field is returned to zero, the polarization falls to point E, below P_s. The polarization at zero field is the remanent polarization P_r. It is usually smaller than the P_s due to the partial back-switch of the domains. The same process of domain switching occurs when the external field is applied in the opposite direction. The field strength at which the ferroelectric domain switching occurs is called the coercive field E_c. Domain switching takes place by nucleation of domains and the movement of domain walls [6]. This process is affected by many factors and thus E_c can differ significantly among different measurements and different samples of the same

material. In particular, it is found that E_c scales with the thickness δ in ferroelectric films according to $E \propto \delta^{-2/3}$ [7].

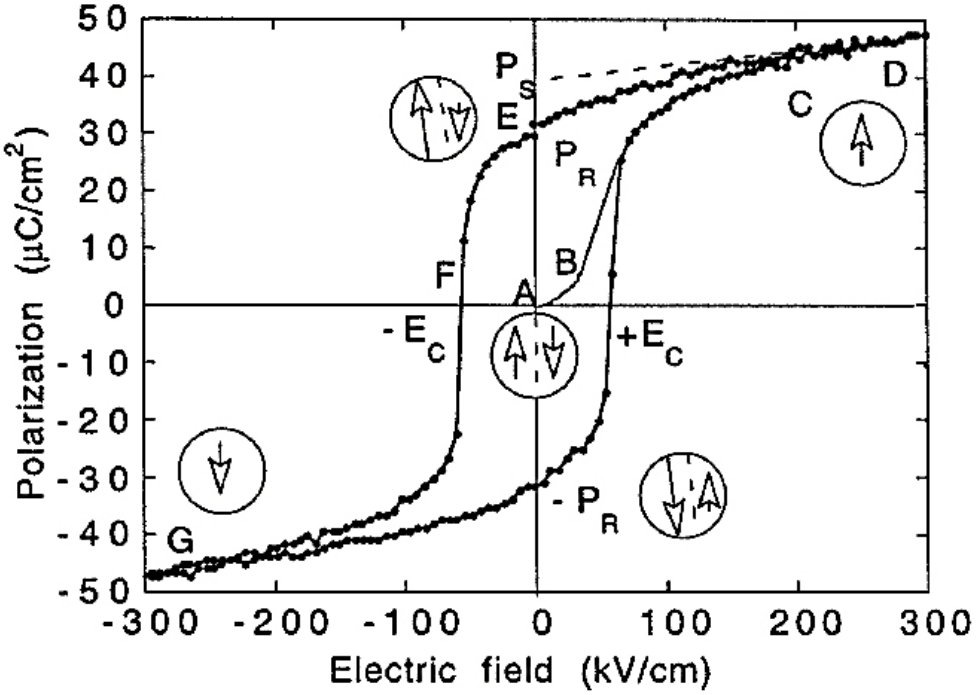

Figure 1.1 Ferroelectric *P-E* hysteresis loop. Arrows denote the polarization vectors in ferroelectric domains [5].

The spontaneous polarization in ferroelectric materials is produced by the atomic arrangement of ions in the crystal structure. For the material to exhibit discrete polarization states, and for this polarization to be switchable by an external field, it is often the case that the polar crystal structure can be obtained as a "small" symmetry-breaking distortion of a higher-symmetry reference state [4]. One such reference state is the cubic perovskite structure (space group $Pm\bar{3}m$) with the general chemical formula ABO_3, where A is a cation with a larger ionic radius at the eight-fold coordinated [000] site, B a cation with a smaller ionic radius at the octahedrally coordinated [0.5 0.5 0.5] site, and O represents oxygen at face centers forming an octahedron (Fig. 1.2) [1]. The perovskite family contains some of the most studied

and technologically important ferroelectric materials, such as $BaTiO_3$ (BTO) and $Pb(Zr_xTi_{1-x})O_3$ (PZT).

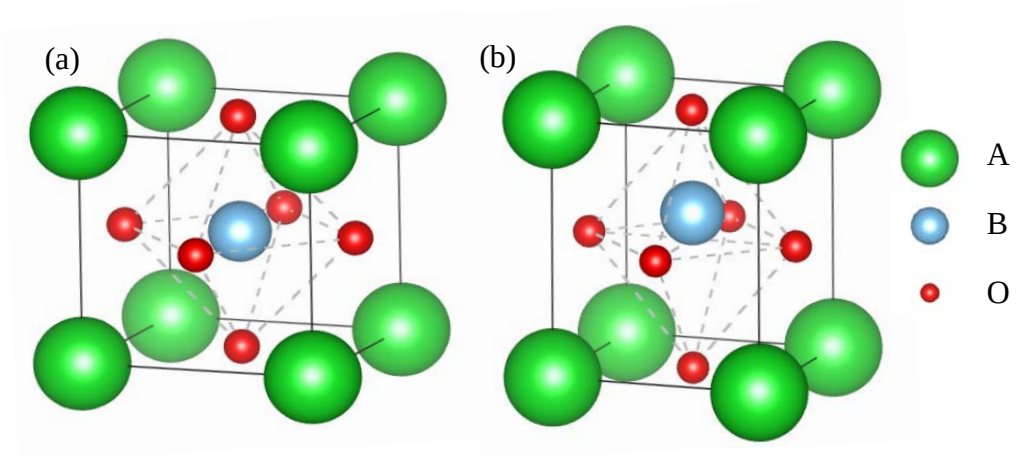

Figure 1.2 (a) Perovskite structure ABO_3 with the oxygen octahedron in the center. (b) Tetragonal distortion to the perovskite structure where anions and cations are displaced relative to each other along the polar axis. (adapted from Ref. [3])

Perovskite ferroelectric materials undergo phase transitions from the reference cubic perovskite state at high temperatures to lower-symmetry ferroelectric states at lower temperatures. The cations and anions are displaced relative to each other in the ferroelectric state to produce a net electric dipole. The temperature where the paraelectric-ferroelectric phase transition occurs is the Curie temperature T_c. The paraelectric-ferroelectric phase transition can be understood in the picture of the classic "soft mode" (Fig. 1.3) [8]. Upon cooling through the phase transition temperature, a normal mode of a phonon goes "soft" and condenses to a finite frozen amplitude. In the ferroelectric state, there is an energy barrier between the two ground levels and the ions are trapped inside one of them, leading to a nonzero electric dipole. This dipole can be switched by applying an electric field, which pushes the ions to overcome this barrier and move into the other energy well.

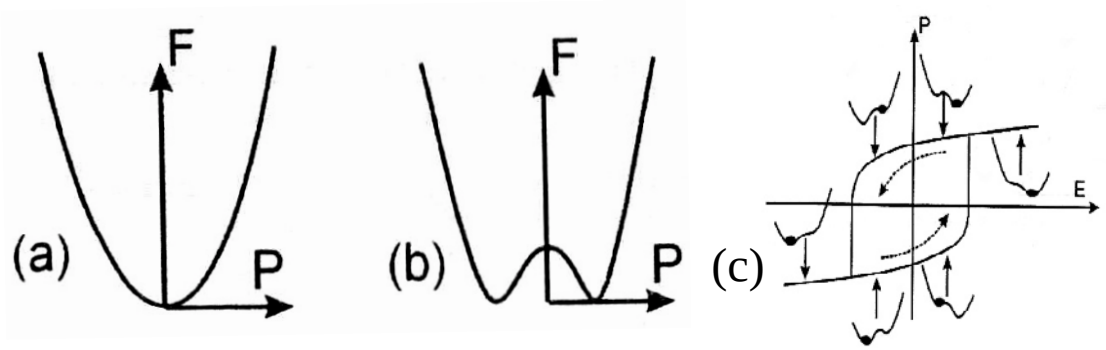

Figure 1.3 Free energy vs. polarization in (a) paraelectric and (b) ferroelectric states. (c) Schematic of a hysteresis loop showing the location of the energy wells [4].

An archetypal example of a perovskite ferroelectric is BTO, the first piezoelectric ceramic with perovskite structure to have been discovered [9]. The phase transitions of BTO are illustrated in Fig. 1.4. At temperatures above 120 ˚C, BTO has a paraelectric phase with cubic perovskite structure. Between 120 ˚C and 0 ˚C, it has a tetragonal ferroelectric phase with the polarization direction along the *c* axis. As the temperature goes down further, BTO undergoes more phase transitions from tetragonal to orthorhombic at 0 ˚C, and from orthorhombic to rhombohedral at -90 ˚C. The polarization vector rotates to the [110] direction in the orthorhombic phase and the [111] direction in the rhombohedral phase. The distortion of the lower-symmetry phase from the cubic perovskite phase is usually small. For example, the *c*/*a* ratio in the tetragonal BTO is only about 1.01. Similarly $PbTiO_3$ (PTO) undergoes a phase transition from paraelectric cubic to ferroelectric tetragonal phase at the T_c of 490 ˚C. A higher T_c is usually concomitant with a higher P_s. BTO has a P_s of 27 μC/cm^2. In comparison, PTO has a P_s of 52 μC/cm^2.

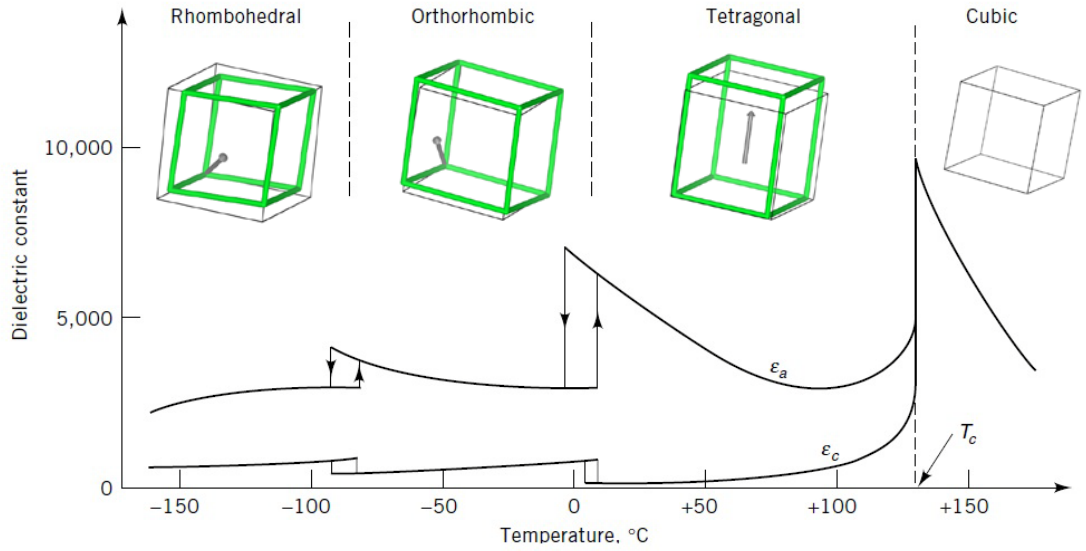

Figure 1.4 Phase transitions of BTO. Black cubes represent the cubic perovskite structure. Thick green lines show the new phases at different temperature ranges. Arrows represent the polarization directions. ε_a and ε_c represent the dielectric constants measured perpendicular and parallel to the polar axis, respectively. (adapted from Ref. [10])

1.1.2. Ferroelectric $BiFeO_3$

Of particular interest in this work is the ferroelectric $BiFeO_3$ (BFO). At the room temperature, BFO has a rhombohedrally distorted perovskite structure (space group R3m). It can be indexed in the trigonal, the hexagonal or the pseudo-cubic system (Figs. 1.5 and 1.6). As shown in Fig. 1.5, the trigonal unit cell consists of two distorted perovskite blocks connected along their body diagonals, with a large displacement of Bi^{3+} ions relative to the FeO_6 octahedra [11]. The ferroelectric polarization vector is along the pseudo-cubic $[111]_{pc}$ direction. In this study, either the hexagonal or the pseudo-cubic system is used, depending on which is more convenient and relevant at the point of discussion. The subscripts “h” and “pc” are used in this thesis to denote the hexagonal and the pseudo-cubic lattices, respectively.

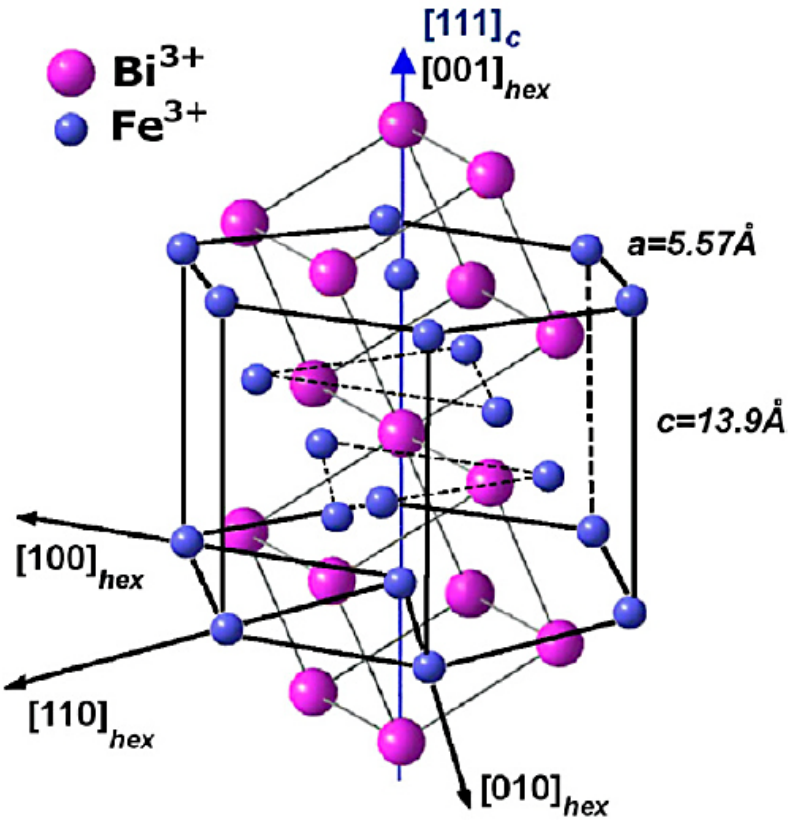

Figure 1.5 BFO unit cell in hexagonal (black lines) and pseudo-cubic (gray lines) unit cells [12]. Oxygen atoms are omitted for clarity.

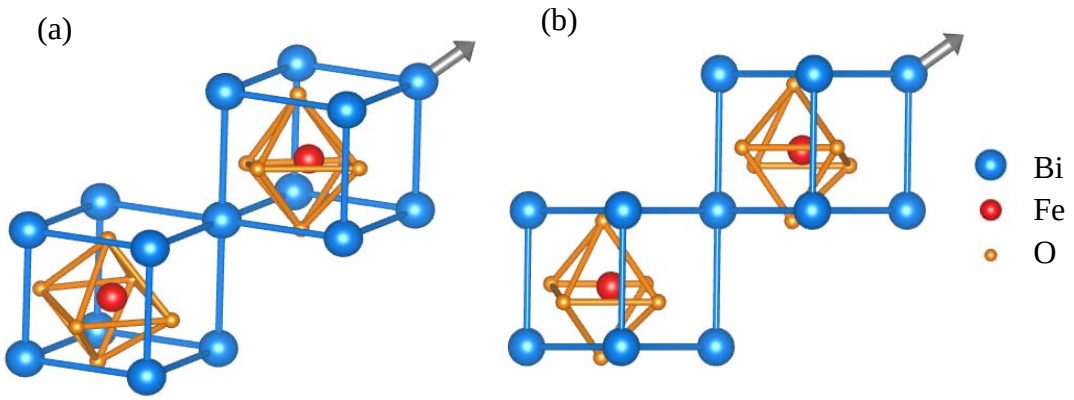

Figure 1.6 BFO crystal structure. (a) Three-dimensional representation showing two pseudo-cubic unit cells. The rotation of the oxygen octahedra is also shown. (b) The unit cells viewed along the $[110]_{pc}$ direction, showing the large displacement between Bi atoms and FeO_6 octahedra. The grey arrows show the direction of the polarization vector.

BFO undergoes a first-order phase transition to a β phase at about 825 ˚C [13]. The exact structure of this β phase has been debated but is believed to be paraelectric [14, 15]. This temperature is often regarded as the Curie temperature T_c for BFO. Due to its high T_c, BFO is expected to have a large remanent polarization. However, earlier studies in BFO have shown a very small P_s [16]. Only recently has very large P_s been obtained in epitaxially-strained BFO thin films [17]. The authors attributed this enhanced ferroelectric polarization to the compressive epitaxial strain imposed by the $SrTiO_3$ (STO) substrates. But other reports since then have disputed this claim [18]. Both first principle calculations [19] and experiments [20] have shown that the intrinsic polarization in BFO single crystals can be as high as 100 $\mu C/cm^2$. It appears now that the small polarization in those early reports were probably due to the significant leakage current in the samples. Furthermore, BFO has a Néel temperature (T_N) of 370 ˚C and is a G-type antiferromagnetic at the room temperature. The ferroelectricity in BFO is caused by the off-center of Bi^{3+} ions and the localization of Bi 6s lone electron pairs, while the ferromagnitism is caused by the usual unpaired Fe 3d orbital. This permits the co-existence of ferroelectricity and magnetism [21]. BFO is probably the only known material so far that is both ferroelectric and antiferromagnetic at the room temperature [13]. Recently there has been a flourish in research works on the multiferrocity of BFO [22-25]. A vast number of publications has focused on the potential applications of its multiferroicity in memory storage [26], sensors and actuators [27], spintronic devices [28, 29] and other multifunctional devices [30-33]. Apart from this very attractive property, its large P_s and high T_c are advantageous for a variety of applications, especially in nonvolatile ferroelectric random-access memories (FRAM) [34, 35].

In constrast to its multiferrocity, the photovoltaic property of BFO has received little attention prior to the works presented in this thesis. The focus of this thesis is on the photovoltaic properties and their mechanisms in BFO. As will be shown in the later chapters, BFO presents some unique characteristics compared to conventional photovoltaic devices and may lead to novel applications.

1.2. Photovoltaic effects and devices

As the world energy demand is expected to more than double by 2050, and as global warming has become an urgent issue on every government's agenda, the search for clean and renewable energies is generating a lot of interest. Among the many candidates, such as wind and nuclear powers, solar energy stands out as clean, safe and abundant and could provide an important solution to the world's energy demand [36-38].

One of the important methods to harvest solar energy is the photovoltaic (PV) effect, where sun light is converted into electricity. In this section I review the history and the theory of the PV technology. The importance of the PV technology in today's world will underline the motivation for this thesis.

1.2.1. History and current status of photovoltaic research

Photovoltaic effect was observed in as early as 1893 [39]. The first Si solar cell was reported by Chapin, Fuller, and Pearson at Bell Lab in 1954 [40]. It was made of a Si p-n junction with an efficiency of 6%. Currently solar cells based on semiconductor p-n junction are still the dominant technology, and Si is still the workhorse material, making up over 99% of the market share, with the remaining taken up mainly by CdTe and $CuInSe_2$. Si in various crystalline forms (*c*-Si) takes up almost 90% of the

photovoltaic market. Although multi-crystalline Si has a lower efficiency than monocrystal Si, its production has surpassed the latter in volume recently due to its lower cost [39].

The exponential growth of the solar cell industry and the recent shortage in Si feedstock have given renewed impetus in the development of thin film solar cells [36, 39]. Major classes of materials for thin film solar cells include amorphous Si, polycrystalline chalcogenide (Group VI), organic material [39] and III-V compound semiconductors [41]. The most efficient solar cell has been realized by the III-V compound semiconductors with a triple-junction structure, achieving more than 40% efficiency under concentrated light [42]. Their high efficiency, high power-to-weight ratio and good radiation hardness make them the material of choice for space power applications [43]. By an estimation in 1999, about 50% to 70% of the satellites under construction were equipped with III-V solar cells [44]. Hydrogen-passivated amorphous Si (*a*-Si:H) thin film solar cells have been making tremendous progresses because of their lower cost. In addition, *a*-Si:H has the added advantage of a bandgap that is adjustable with different levels of crystallization. This makes it very attractive for multi-junction cells.

1.2.2. Theory of photovoltaic effects

In a PV device, photons are converted into electricity. The process involves the generation of charge carriers by photon absorption, separation and transportation of the carriers and finally their collection at electrodes. A sound understanding of the PV effects in Si and other relatively more matured technologies will be of great use for the developing of PV technologies with ferroelectrics. The working principles of the PV devices based on *c*-Si, *a*-Si, and organic materials are discussed here.

1.2.2.1. Crystalline Si photovoltaic devices

Figure 1.7(a) shows the band diagram of a crystalline p-n junction PV device. Free charges are generated when photons with energies higher than the bandgap are absorbed. These photogenerated charges are then separated by the built-in field in the space charge region (SCR) and collected at the contact electrodes before flowing into external circuits to do useful work.

A typical *c*-Si solar cell is shown in Fig. 1.7(b) [39]. The electron mobility in p-type silicon is usually higher than the hole mobility in n-type silicon when both are doped to the same level [41]. The electron mobility in intrinsic Si is 1350 $cm^2/(V\ s)$ while the hole mobility is only 480 $cm^2/(V\ s)$ [45]. This means that the carrier collection is more efficient in the p-type than in the n-type layer, all the other conditions being equal. As a result, most *c*-Si solar cells adopt the structure of a n^+-p junction [41]. The p-layer (base) is much longer than the n^+-layer (emitter), and is the main optical absorber. The emitter is the top (front) layer. The absorption coefficient of Si increases from below 1000 cm^{-1} at the red end to about 15000 cm^{-1} at the wavelength of 500 nm, the solar spectrum peak. The light enters from the emitter and is strongly absorbed there, especially so in the case of the shorter wavelengths. To reduce recombination and minimize losses, the emitter is heavily doped to improve the conductivity and is much shorter than the lightly doped base. Most of the SCR is in the base, where the majority of the sunlight is absorbed and the photogenerated charge carriers are separated by the built-in field.

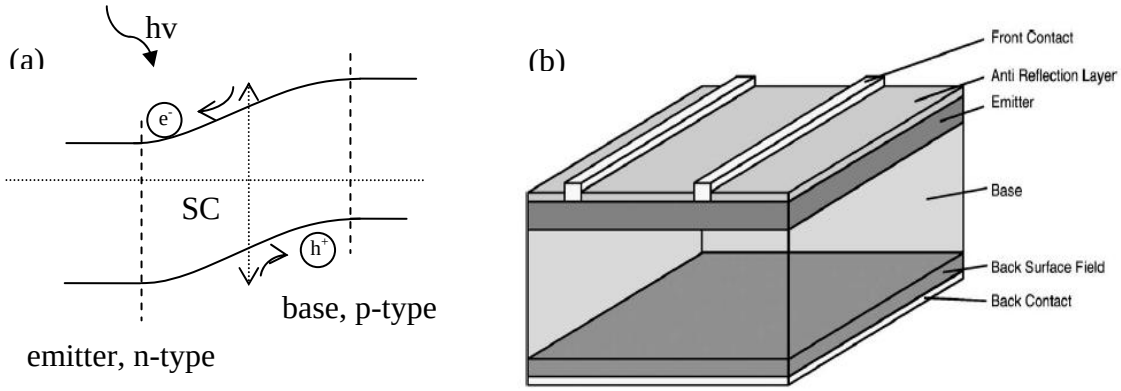

Figure 1.7 (a) The band diagram of a p-n junction under illumination, and (b) a typical *c*-Si solar cell with a n^+-p junction structure [39].

Under illumination, excess charge carriers are generated in all three regions of the cell: emitter quasi-neutral region (QNR), SCR, and base QNR [Fig. 1.7(a)]. As mentioned above, the majority of the charge carriers are generated in the base. The resulting excess minority electrons diffuse towards the edge of the SCR. Once the electrons reach the junction, they are swept over to the emitter by the built-in field. There the electrons become the majority carriers. Because of the high charge density in the emitter, the electrons experience a very small concentration gradient. However, the excess electrons in the emitter repel each other due to the Coulomb force and push them out to the top contacts [46]. An analogous analysis applies to the excess minority holes generated in the emitter. The holes diffuse to the SCR boundary in the emitter and move towards the base under the built-in field. The performance of a *c*-Si solar cell is determined by the mobility and the lifetime of the minority charge carriers.

1.2.2.2. Amorphous Si photovoltaic devices

Amorphous Si lacks the long range order that exists in *c*-Si. The variation in the bond angle and interatomic distances gives rise to the localized states near the band edges, known as the Urbach tail. Unsatisfied dangling bonds and impurities form deeper local states within the bandgap. As a result, *a*-Si is characterized by a continuous distribution of energy states across the bandgap. Hydrogen is used to passivate these dangling bonds and defects to reduce the localized states. This process produces the hydrogenated amorphous Si (*a*-Si:H).

The carrier mobility within the deep local states is negligibly small. Consequently, these deep local states form a mobility gap. The charge transport in the *a*-Si involves the trapping and de-trapping of the carriers by the local states in the band tails. The carrier mobility is a few orders of magnitude smaller than that in *c*-Si and is strongly dependent on the density of the tail states.

The diffusion lengths in *a*-Si are too short for effective charge collections (about 100-200 nm) [47]. Doping further increases the trapping density and reduces the carrier lifetime. Carriers usually recombine instantaneously in heavily doped *a*-Si:H layers. As a result, *a*-Si:H thin film solar cells usually employ a p-i-n structure, where the intrinsic i-layer is the thickest and functions as the main light absorber (Fig. 1.8).

Most of the photogeneration occurs in the i-layer, where the carrier lifetime is longer at around 3 to 30 μs [41, 48]. The SCR extends across the whole i-layer for effective charge separation [Fig. 1.8(b)]. The electric field in the i-layer absorber is about 10^6 V/m and higher at the interfaces with the p- and n-layers [47]. As a result, the photocurrent in *a*-Si solar cells is the drift current generated by the built-in field, rather than the minority carrier diffusion current as in the case of the *c*-Si solar cells.

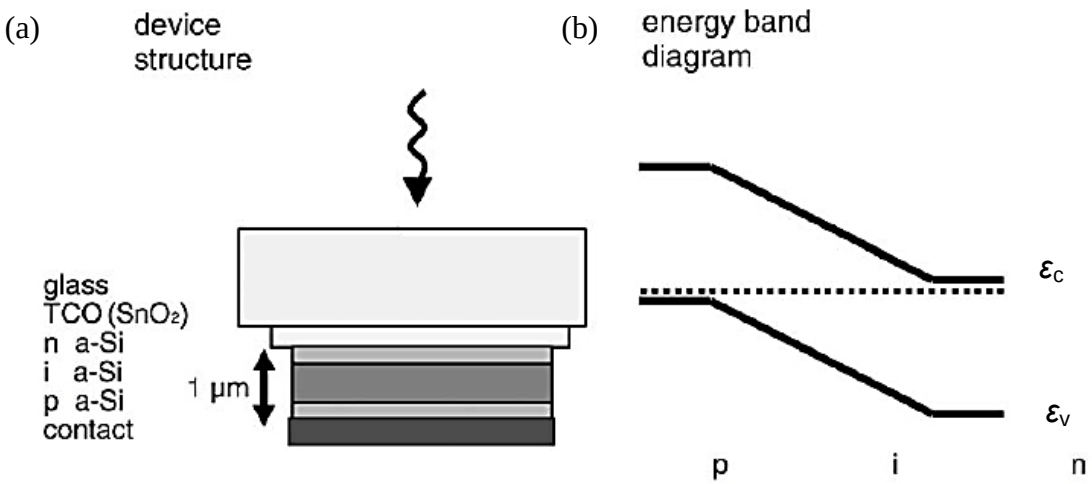

Figure 1.8 Typical *a*-Si solar cell structure. (a) The p-i-n structure. (b) The corresponding band diagram [49].

The product of mobility and lifetime $\mu\tau$ is often quoted as a figure of merit for the *a*-Si:H solar cell [48]. This value decreases with heavier doping. In the intrinsic layer of a device-quality *a*-Si:H solar cell, $\mu\tau = 10^{-6}$ cm^2/V for electrons [47]. This value means even a weak field is enough to generate a long drift length comparable with the typical i-layer thickness of 0.5 μm. In *a*-Si:H solar cells the drift length can be of hundreds of microns. This enables a relatively-thick intrinsic layer in *a*-Si:H solar cells for the effective absorption of the incident light. However, the thickness of the i-layer is limited by the requirement that it should be shorter than the SCR for efficient charge collections [47, 48].

1.2.2.3. Organic photovoltaic devices

There is a wide variety of PV cells making use of organic materials. The most successful concept of the organic solar cell at present is perhaps the dye-sensitized solar cell (DSSC). In DSSC a monolayer of dye (most notably *sci*-$RuL_2(NCS)_2$, or N3) is adsorbed onto the surface of a mesoscopic film of a wide-bandgap oxide semiconductor (e.g., TiO_2 nanoparticles). The TiO_2 nanoparticles in DSSC are usually about 20 nm in diameter [50]. The TiO_2 films have a porous high-surface-area texture

to ensure efficient light harvesting. The ratio of the real surface area to the projected area is usually over 1000. A redox electrolyte or solid organic hole conductor permeates through the oxide film to form intimate contacts for efficient hole removal [50].

Organic photovoltaic devices such as the DSSC operate by a fundamentally different process compared to the inorganic type [51]. First of all, the light absorption in organic materials almost always results in the formation of bound electron-hole pairs called excitons, rather than free electrons. Secondly, the free charge carriers are generated and separated at the same time, when the exciton dissociates at the heterointerface. This injects a free electron into an n-type semiconductor and a hole into a p-type semiconductor on the other side of the interface (Fig. 1.9). The charge carriers are then driven by diffusion and/or built-in potential towards the electrodes. The property of the heterointerface is the most important parameter here because it controls the charge separation and the injection. Afterwards, the charge transportation is by the majority carrier, which reduces recombination. The open-circuit voltage V_{oc} can be larger than the built-in potential due to the contribution of the chemical potential energy from the carrier concentration gradient (Fig. 1.9) [52].

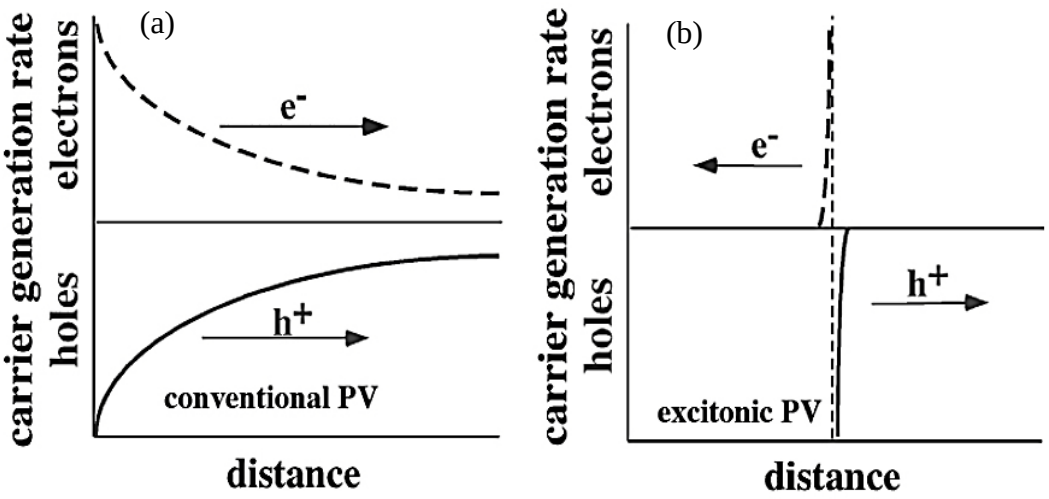

Figure 1.9 Comparison of charge separation and transportation between (a) conventional solar cell such as those based on p-n junctions and (b) exitonic solar cells. In (a), both minority and majority carriers are transported together in the same medium. In (b), electrons and holes are separated at the same time of their generation at a heterojunction and transported by separate media [52].

1.2.3. Photovoltaic effect in ferroelectric materials

Many ferroelectric crystals can be considered as wide bandgap semiconductors. Analogous to Si, they are able to produce photoexcited charge carriers from photons with energies higher than the bandgap. PV effect in ferroelectrics has been first reported in bulk ferroelectric BTO crystals in as early as 1950s [53]. The early studies revealed some striking differences between the PV effect in ferroelectrics and that from the p-n junction. One of the most important features is that the open-circuit voltage V_{oc} can be larger than the bandgap. In some cases V_{oc} of a few kV has been observed in bulk ferroelectric materials [54]. It was also discovered that the charge separation in the ferroelectric materials can occur in the homogeneous bulk regions and does not require an interface such as a p-n junction [55]. Line and Glass found that the photocurrent was only along the direction of the ferroelectric polarization vector [8]. However, many studies in bulk ferroelectric ceramics and single crystals

since then have observed photocurrents perpendicular to the polarization vector [56]. The full relationship between the incident light and the photocurrent can be described by a rank-three tensor, similar to the piezoelectric effect [Fig. 1.10(a)] [57]. This has been termed the bulk photovoltaic effect (BPVE). The photocurrent direction can even depend on the incident light wavelengths [Fig. 1.10(b)] [56]. Many have attempted to explain these rather unusual results in ferroelectric materials. These different theories have various degrees of success but so far there is not a single explanation that can satisfactorily explain all these results.

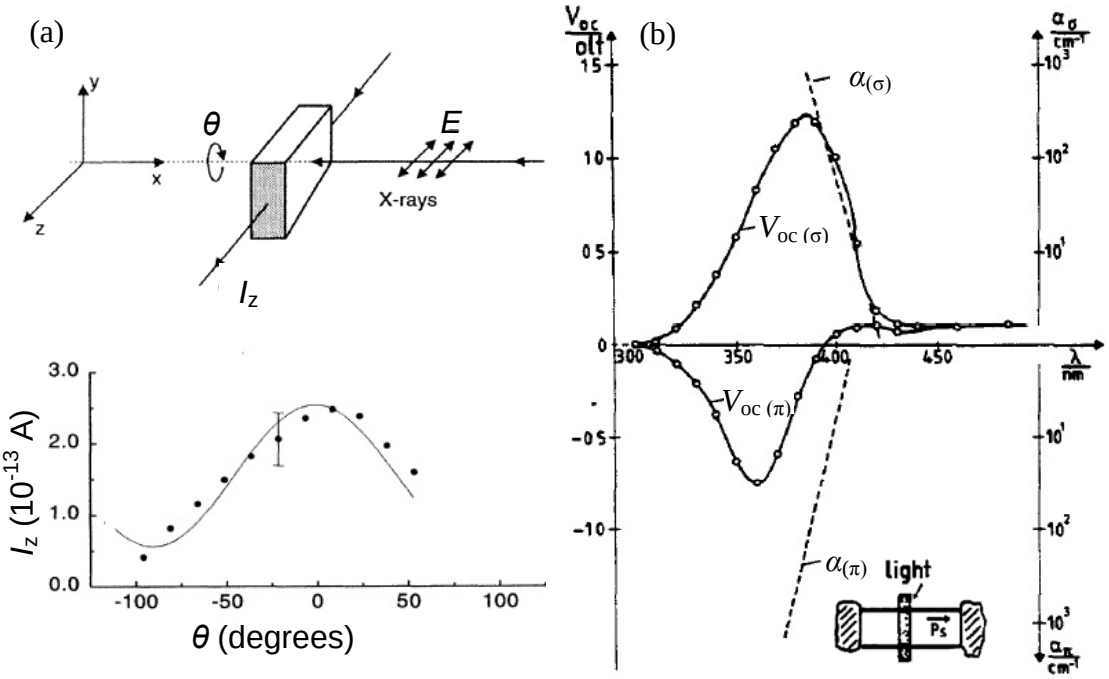

Figure 1.10 Photovoltaic measurements in ferroelectric samples. (a) Short-circuit photocurrent along the z axis of a $LiNbO_3$:Fe sample as a function of the polarization angle of the incident linearly-polarized x-ray [58]. (b) Open-circuit voltage V_{oc} and the absorption coefficient α of a BTO single crystal as a function of the incident wavelength for light polarized perpendicular (σ) and parallel (π) to the *c* axis [56].

1.2.3.1. Theories of photovoltaic effect in ferroelectric materials

- Photovoltaic theories based on local asymmetries

One of the most widely cited theories explaining the PV effects in ferroelectric materials is developed by Glass and coworkers [8]. Their initial theory is based on the photoabsorption by impurity states. They suggested that the local asymmetry of impurities in the pyroelectric host can lead to a steady-state photocurrent in $LiNbO_3$ (LNO) [54]. Electrons from the impurity atoms are excited to a delocalized state. The scattering by the local asymmetrical potential causes the probability of charge transfer in the $\pm c$ directions to differ. The steady-state short-circuit photocurrent density can be written as

$$J_{sc} = J_e - J_r = G\alpha I_L, \qquad 1\text{-}1$$

where J_e, J_r, G, α, and I_L are the current density due to the excitation of the charge carriers, the recombination current density, the Glass coefficient, the absorption coefficient, and the light intensity, respectively [54]. The Glass coefficient G is unique for each material. Equation (1-1) expresses the linear relation between the short-circuit photocurrent density and the incident light intensity.

With an external load, there is an additional component (i.e., dark current) due to the potential drop $V = E\delta$ across the thickness δ. Consequently the photocurrent density is given as

$$J = G\alpha I_L - \sigma E, \qquad 1\text{-}2$$

where σ is the conductivity. The open-circuit electric field is

$$E_{oc} = \frac{V_{oc}}{\delta} = \frac{G\alpha I_L}{\sigma}. \qquad 1\text{-}3$$

Equation (1-3) shows that V_{oc} is proportional to the sample thickness and is not limited by the bandgap. Furthermore, a higher conductivity would result in a smaller V_{oc}. For the same thickness, the V_{oc} saturates at high incident intensities as the conductivity becomes dominated by the photoconductivity, which is proportional to the incident intensity.

Chanussot and Glass later extended the model to pure pyroelectrics with band-to-band transitions [59]. In this model the directional movement of carriers is accomplished through Franck-Condon relaxation. As shown in Fig. 1.11, electronic charges are excited from the ground state (G.S.) at anion O to the nearest cation B by the absorbed photons. The excited Franck-Condon state (F.C.S.) then undergoes relaxation. At the relaxed excited state (R.E.S.), the charge recombination path will be different from its excitation path [compare (a) and (c) in Fig. 1.11]. The charge is shifted from one ion to another and a net current is generated.

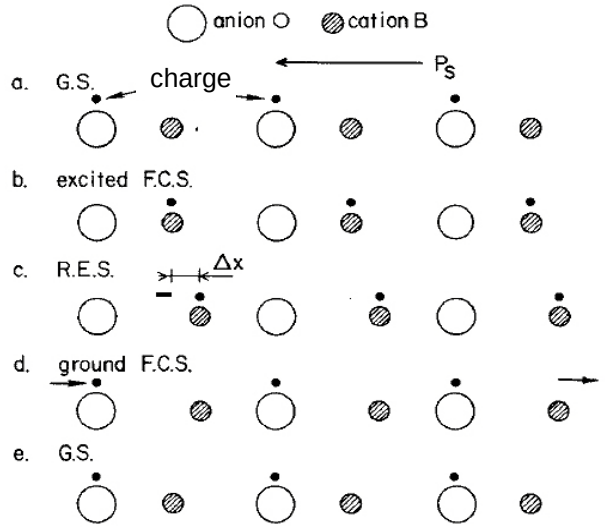

Figure 1.11 A one-dimensional representation of the photovoltaic current generation in a polar crystal. Electrons are shifted to the right through excitation and Franck-Condon relaxation [59].

The theories by Glass and coworkers give a physical picture of how asymmetric crystal structure can give rise to steady-state photocurrent through electron-phonon interaction or asymmetric potentials from impurities. Similarly Sturman and Fridkin formulated that the local microscopic asymmetries cause the photovoltaic effect in ferroelectric crystals (Fig. 1.12) [57].

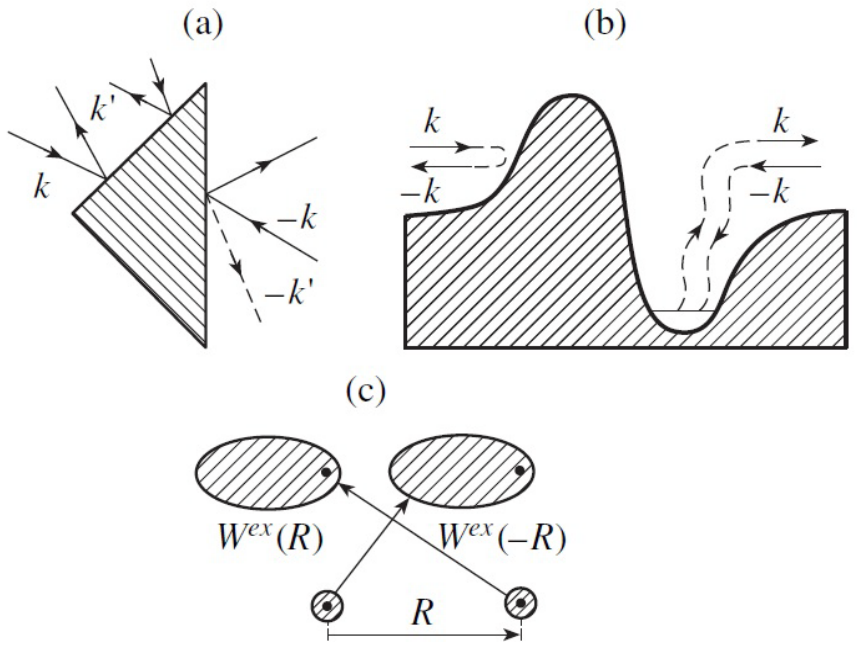

Figure 1.12 The photocurrent due to asymmetric elementary processes: (a) elastic scattering by asymmetric potential, (b) photoexcitation and recombination and (c) phototransition between localized states (impurities) [55].

- Additive photovoltage in ceramic samples

One of the salient features of the PV effects in ferroelectrics is that the open-circuit voltage V_{oc} can be larger than the bandgap. This is explained by Eq. (1-3) of Glass' theory, where a low conductivity and a thick sample give a high voltage. However, for polycrystalline or ceramic samples, Brody and Crowne proposed that the photovoltage of individual grains adds up to give the anomalous high voltage (Fig.

1.13) [60]. In the dark the polarization is partially screened in a region adjacent to the grain surface. The potential drop within the grain due to depolarization field is cancelled by the potential drop of the screening charges across grain boundaries [Fig. 1.13(a)]. When illuminated, excess free charge carriers completely screen the polarization within grains. Consequently there is no potential drop within domains. The potential drop across the grain boundaries still exists and adds up to the total photovoltage [Fig. 1.13(b)]. It should be noted that in this picture the photocurrent will always be in the direction of the polarization vector. This does not always agree with other experimental results.

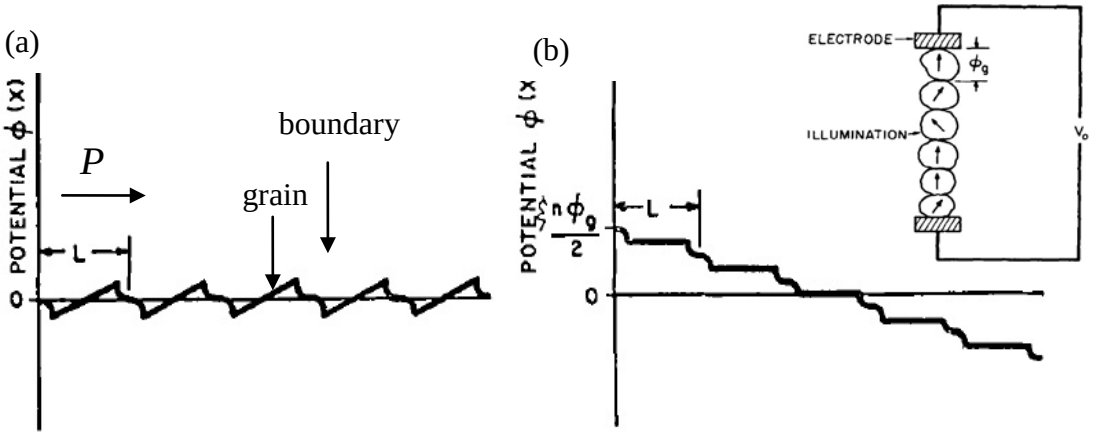

Figure 1.13 Potential profile of a poled polycrystalline sample (a) in dark and (b) under illumination. Inset illustrates the addition of the photovoltage [60].

- Photovoltaic effect from nonlinear optical effect

Tonooka et al. proposed that the photocurrent in ferroelectric materials is produced by the photoinduced nonlinear polarization [61]. By considering the nonlinear effect to the second order, they showed that this photoinduced polarization can be asymmetric in a noncentrosymmetric material such as a ferroelectric (Fig. 1.14). This asymmetric polarization results in an effective DC field which drives the photocurrent. Recently

Yuan and Wang also used optical rectification to explain the dependence of the photocurrent direction on the polarization of the incident light [62].

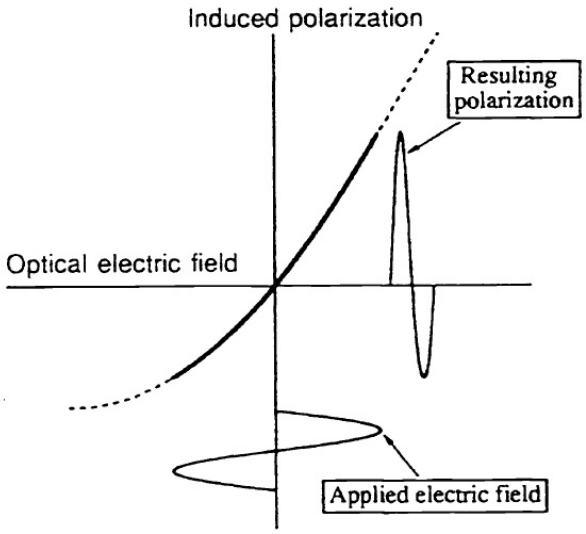

Figure 1.14 Photoinduced nonlinear polarization in an noncentrosymmetric material [61].

It is commonly understood that at optical frequency ions have too large an inertial to be polarized. As a result, second-order nonlinear effect is very weak and usually requires high intensity sources such as a laser. Furthermore, optical rectification is a transient response and is not able to sustain a DC current over a long time scale. It appears that theories based on nonlinear optical effect are probably not valid.

- Photovoltaic effect driven by ferroelectric domain walls

A recent study shows that domain walls can provide the necessary electric field for charge separation and the charge carriers rapidly recombine within the domains [63]. The authors proposed that the large photovoltage is generated as a result of the additive effect of the potential steps produced at 71˚ or 109˚ domain walls (Fig. 1.15). Ab initio studies on $PbTiO_3$ show that there is a jump in electrostatic potential of about 0.18 V across the 90˚ domain wall [64]. Density functional theory studies show

a step in the electrostatic potential of 0.15 V across the 109˚ domain walls in BFO, and 0.02 V across the 71˚ domain wall s [65]. It was proposed that these potential steps can provide the means for charge separation.

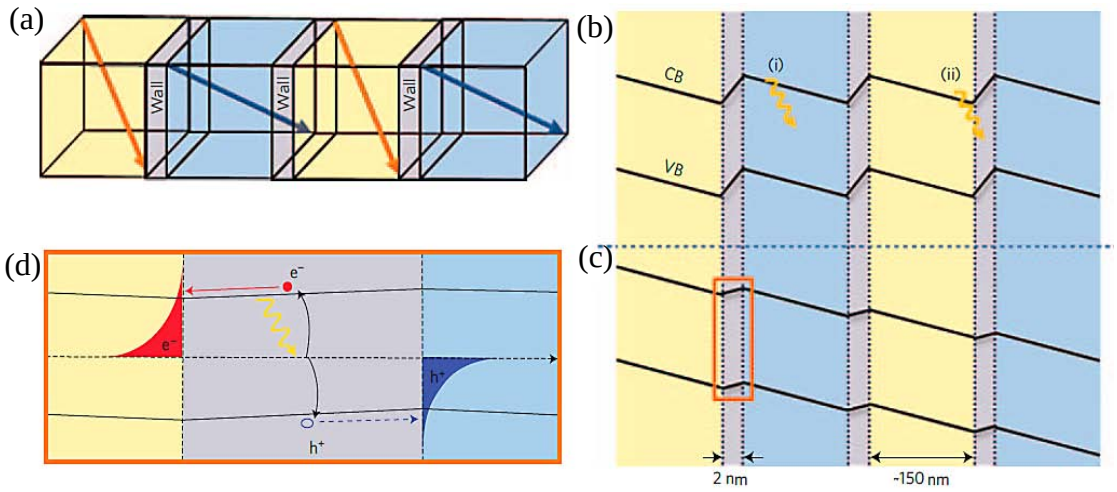

Figure 1.15 Domain wall mechanism of photovoltaic effect in a ferroelectric material (a) Schematic of four domains with 71˚ domain walls. (b) Corresponding band diagram showing the valence band and conduction band in dark. (c) Band diagram under illumination. (d) Detailed picture of the buildup of photoexcited charge carriers with domain walls [63].

At equilibrium, the potential step at the domain wall causes the offset of the conduction band and valence band. Periodic constraints require that there is an electric field within the domain in the opposite direction. Consequently the band shows a zigzag shape [Fig. 1.15(b)]. Upon illumination, exitons are separated at the domain walls, with holes moving to the right side, and electron to the left of the domain walls [Fig. 1.15(d)]. The injected electrons and holes then diffuse across the domains. Exitons deep within the domains will eventually recombine and will not contribute to the overall photocurrent. This is because that the electric field within the domain is much smaller than that across the domain walls. From this point of view, the situation is rather similar to the dye-sensitized solar cells (DSSC), where exitons dissociate at the interface between the dye sensitizers and the semiconductor

nanoparticles. The additive mechanism of the photovoltage is analogous to the model proposed by Brody and Crowne for polycrystalline samples [60]. Similarly in this case the photocurrent is in the direction of the polarization vector.

This mechanism is obviously not the BPVE, as it does not cause a dependence of the photocurrent on the incident light polarization. The validity of this theoretical model has also come under some scrutiny recently, as other studies have shown that charge carriers do not rapidly recombine within domains and in fact a constant photovoltaic current can be detected across an entire domain [66].

- The phenomenological description of the BPVE

The phenomenological description of the BPVE describes the tensorial behaviors of the photocurrent in ferroelectrics. It can be understood as follows. First, it is observed that the photocurrent is proportional to the incident light intensity I_{L} as

$$J \propto I_{\mathrm{L}} \propto |E|^2, \tag{1-4}$$

where E is the optical electric field of the incident light. Consequently, the BPVE can be described by a tensor β:

$$J = \beta |E|^2. \tag{1-5}$$

Experimental results show that the photocurrent depends on the polarization direction

$$j = \beta(0, \omega, \omega) : E(\omega)E(\omega), \tag{1-6}$$

or written using the Einstein notation

$$j_i = \beta_{ijk} E_j E_k. \tag{1-7}$$

As a result, the photovoltaic tensor has a rank of three. Equations (1-6) and (1-7) show that a DC current is produced by combining two oscillating electric field of the same frequency. This has a similar form to the optical rectification in nonlinear optics. But it is noted that in optical rectification, the incident light has a wavelength below the bandgap and does not create photocarriers. The result of optical rectification is a change in the material's polarization

$$P_i = \chi_{ijk} E_j E_k, \tag{1-8}$$

where χ_{ijk} is the second-order nonlinear optical susceptibility. Consequently, the current is only transient and the current density is

$$j_{\mathrm{OR}} = \frac{dP_i}{dt}. \tag{1-9}$$

Optical rectification, like other nonlinear optical effects, also requires a very intense incident light, usually provided by a laser. In contrast, the BPVE requires the excitation of the charge carriers and can occur at a much lower intensity. BPVE has sometimes been called above-the-bandgap optical rectification.

The optical electric field of the incident light can be expressed in a complex form

$$\bar{E} = |E| \hat{e} \exp i(k_{\mathrm{wn}} r - \omega t), \tag{1-10}$$

where $\hat{e}$ is the unit vector and k_{wn} the wavenumber. For a second-order effect to produce a DC current, one of the E's should be conjugated to cancel the time component ωt. Without the complex conjugation, the current would have a frequency of 2ω. Consequently the formula for the bulk photovoltaic current density becomes

$$j_i = \beta_{ijk} E_j E_k^*. \tag{1-11}$$

Since

$$j_i = \beta_{ijk} E_j E_k^* \propto |E|^2 \propto I_{\mathrm{L}}, \tag{1-12}$$

we can absorb the proportionality into β and write

$$J = \beta_{ijk} e_j e_k^* I_{\mathrm{L}} = \alpha G_{ijk} e_j e_k^* I_{\mathrm{L}}. \tag{1-13}$$

This is the tensor equation for the BPVE current density. Here G is the Glass coefficient and β the BPVE tensor coefficient [57]. Note here e_i is the time-space dependent directional cosine of the optical electric field along the i^{th} axis

$$e_i = (\hat{e} \cdot \hat{i}) \exp i(kr - \omega t), \tag{1-14}$$

where $\hat{i}$ is the unit vector of the i^{th} axis. As it is equally valid to take the complex conjugate of any of the E's in the equation above, the indices j and k can be interchanged as

$$j_i = \beta_{ijk} E_j E_k^* = \beta_{ijk} E_k E_j^* = \beta_{ikj} E_k E_j^*. \tag{1-15}$$

Consequently

$$\beta_{ijk} = \beta_{ikj}. \tag{1-16}$$

This is the permutation symmetry, and is valid independent of the point group of a specific material. Due to the permutation symmetry, there are 18 independent components in β. The BPVE tensor shares the same form as the piezoelectric tensor

because both follow the same symmetry properties. Consequently, the BPVE is only observed in materials in the piezoelectric group.

The phenomenological description of the BPVE shows the relationship between the light polarization and the structure of the ferroelectric material. However, it does not explain the origin of the phenomenon, nor can it predict the magnitude of the photovoltaic response.

- Photovoltaic effect from depolarization field in thin films

Ferroelectric polarization can induce an electric field within the material in the direction opposite to the polarization. This field is called the depolarization field E_d. In a bulk material, where the dimension between boundaries (e.g., crystal surfaces) is large, the effect of E_d is normally small. However, in a thin film, where the thickness is on the order of tens to a few hundreds of nanometers, the effect of E_d can be significant. When the magnitude of E_d is comparable with the coercive field E_c, the ferroelectric domains can even be depoled by E_d [67]. The screening of the polarization charges by charge carriers from the ferroelectric material or from the external environment (e.g., electrodes) can reduce the magnitude of E_d and help to stabilize the ferroelectric domains. Nevertheless, the polarization charges are normally only partially compensated. Therefore, the resulting E_d can act to separate and transport photoexcited charge carriers, similar to the built-in electric field within the depletion region of a p-n junction. The depolarization field due to the incomplete compensation of the polarization charge has been proposed as one of the possible PV mechanisms for ferroelectric thin films with small thickness [68, 69].

By analyzing the distribution of polarization charge and the screening charge within the ferroelectric films and also the electrodes in an electrode-ferroelectric-electrode sandwich structure (Fig. 1.16), Qin et al. showed that the short-circuit photocurrent increases exponentially with the decrease of the film thickness. The photocurrent also increases with larger remanent polarizations [68]. They further showed that the use of electrodes with high effective dielectric constants, which reduce the screening effect for the polarization charges, can dramatically improve the PV output in ferroelectric thin films [69]. A theoretical maximum efficiency of 19.5% is predicted in a 1.2-nm-thick film. These encouraging results suggest that the low efficiency of 10^{-6} to 10^{-4} predicted in the bulk ferroelectric materials [55] could be overcome by the use of ferroelectrics of low dimensions. However, currently the highest efficiency in a sandwich-structure device with a single ferroelectric PLZT thin film is about 0.28% [70], falling far short of the theoretical prediction.

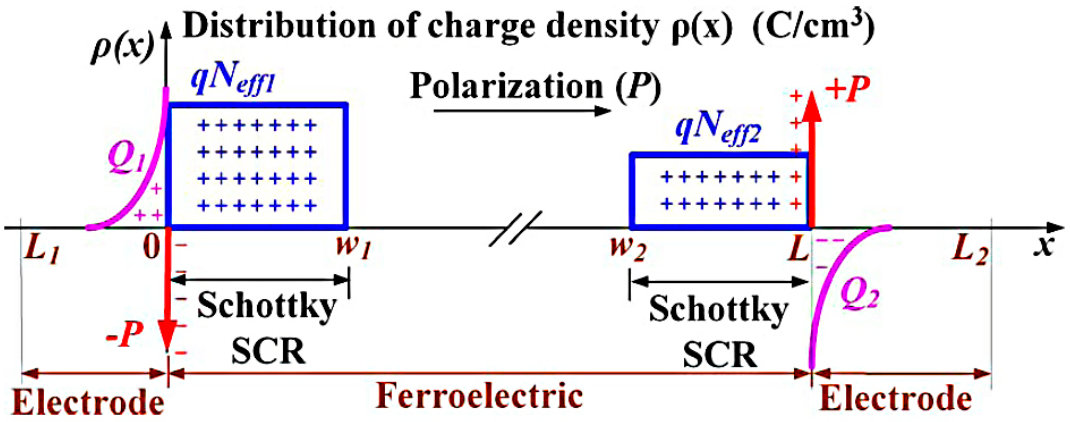

Figure 1.16 The charge distribution in an electrode-ferroelectric-electrode sandwich-structure device [69]. Ferroelectric polarization charges are modeled as the sheet charge P. Q_1 and Q_2 are the screening charges within the electrode with a finite screening length. N_{eff1} and N_{eff2} are the space charges within the Schottky junction space charge regions (SCR).

- Conclusion

In conclusion, it appears that the myriad of phenomena observed in the PV effect in ferroelectric materials can hardly be explained by one universal theory. Many of the proposed models reviewed here can only explain some aspects of the experimental results but fail in other aspects. The interpretation of the experimental data is often complicated by a number of factors. Complex oxides such as ferroelectrics often have some degree of nonstoichiometry, defects, and impurities. These have a major influence on the sample properties. One commonly encountered issue is the oxygen stoichiometry. Oxygen deficiency can introduce donors while excess oxygen content can introduce a secondary phase. These variables can profoundly affect the PV results in ferroelectric thin films.

Incomplete screening of the polarization in ferroelectric thin films results in the depolarization field [67, 71, 72], which can contribute to the photocurrent as well [68, 69]. More importantly, much higher PV efficiency of 19.5% has been predicted in the ferroelectric thin films by considering the depolarization field [69]. However, no experimental results have come even close to that prediction. The discrepancy between the theoretical prediction and the experimental results points to an incomplete understanding of the topic. We have to bear in mind the complexity of the PV processes in ferroelectric thin films. Factors of nonstoichiomtry, defects, and impurities can all affect the PV process. Additional factors, such as the surfaces and interfaces, become increasingly important too as the film thickness reduces. Electrodes often form Schottky barriers with the ferroelectrics and can have a significant effect to the overall response in thin films [73, 74]. Further progresses in the understanding of the PV effect in ferroelectric systems require careful

experimental designs that can separate and quantify the different contributions and factors that affect the PV process.

1.2.3.2. Recent development of photovoltaic research in ferroelectrics

Despite the various intriguing PV effects that are unique in the ferroelectrics, the interest in ferroelectric materials for PV applications had been very limited and largely confined in the field of photorefraction [75-77]. This is because of the very low PV efficiencies in the bulk ferroelectrics [55], which are usually insulating wide bandgap materials with low charge mobility. One way to overcome this limit is to work with materials of lower dimensions. In the ferroelectric thin film, properties insignificant in the bulk can become important. The depolarization field increases with the decrease of the thickness and can become sufficiently large in ferroelectric thin films to cause the charge separation and transportation [78]. This depolarization field can possibly enhance the PV effect if it works constructively with other mechanisms. The Schottky junctions at the interfaces between the film and the electrodes can play an important role in the overall PV effect as well. In addition, strain engineering of thin films can create material systems inaccessible in the bulk and lead to new discoveries. Recently it has been proposed and shown that remarkably higher photovoltaic efficiency can be achieved in thin films [68, 70]. Open-circuit voltages much larger than the bandgap have also been achieved in ferroelectric thin films with in-plane interdigital electrodes [79], which has led to the development of UV sensors and dosimeters [80]. The possibilities of higher efficiency and novel applications have attracted increasing interest in the field of ferroelectric thin film photovoltaic devices (Fig. 1.17).

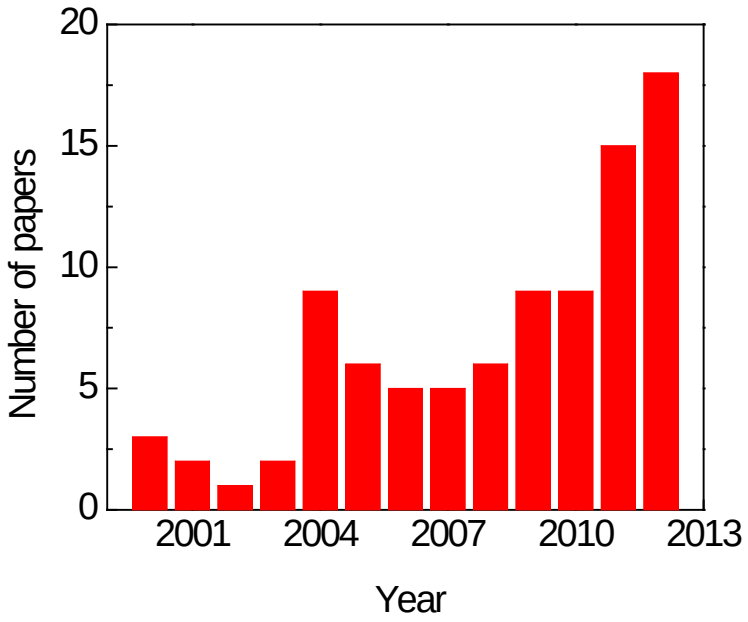

Figure 1.17 The number of articles per year published in the literature on the PV effect in ferroelectric or ferroelectric-composite materials. Source: Scopus with key words "ferroelectric" and "photovoltaic".

1.2.4. $BiFeO_3$ as a photovoltaic material

The ferroelectric thin film materials under the previous studies, such as BTO and $Pb(ZrTi)O_3$ (PZT), have wide bandgaps (typically larger than 3.3 eV) corresponding to the UV region. For energy harvesting and many other possible applications, smaller bandgaps in the visible part of the solar spectrum is desired. BFO, with a bandgap near 2.72 eV [81] and a very large remanent ferroelectric polarization [17, 18, 82], is an excellent material for such investigations. Since the start of this project, appreciable photoconductivity in visible light has been reported in BFO [83], and optical studies by absorption spectrum [83, 84] and spectroscopic ellipsometry [85] have shown that BFO has a direct bandgap with a high absorption coefficient. Recently switchable diode effect and visible-light photovoltaic effect have been observed in BFO bulk crystals [86]. However, no values of the photovoltage have

been reported for ferroelectric BFO prior to the work in this thesis. Neither has any significant photovoltaic response been demonstrated in BFO thin films at the time. It is also unclear if the photovoltaic response in BFO is due to the diode effect, the BPVE, Schottky junctions or any combination of these. It is difficult to improve the PV efficiency or to develop other multifunctional applications using the BFO thin films without a clear understanding of the mechanisms. The PV effect in BFO thin films and the different mechanisms that contribute to it will be investigated in this work.

1.3. Photoelectrolytic effect for water splitting

Solar power provides a clean and renewable energy source. Photovoltaic panels have long been used to harvest the solar energy by converting it into electricity. However the production of electricity from solar power rises and falls with the daily and seasonal fluctuations of the sunlight that reaches the earth surface. In order to provide a reliable energy source, there is a need to store the excess electricity to be used when the sunlight is not sufficient. A different approach, as in the photosynthesis in plants, is to convert solar energy directly into chemical energy, which can be stored much more easily than electricity. This is called photoelectrolysis. Hydrogen is one of the most desired chemical energy storage media. It has high specific energy, is nontoxic and environmentally benign, and can be produced from an abundant source: water [87]. A photoelectrolytic cell can harvest the solar power to break water molecules into H_2 and O_2, which can then produce electricity through a fuel cell with only water as the by-product (Fig. 1.18). This provides a truly clean and sustainable energy source.

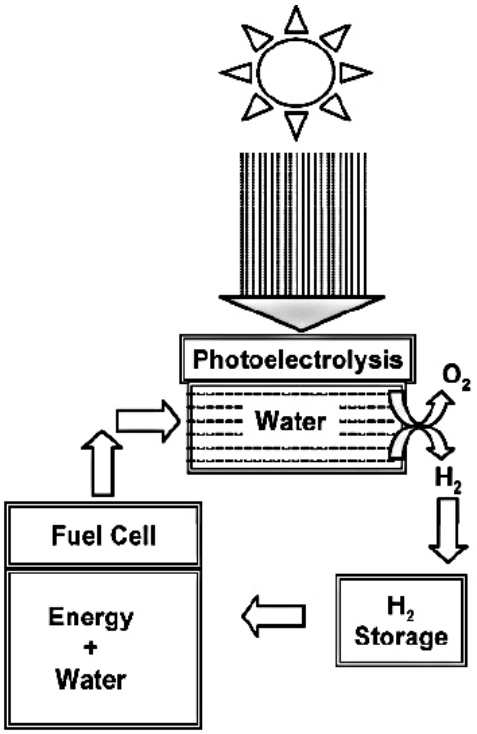

Figure 1.18 Photoelectrolytic water splitting to produce H_2 as a clean and renewable energy source [87].

Ever since the first report on water splitting by the use of TiO_2 in 1972 [88], photoelectrolytic water splitting reactions using semiconductor electrodes have been the focus of numerous studies. TiO_2 has a wide bandgap of more than 3 eV. As a result, it can only absorb the UV portion of the solar spectrum. BFO has a smaller bandgap corresponding to the visible region. Furthermore, BFO is also a ferroelectric material. Its ferroelectric polarization charges can modify the electronic structures of the surfaces. It has been shown that the catalytic properties of the surface can be modified by the polarization to enhance the desired reactions [89, 90]. The use of BFO as a photoelectrode seems a very attractive option for water splitting as it offers the possibility of unassisted reaction and enhanced functionality through the ferroelectric polarization.

1.4. Motivation and objectives

This project is motivated by the need for clean and renewable energy. Solar energy will be an important part in the future of clean energy. This requires the exploration and discovery of better materials and devices. Ferroelectric materials have shown some unique features that are not accessible in the conventional PV devices based on p-n junctions. These include larger-than-bandgap photovoltages and tensorial photocurrents. Furthermore, many ferroelectrics are multifunctional materials. The coupling of the PV effect with other useful properties can lead to the development of new applications and devices. In this respect, ferroelectrics provide an opportunity for new discoveries in energy harvesting and other applications.

This project is also motivated by the need to understand the mechanisms of the PV effect in a ferroelectric thin film device. Previous studies focused on the ferroelectric bulk materials, which have very low efficiencies. In a ferroelectric thin film, as the thickness is reduced, the effects of the free surfaces and the interfaces become comparable to its bulk properties. This can have a drastic effect on the PV properties in ferroelectric thin films. As a result, new phenomena might be discovered and the efficiencies can be potentially improved. To improve the performance of any PV devices based on ferroelectric thin films, it is necessary to understand its mechanisms first.

The relatively-small direct bandgap and its excellent ferroelectric polarization makes BFO an ideal material for the studies on the PV effect in a ferroelectric thin film. The objectives of this project include:

- To clarify the mechanism of PV effect in ferroelectric BFO thin films

- To explore possible applications for the solar energy harvesting based on the ferroelectric BFO thin films.

1.5. Organization of thesis

This thesis consists of seven chapters. Chapter 1 gives the background of this thesis starting with a general introduction to the ferroelectric materials and to the material of interest, BFO, in particular. This is followed by a review of the PV effects in *c*-Si, *a*-Si and exitonic solar cells. The PV effects in ferroelectric systems, both in bulk and thin films, are reviewed. The motivations and objectives of this thesis are stated.

Chapter 2 discusses the various experimental techniques employed in this work. Fabrication methods and various characterization techniques are discussed with an emphasis on the aspects that are most relevant to the current work.

Chapter 3 presents the properties of the epitaxial BFO thin films and other materials fabricated in this work, including the ceramic BFO targets, the processed substrates, and the bottom electrode.

Chapter 4 discusses the effects of the ferroelectric polarization on the PV responses of the BFO thin films. The BFO films with different ferroelectric polarizations are prepared and their PV responses are measured. A clear relationship of the PV response to the depolarization field is observed and a theoretical model is proposed.

Chapter 5 investigates the existence of the BPVE in ferroelectric thin films. In-plane electrodes are used on BFO thin films with the ferroelectric polarization in the out-of-plane direction. The photocurrent from the BPVE is observed for the first time in ferroelectric films as thin as 40 nm. The BPVE coefficient of the BFO thin films is

calculated and found to be much larger than that of many other ferroelectric materials. The BPVE in poled PLZT ceramic thin films is also investigated and the results are discussed.

Chapter 6 analyses the photoelectrolytic water splitting effect in BFO thin films by linear sweep voltametry. The oxygen evolution reaction is observed by the measurement of the anodic photocurrent. The oxygen The effects of the ferroelectric polarization on the photoelectrolytic effect of the ferroelectric photoelectrodes are discussed. A monolithic cell capable of unassisted water splitting reactions based on such effects is proposed.

Chapter 7 summarizes the important findings of this thesis and suggests future works.

Chapter 2. Experimental techniques

2.1. Preparation of ferroelectric oxide thin films

2.1.1. Substrate selection and preparation

2.1.1.1. Substrate selection

An appropriate substrate is crucial for the growth of epitaxial films. The lattice mismatch between the film and the substrate induces mechanical strains, which are released through the creation of dislocation defects and twinning domains [91]. High density of defects can cause large leakage currents and degradation of ferroelectric properties. The epitaxial strain ε_s is defined as

$$\varepsilon_s = \frac{a_{//} - a_o}{a_o}, \qquad 2\text{-}1$$

where $a_{//}$ and a_o are the in-plane lattice constants of the strained and the fully-relaxed ferroelectric material, respectively [92]. A comparison of the lattice parameters between BFO and some common substrates is shown in Fig. 2.1. $SrTiO_3$ (STO) has one of the smallest lattice mismatches with BFO (-1.44%) and has been extensively studied. Methods to prepare atomically flat STO surfaces have been developed. For a device of the sandwich structure, bottom electrodes are required. For epitaxial growth the bottom electrodes are required to function as a template as well. The conducting perovskite oxide $SrRuO_3$ (SRO) has a small lattice mismatch to BFO (-0.96%) and has been shown to promote the growth of the BFO phase [93]. The compressive strain from SRO-buffered STO substrates can enhance the ferroelectric polarization in (001)-oriented BFO films by forcing the polarization vector to rotate towards the out-of-plane direction [94], while the small lattice mismatch ensures high quality epitaxial

growth. For these reasons, STO is selected as the substrate and SRO is used as the buffer layer and the bottom electrode for ferroelectric BFO thin films.

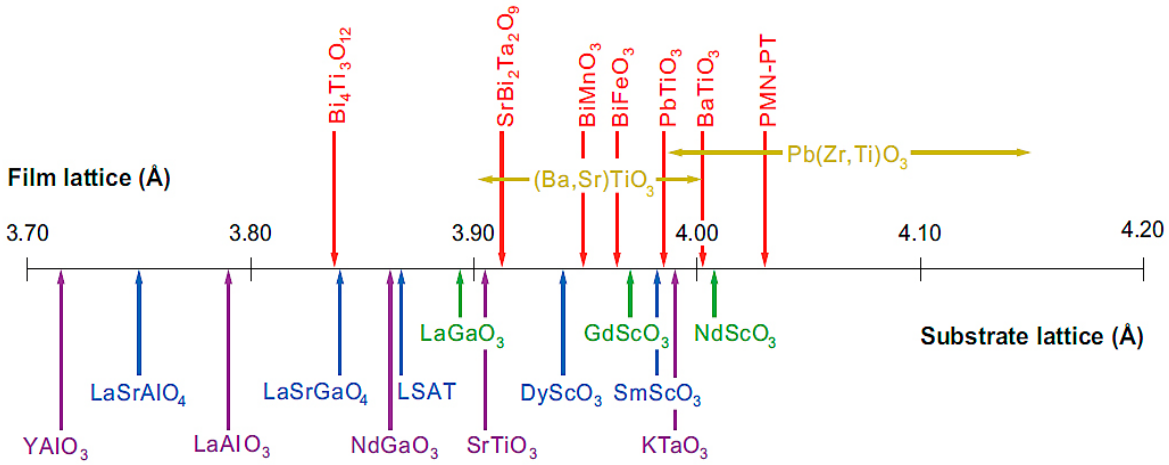

Figure 2.1 Lattice constants for common ferroelectric films and substrates [92].

The epitaxial BFO films on the STO(001) substrates are expected to be fully strained up to the thickness of about 40 nm [24, 95]. Thicker films will be partially relaxed but will not fully relax until a few microns in thickness, as illustrated by the example of the epitaxial $Pb(MgNb)O_3$ (PMN) films grown on the STO substrates (Fig. 2.2).

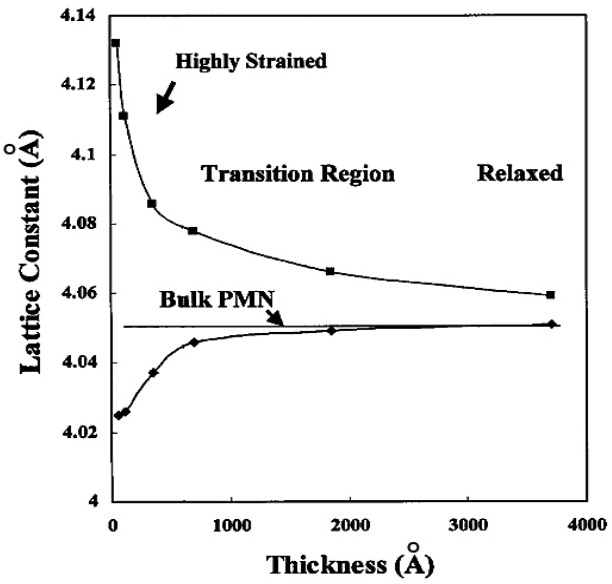

Figure 2.2 PMN on STO substrate (3.7% strain). The lattice is relaxed within a few microns [96].

The substrate condition plays a crucial role in the epitaxial film quality. Its surface energy decides the film growth mode. High surface energies promote wetting and 2D epitaxial growth. If the surface energy is smaller, 3D island growth will be dominant. Cleaning the surface removes the adsorbed carbons and other contaminants, and enhances the surface energy. Oxygen plasma cleaning can be used to further increase the surface energy in some cases.

Film surfaces with energetically different sites are illustrated in Fig. 2.3. In order to obtain smooth surfaces, step flow growth is preferred. In this mode, deposited atoms (adatoms) do not have enough energy to nucleate on the film surface. Instead they must diffuse to the step edges (ledges) and get attached there, resulting in the steady advances of the steps along the vicinal direction. Adatoms become more mobile at higher substrate temperatures, and their diffusion lengths increase. Epitaxial films are only obtained at relatively high growth temperatures when the adatoms are mobile enough. Subsequent thermal annealing can promote crystal growth and release some of the built-in strains.

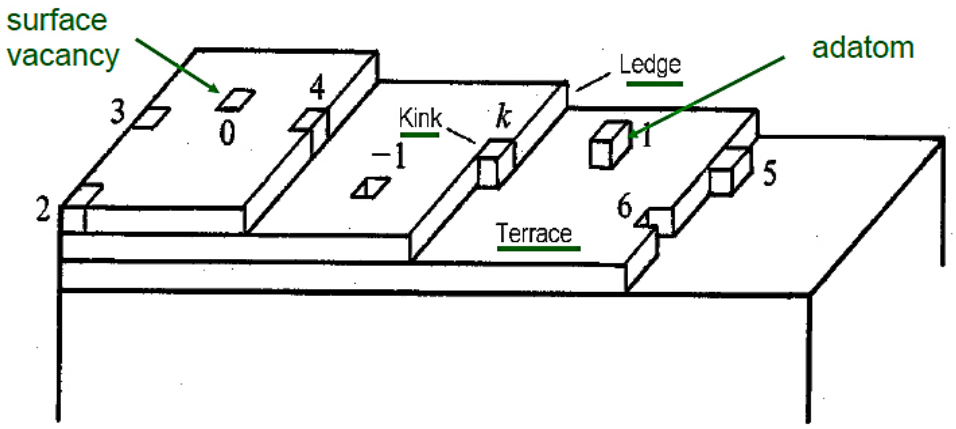

Figure 2.3 Terrace-ledge-kink model showing energetically different sites [97].

2.1.1.2. Preparation of vicinal $SrTiO_3$ substrate

The STO(001) surface can have either the SrO or the TiO_2 termination. The as-received substrate surface is usually chemical-mechanically polished to a very small roughness. But these surfaces are not well-ordered on the atomic scale. Different crystal surfaces are exposed and the surface has mixed terminations. Adatoms will behave differently at different sites due to the different bonding energies. In addition, significant strains can be introduced to the surface during the polishing process. Consequently, the surface may not be stable at an elevated temperature.

Atomically flat substrate surfaces can promote the formation of high quality epitaxial films. The TiO_2-terminated surface is much more stable than the SrO-terminated surface. The preparation of atomically flat TiO_2-terminated STO substrates has been well studied. Two methods are generally employed: high-temperature annealing and chemical etching [4].

High-temperature annealing promotes recrystallization of the surface layer and helps to release the strain. Background oxygen pressure is important to reduce the oxygen vacancy formation. The Sr vacancy and segregation is a problem with the high-temperature annealing method. Step edges of more than 1 unit cell high (step bunching) can also occur at the annealed surface.

Etching with buffered hydrofluoric acid (BHF) has been used successfully by many reports to prepare atomically flat TiO_2-terminated STO substrates [98]. This method works because SrO is a basic oxide and TiO_2 is an acidic oxide. The acid preferentially dissolves the SrO layer and any segregated Sr. After that, etching proceeds in the step-flow mode as Sr is removed from the step edge and the covering

TiO_2 layer is removed [4]. However, acid also attacks TiO_2 and can form etch pits in the middle of the terrace. The pH value of the solution must be adjusted so that the newly formed etch pits are removed fast enough. Studies show that a pH value between 4 and 5 is appropriate [98]. If the pH is higher than 5, the surface might have etch residues.

In this work vicinal surfaces of the STO(001) substrates were prepared by a combination of the chemical and the thermal treatments [99]. The substrates were first soaked in DI water at 50 ˚C for 30 minutes with ultrasonic agitation. They were then etched with a diluted buffered oxide etchant (Honeywell 7:1 modified etchant with DI water at 1:1 ratio) for 30 seconds. Finally they were annealed in air at 950 ˚C for one hour.

2.1.2. Sputter deposition

Sputtering is the ejection of (mostly neutral) atoms from a target surface as a result of energetic particle bombardments. The sputtered materials can be used to grow films onto substrates by condensation. This method of material growth is called the sputter deposition.

Plasma is the most common source of the energetic ions for the sputtering process in a sputter deposition equipment. In a DC plasma discharge, almost all the applied voltage is dropped across the cathode sheath (Fig. 2.4). Ions are accelerated across this region and bombard the target (cathode). The sputtered atoms are deposited onto substrates to grow films. Due to the buildup of the cations on the targets, the DC plasma sputter method is not suitable for the deposition of dielectric materials. This problem is overcome by the use of the RF plasma. In an RF plasma, the sheath boundary oscillates with the driving voltage. A time-average DC voltage is present

within the sheath region to accelerate the ions to the target surface. Somewhere during the positive half-cycle, the sheath width approaches zero and the electrons are able to reach the surface to neutralize the charge buildup. One disadvantage of the RF plasma sputter deposition compared with the DC method is a lower deposition rate (at the range of nm/hr).

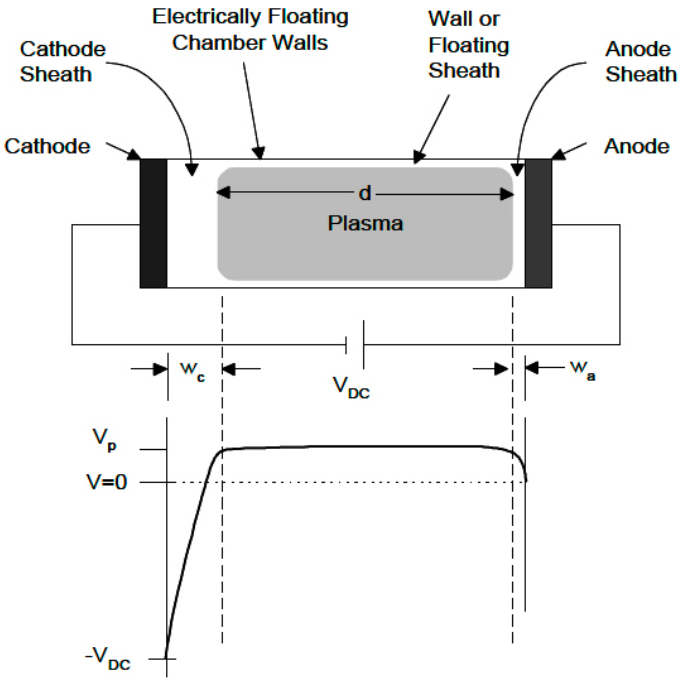

Figure 2.4 DC discharge and the potential distribution between the electrodes and the plasma [100].

RF magnetron sputter deposition is used for the growth of the epitaxial $SrRuO_3$ (SRO) and BFO films, and the tin-doped indium oxide (ITO) electrode. The equipment used are: Oerlikon Sputtering System at the advanced materials lab (ACL) from the school of materials science and engineering (NUS), Oerlikon Sputtering System in IMRE, and Nanofilm Unbalanced Magnetron Sputtering System (UBM in short) in IMRE. The targets for the UBM were purchased from commercial suppliers. Metal electrodes are grown using the DC deposition method with Denton II (Denton Discovery 18 Magnetron Sputtering System) in IMRE.

2.1.3. Photolithography

Photolithography is a process that transfers geometric shapes on a mask onto a substrate by optical means. For this project, the image reversal photoresist AZ5214 was used for the patterning of the top electrodes. AZ5214 can be used as a positive resist. However, its strength is the image reversal capability. By an additional reversal bake and a flood exposure after the first exposure, the pattern can be reversed to negative. The result is a reversed-trapezoidal profile with a high resolution. An added advantage of AZ5214 is its low viscosity, which results in a thinner resist layer with reduced edge effects. This is important in this project as the sizes of the substrates used are rather small, ranging from 3x3 mm^2 to 5x5 mm^2.

2.2. Characterization techniques

2.2.1. X-ray diffraction (XRD)

The spacing between crystal lattices is typically on the order of a few angstroms, comparable to the wavelength of x-ray. When x-ray is incident on a set of lattice planes it can be diffracted due to elastic scattering. The interference patterns from this diffraction can be used to determine the phase and the structural parameters of a crystalline material. This is the basic idea of XRD. Commonly used x-ray sources include the Cu kα and the Co kα lines. The former is the most widely used and has the wavelengths of 1.5406 and 1.5444 Å for $k\alpha_1$ and $k\alpha_2$ lines, respectively.

Two XRD systems have been used in this project for the characterization of different systems. Both use the Cu $k\alpha_1$ x-ray source. The general area detector diffraction system (GADDS) from Bruker is equipped with an area detector that is capable of simultaneous collections of many diffraction peaks over a 2θ angle (2θ is the angle between the incident and the refracted x-ray wave vectors). The detector on the

GADDS covers about 30° of 2 θ. Due to its fast data collection and its relatively low resolution of 0.02°, GADDS is most suitable for the rapid phase identification of polycrystalline samples.

The Panalytical X'pert MRD high resolution XRD (HRXRD) is equipped with a point detector. It only collects a single diffraction at one time and often requires hours for a single scan. However, it has a very high resolution and is used for the characterization of epitaxial thin-film samples. It employs a four circle diffractometer to manipulate the sample and the detector to bring different reciprocal space vectors into the diffraction conditions.

2.2.2. Field-emission scanning electron microscopy (FESEM)

Conventional optical microscopy is unable to resolve features on the order of nanometers due to the fundamental diffraction limit. Electrons can attain sub-nanometer wavelengths when they are accelerated to a few kV's and therefore provide a much higher resolution. Among the many electron microscopy techniques, SEM is routinely employed for the observation of the microstructures of semiconductor and MEMS devices. SEM scans across the sample surface with a collimated electron beam, which generates secondary electrons from the sample surface among other products. In the most common applications the secondary electrons are collected and processed to form an image of the sample surface. The contrast of the image is mainly caused by the topography of the sample. The advantage of using secondary electrons is its smaller generation volume, which provides a higher resolution than back scattered electrons. In addition, it is not a strong function of the atomic number *Z* and thus will not cause appreciable contrast from the variations of atomic species.

It is important to note that although the diameter of the electron beam on a FESEM is on the order of 0.1 nm, its resolution is about one nm due to the larger secondary electron generation volumes. The generation volume of the secondary electrons in an insulator such as a ferroelectric film is usually a few tens of nanometers in depth. The total interaction volume of the incident electron can be a few microns deep and can affect the SEM image. As a result, the images of the same surface can appear different depending on the particular parameters used.

It is important to understand the influences of the different parameters on the SEM image. The acceleration voltage is one of the parameters that has a major effect on the image quality. A higher acceleration voltage produces electrons with shorter wavelengths. However, the interaction volume is increased as well and unwanted signals such as back scattered electrons will be increased. This often results in degraded images. Charging and sample damage might also occur. As a result, it is often desirable to use smaller accelerating voltage, especially on insulating or relatively smooth samples. Other parameters can also be adjusted to achieve the optimum image quality. The resolution can be enhanced by using smaller objective apertures or smaller probe currents. The downside is a more grainy image. The working distance can also be reduced to improve the image resolution, but at the cost of a shallower depth of field. Tilting the sample can increase the contrast by enhancing the secondary electron emission from the edges. It is often necessary to optimize these parameters to obtain good SEM images of insulating ferroelectric thin films. In this project a JSM-6700F FESEM from JOEL Ltd. was used for the characterization of ferroelectric thin films and ceramic samples. Insulating samples were coated with gold before the observation to minimize the charging effects.

2.2.3. X-ray photoelectron spectroscopy (XPS)

XPS is an electron spectroscopy technique that allows both elemental and chemical identifications. This technique works by measuring the kinetic energy of the ejected photoelectrons. When core electrons of an atom absorb photons with energies higher than their binding energies, they can be ejected out. These ejected photoelectrons are collected by a high-resolution spectrometer and their kinetic energies are measured. The binding energy can then be calculated. Because the binding energies of the core electrons are characteristic of the atomic species, their valence states, as well as the chemical bonds, XPS provides a very sensitive tool for the identification of both elements and chemical states.

One characteristic of XPS is its high surface sensitivity. Only the photoelectrons originating from less than a few nanometers deep from the surface can be ejected out of the sample. Photoelectrons lose energy through inelastic scatterings with the neighboring atoms on the route to the surface. In insulators, the loss of core electrons can also cause positive charging. Both these effects reduce the kinetic energies of the escaping photoelectrons and increase the apparent binding energies. These shifts can be corrected from the well-known C 1s peak (284.5 eV). Charging in insulating samples can be reduced by an electron flood gun as well. In this project, an XPS VG ESCALAB 2201-XL Imaging System was used for the analysis of BFO stoichiometry. The x-ray source was Al K_α (1486.6 eV).

2.2.4. Atomic-force microscopy (AFM)

Imaging the surface of a smooth insulating epitaxial ferroelectric film with SEM often presents considerable challenges. AFM in these instances can often prove a better

solution. A type of scanning probe microscopy (SPM), AFM was originally developed in 1986 to observe insulating samples [101]. To image the sample topography with AFM, a sharp tip suspended at one end of a cantilever is scanned across the sample surface with the sample mounted on a piezoelectric tube scanner. A laser beam is directed onto the back of the cantilever and reflected onto a four-segment position-sensitive photodiode (PSPD). The position of the reflected laser spot on the PSPD is a direct measurement of the movement of the cantilever. In this project, a NanoScope IV multi-mode AFM from Veeco Metrology Group was used for the topography characterization in tapping mode.

2.2.5. Electrical, optical and photovoltaic characterizations

2.2.5.1. Low frequency dielectric properties

Dielectric properties measure the response of a material to an electric field. The dielectric constant is

$$\varepsilon_r(\omega) = \varepsilon'(\omega) - i\varepsilon''(\omega). \qquad 2\text{-}2$$

The real part of the dielectric constant is a measure of the material's ability to store energy by polarization (analogous to a spring). The imaginary part describes the dissipation of the energy in the form of Joule heating. The dielectric constant is a function of the frequency. This is because the polarizability of different systems is different at different frequencies (Fig. 2.5). It can be seen that at low frequencies dipoles and boundary planes contribute to the dielectric response of the materials. The large polarizability of the dipoles in the ferroelectric materials leads to the large real dielectric constant at low frequencies. At optical frequencies only electrons are light enough to follow the optical electric field. The dielectric constant of a ferroelectric

material at optical frequency is therefore similar to other nonferroelectric dielectric materials.

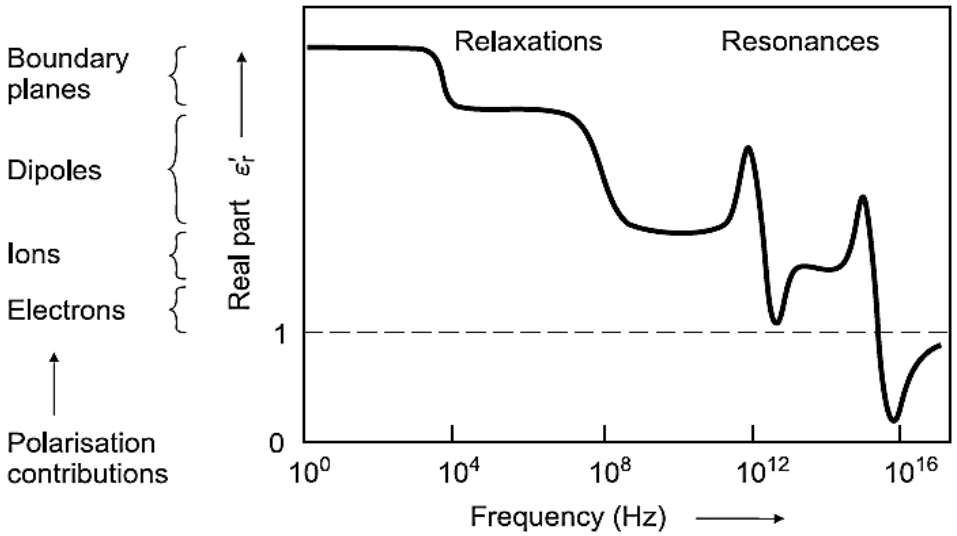

Figure 2.5 Different contributions to the real component of the dielectric constant [102]. The boundary planes refer to the accumulation of charges at structural interfaces in a heterogeneous material.

In this project, an Agiligent 4294A Precision Impedance Analyzer was used to measure the low frequency dielectric response of the ferroelectric samples. Its measurement frequency covers from 40 Hz to 110 MHz. The outputs from the impedance analyzer are the equivalent parallel capacitance (C_p) and the loss factor (D). The dielectric constants are then calculated by

$$\varepsilon' = \frac{C_p \times \delta}{\varepsilon_0 \times A}, \qquad 2\text{-}3$$

$$\varepsilon'' = D \times \varepsilon', \qquad 2\text{-}4$$

where δ is the sample thickness, ε_0 the permittivity of vacuum, and A the device area.

The reason for choosing the C_p-D model is that the devices used in this work typically have a very small capacitance and thus a large impedance value. The impedance analyzer measures the impedance vector and calculates the capacitance according to the selected model. Theoretically the ferroelectric capacitor should be modeled as a capacitor with one resistor in parallel and one in series (Fig. 2.6). However, the values of these three components cannot be simultaneously determined from the measured impedance vector. In practice this is simplified to one of the two models to choose from: a capacitor with a resistor either in parallel, or in series. The former is suitable when the device capacitance is small, i.e., the impedance of the equivalent capacitor is large. In this case the capacitor with the parallel resistor has a large impedance and the serial resistor can be omitted without causing large errors. On the other hand, when the device has a large capacitance and thus a small impedance, the parallel resistor can be ignored and equivalent series capacitor model should be used instead. In this project the ferroelectric capacitor normally has a small electrode of 0.2 mm in diameter. The capacitance of these devices is typically on the order of hundreds of pF and the impedance is on the order of tens of MΩ, much larger than any serial resistances (mainly from electrode contacts) encountered in these devices. Consequently, the parallel capacitor model is more appropriate.

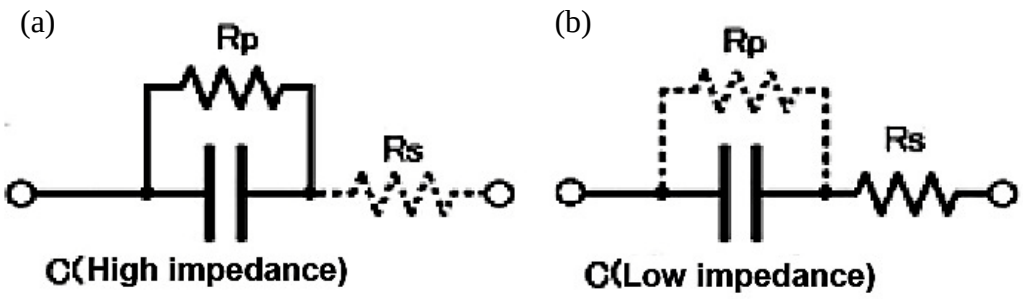

Figure 2.6 Equivalent circuit of a ferroelectric capacitor with (a) a small capacitance, and (b) a large capacitance.

2.2.5.2. Optical frequency dielectric properties

Ellipsometry is an optical technique widely used for the measurement of the thickness and properties of thin films. The refractive indices and dielectric constants at optical frequencies can be measured by spectroscopic ellipsometry. Ellipsometry measures the change in both the amplitude and polarization of a linearly polarized light after it is reflected from a sample surface. The optical constants can be calculated by using an appropriate dispersion model to fit the experimental results over a wide range of wavelengths in spectroscopic ellipsometry. The optical dielectric constant is calculated from the relationship $\varepsilon_\infty = n^2$. In this project a Variable Angel Spectroscopic Ellipsometer from J. A. Woollam Co., Inc. was used.

2.2.6. Ferroelectric properties

The total electric flux density *D* in a ferroelectric system comprises of both the linear dielectric component and the nonlinear ferroelectric polarization

$$D = \varepsilon_0 \varepsilon' E + P. \qquad 2\text{-}5$$

When the ferroelectric is subject to a electric field, the change in *D* gives a displacement current density

$$J_{\mathrm{d}} = \frac{\partial D}{\partial t}. \qquad 2\text{-}6$$

This current is integrated to obtain *D*. The measured *D* is plotted vs. the applied electric field *E*. This plot is commonly called the *P*-*E* plot as the contribution from the linear dielectric response is very small compared to the ferroelectric polarization.

The ferroelectric properties of the samples were investigated using a Radiant Technology Precision Premium II tester. Two identical bipolar triangular waveforms were used successively for the measurement (Fig. 2.7). The first wave was to preset the ferroelectric to $-P_r$. The second wave was used to measure the hysteresis loop.

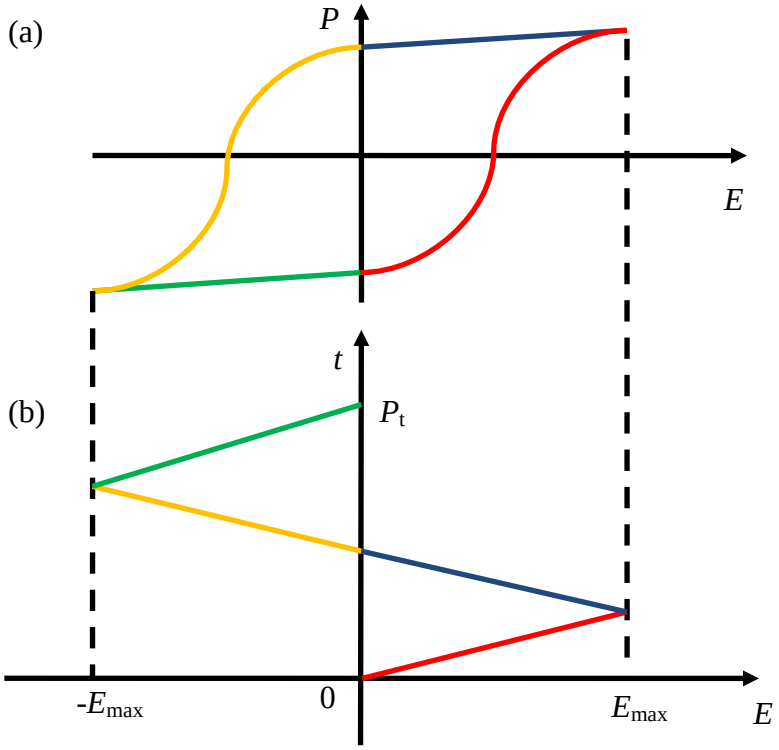

Figure 2.7 (a) Ferroelectric hysteresis and (b) the measurement waveform vs. time *t*. P_t denotes the measurement period. Segments of the hysteresis loop corresponds to the segments on the wave form of the same color. The preset waveform is identical to the measurement waveform and is not shown.

This system was also used for the poling of the BFO films. In this case, a uni-polar triangular waveform was used with the maximum voltage larger than the coercive field. The pulse period was about 0.1 ms. The use of the short electrical pulses was to prevent damages to the BFO films that could occur when conventional DC poling was used.

2.2.7. Piezoelectric properties

The piezoelectric property is an important parameter in a ferroelectric material. The piezoelectric coefficients of bulk samples are usually obtained from the resonance method. However such methods are usually not applicable to thin films deposited on thick substrates as the resonance frequency can be dominated by the substrates [103]. The laser scanning vibrometer (LSV) provides a direct and accurate measurement of the piezoelectric response from thin-film samples through the converse piezoelectric effect. Compared to other methods for thin film piezoelectric measurements, one major strength of the LSV is its ability to map the piezoelectric response of an entire area on the film with and without electrode coverage [104].

In this project an LSV system (OFV-3001-SF6, PolyTech GmbH) consisting of mainly a vibrometer scanning head, a vibrometer controller, a junction box, and a host computer was used. A function generator (HP33120A) was connected to a high speed power amplifier (NF Electronic Instruments 4010) to produce the driving signal. A sine signal with a frequency of 5 KHz and a peak-to-peak voltage of 1 V was applied. Gold top electrodes were patterned on the samples prior to the measurements. The electrodes of the samples were connected to the output of the high speed amplifier. The dilation of the region covered by the electrode and the immediate surrounding areas were scanned. The average dilation of the electrode area was subtracted by that of the surrounding area to obtain the piezoelectric dilation η. The effective piezoelectric coefficient d_{33} is calculated according to

$$d_{33} = \frac{\eta}{V}, \qquad 2\text{-}7$$

where V is the applied voltage.

2.2.8. Optical spectroscopy

Optical spectroscopy provides a valuable tool to understand the different processes that occur when light interacts with photovoltaic materials. The absorption of photons can occur via the fundamental absorption between the valence and the conduction bands, or via impurity states. For the fundamental absorption, it can be either direct or indirect. These processes can be studied by the optical absorption spectroscopy. In this project a Shimadzu UV-3101 UV-vis-NIR spectrometer was used to study the absorption processes in BFO thin film. The absorption of the substrate is measured by a reference beam. The absorption of the samples (BFO films on substrate) is measured by another beam of identical intensity. The absorbance *abs* is obtained by

$$abs(\lambda) = \lg\left(\frac{I_{\mathrm{L,substrate}}(\lambda)}{I_{\mathrm{L,sample}}(\lambda)}\right), \qquad 2\text{-}8$$

where $I_{\mathrm{L,substrate}}$ and $I_{\mathrm{L,sample}}$ are the intensities after the beams have passed the reference substrate and the sample, respectively. The absorption coefficient α of the BFO film is

$$\alpha = \frac{1}{\delta}(abs) / \lg(e), \qquad 2\text{-}9$$

where e is the Euler's number and δ the sample thickness. The discussions above show that the technique used here ignores other losses such as scattering and reflections, and probably overestimates the α. However, these effects are usually very small when compared to the fundamental absorption, which is the main interest in most of the experiments.

Photocurrent spectroscopy is another useful method to investigate the properties of photovoltaic materials. The short-circuit photocurrent is measured at different wavelengths. This gives direct information on the region of wavelengths that is responsible for the production of the photocurrent. In this work the spectral response of the short-circuit photocurrent was recorded by a spectral measurement system (NCL, Acton Research) with a solar simulator (Oriel 66011) as the light source, with an integrating time of one second.

2.2.9. Hall effect

Hall effect measurement is a widely used technique for the electrical characterization of metals and semiconductors. Its strength lies in its ability to simultaneously measure the resistivity, the charge carrier density, the carrier mobility, and the carrier types. Its operating principle is the well-known that Lorentz force electrons experience when they move in a magnetic field. One thing to take note is that the calculation of the charge carrier density and mobility from the measured Hall voltage assumes the conduction is dominated by one majority carrier. With ambipolar conductions, as in intrinsic or highly compensated semiconductors, the calculated values can have considerable errors under such assumptions.

This project used an Accent HL5500PC Hall System for the electrical characterization of the oxide electrodes. Samples were prepared in the square van der Pauw shape. Indium was soldered onto the four corners of the square to provide Ohmic contacts. The Hall System would detect any asymmetries in the sample geometry and provide compensations.

2.2.10. Current density-electric field characteristics

The current density-electric field (*J-E*) characteristics were measured with an electrometer (Keithley 6517A), with the sample connected in the force-voltage-measure-current configuration. Different conduction mechanisms have been found in ferroelectric films. In many cases the low-field conduction is found to be Ohmic. In the intermediate field strength, space-charge limited conduction (SCLC), Schottky emission and Poole-Frenkel (PF) emission have all been reported as the dominant conduction mechanisms by different authors. At very high fields, Fowler-Nordheim (FN) tunneling has often been found to dominate. These different conduction mechanisms and the methods to differentiate them experimentally are summarized below.

- Space charge limited current (SCLC)

SCLC arises when charges are injected over the interface faster than they can move in the bulk and the current density is

$$J_{\text{sclc}} = \frac{9\mu\varepsilon_0\varepsilon' V^2}{8}\frac{V^2}{\delta^3} = (\frac{9\mu\varepsilon_0\varepsilon'}{8\delta})E^2, \qquad 2\text{-}10$$

where μ is the charge mobility, ε_0 the vacuum permittivity, ε' the low frequency relative dielectric constant, and δ the sample thickness [105]. If both J_{sclc} and E are plotted in the natural log scale as

$$\ln(J_{\text{sclc}}) = \ln(\frac{9\mu\varepsilon_0\varepsilon'}{8\delta}) + 2\ln E, \qquad 2\text{-}11$$

the slope should be two for SCLC. If the slope is one, it shows that the conduction is Ohmic.

- Poole-Frenkel emission

Poole-Frenkel emission involves the charge hopping between defect trap centers. It can be thought of as field-enhanced thermal excitation of trapped electrons and the current density is

$$J_{\text{p-f}} = cE\exp(-\frac{\Phi_{\text{t}} - \beta_{\text{t}}\sqrt{E}}{k_{\text{B}}T}), \qquad 2\text{-}12$$

where

$$\beta_{\text{t}} = \sqrt{q^3 / \pi\varepsilon_0\varepsilon_\infty}, \qquad 2\text{-}13$$

and Φ_{t} is the trap ionization energy (in eV), T the absolute temperature, and ε_∞ the optical frequency dielectric constant [106]. The plot $\ln(J_{\text{p-f}})$ vs. $\sqrt{E}$ should be a straight line and the dielectric constant can be obtained from the slope of

$$\ln(\frac{J_{\text{p-f}}}{E}) = \ln(\sigma) = (\ln(cE) - \frac{\Phi_{\text{t}}}{k_{\text{B}}T}) + \frac{\beta_{\text{t}}}{k_{\text{B}}T}\sqrt{E}. \qquad 2\text{-}14$$

- Schottky Emission

Schottky emission describes the charge injection over Schottky barrier. Standard Richardson-Schottky thermionic emission equation is originally derived for a metal/vacuum interface as

$$J_{\text{s}} = A^*T^2\exp(-\frac{\Phi_{\text{SB}} - \beta\sqrt{E}}{k_{\text{B}}T}), \qquad 2\text{-}15$$

where

$$A^* = 4\pi qm^*k^2 / h^3, \qquad 2\text{-}16$$

and

$$\beta = \sqrt{q^3 / 4\pi\varepsilon_0\varepsilon_\infty}. \qquad 2\text{-}17$$

Here Φ_{SB} is the Schottky barrier height (in eV), T the absolute temperature, and A^* the Richardson constant. It is noted the appropriate dielectric constant is the optical one $\varepsilon_\infty = n^2$ [107]. The second term in Eq. (2-15) is to account for the image-force effect.

This equation is extensively used in the literature to describe the Schottky emission. However, it should be noted J_s is the reverse saturation current density. As a result, this equation is appropriate in a MFM capacitor where one of the barriers is always reverse biased. The forward conduction over a Schottky barrier is described by the following equation

$$J = J_s[\exp(\frac{qV}{n_i k_B T}) - 1], \qquad 2\text{-}18$$

where n_i is the ideality factor. In an ideal Schottky barrier, n_i is unity. When $qV > 3k_B T$, the number 1 in the square bracket might be safely omitted and the forward current increases exponentially with the applied bias. Here the image lowering effect is neglected because it is a weak function of the applied bias. Consequently, J_s is assumed to be constant.

- Fowler-Nordheim tunneling

Fowler-Nordheim tunneling occurs when electrons tunnel through potential barriers assisted by a high electric field. Due to the presence of the high electric field, the

effective barrier width is reduced and the tunneling becomes easier. The current density can be expressed by the following equation

$$J_{FN} = AE^2 \exp(-\frac{8\pi\sqrt{2m^*}(\Phi_B)^{3/2}}{3qh}\frac{1}{E}), \qquad 2\text{-}19$$

where A is a constant and Φ_B is the barrier height (in eV). The plot $\ln(J_{FN}) - (1/E)$ is a straight line and the barrier height can be extracted from its slope.

Chapter 3. Preparation and properties of epitaxial $BiFeO_3$ thin films by sputter deposition

3.1. Introduction

This project studies the ferroelectric contributions to the photovoltaic effect. Epitaxial BFO thin film is a suitable system for such studies. The ferroelectric polarization in an epitaxial film can be controlled and tailored to the desired configuration by the use of specific substrates. The aligned ferroelectric domains in epitaxial films produce a larger polarization than polycrystalline samples, where the domains are randomly orientated. It has also been very difficult to achieve large polarization in polycrystalline BFO films due to the large leakage current. This problem can be solved by the use of high quality epitaxial BFO films.

Sputter deposition is widely used for the deposition of complex metal oxide films in research and in industrial production. This technique gives good control of film properties with excellent repeatability. Large-area depositions with good uniformity can be achieved by the use of large targets. The results can be readily scaled up for industrial applications. For these reasons this project uses sputter deposition for the growth of high quality epitaxial BFO films.

3.2. $BiFeO_3$ ceramic sputtering targets

The difficulties in prepare single phase BFO ceramic have been well-documented. In fact, many of the commercial targets we purchased turned out to have almost no BFO phase. The films grown from these targets with little BFO phase showed large amount of secondary phases.

The standard mixed-oxide synthesis was used for the preparation of the BFO ceramic targets. This method often produces BFO accompanied with impurities. Bernardo et al. showed that BFO phase forms by Bi^{3+} diffusion into Fe_2O_3, a process involving the formation of the secondary phases $Bi_{25}FeO_{39}$ and $Bi_2Fe_4O_9$ [108]. A competition is established between the diffusion process that forms BFO and the crystallization of stable $Bi_2Fe_4O_9$ mullite crystals, which tend to block the formation of BFO. As a result, all three phases coexist in the final product. Different approaches have been adopted in an attempt to produce phase-pure BFO. Mahesh Kumar et al. obtained single phase BFO by leaching with dilute nitric acid [109]. Shvartsman et al. claimed they obtained phase-pure BFO by calcinig at 820 ˚C twice but did not provide the XRD results [110].

In order to compensate for the volatility of Bi during calcinations and sputter depositions, 10 at.% excess of Bi_2O_3 was used in the process in this work. The formation of the BFO ceramic has been investigated by differential scanning calorimetry (DSC) of the powder mixture (Fig. 3.1). The broad exothermic peak around 700 ˚C is from the reaction of the mixed oxides and the crystallization of BFO. Two endothermic peaks are observed at 825 ˚C and 779 ˚C. The first corresponds to the phase transition temperature T_c, while the second has also been observed in BFO before [111]. This shows that BFO phase is already formed at or before 779 ˚C from the mixed oxides. BFO does not melt below 900 ˚C as no endothermic peaks are observed between 825 ˚C and 900 ˚C. The thermal studies here provide a guide for the calcination and sintering temperatures for the ceramic target preparation.

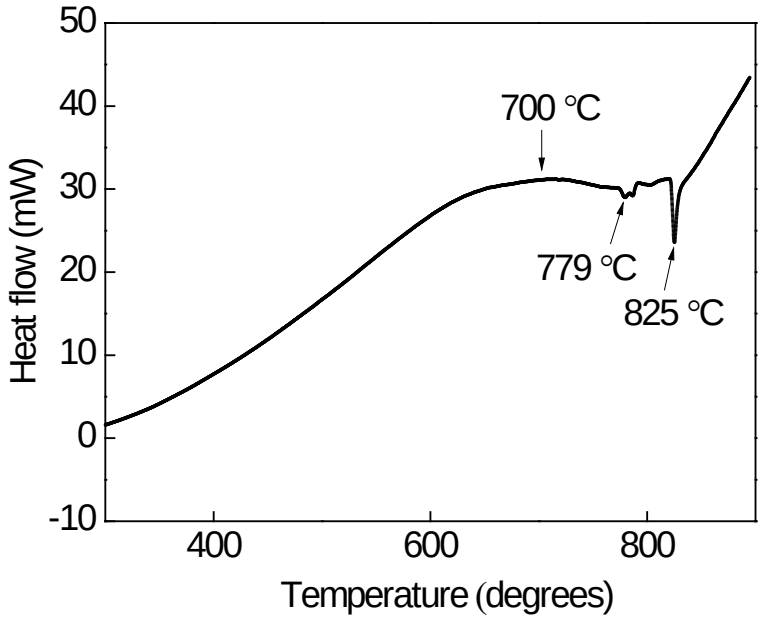

Figure 3.1 DSC curve of a powder mixture of Bi_2O_3:Fe_2O_3 (1.1:1). The heating rate is 1 ˚C/min in air. Downward peaks are endothermic.

Powders of Bi_2O_3 and Fe_2O_3 with a molar ratio of 1.1:1 were first mixed by ball milling to achieve good homogeneity. The powders were then collected and calcined in air at 750 ˚C for 6 hours. The BFO powders were then crushed and ground by ball milling. The purpose of this step was to achieve small particle sizes that would result in a good density in the final ceramic pellet. A small amount of polyvinyl alcohol (PVA) was homogeneously mixed into the BFO powders to promote the adhesion between the BFO particles and improve the mechanical integrity of the green pellet. The BFO powders were then pressed into a pellet and sintered at 850 ˚C for 2 hours. The pellet was then polished on both sides till they were flat and parallel. Finally an oxygen-free copper backing plate was bonded to one side of the pellet with silver epoxy to improve its mechanical strength and thermal conductivity.

The XRD results show that the final product is predominantly BFO with trace amounts of $Bi_{25}FeO_{39}$ but no $Bi_2Fe_4O_9$ [Fig. 3.2(a)]. The excess amount of Bi is believed to tip the balance of the reaction towards the Bi-rich direction. The phase purity is improved by sintering at 850 ˚C. The SEM images show that the sintered BFO pellet form dense grains of about 20 μm in diameter [Fig. 3.2(b)].

(a)

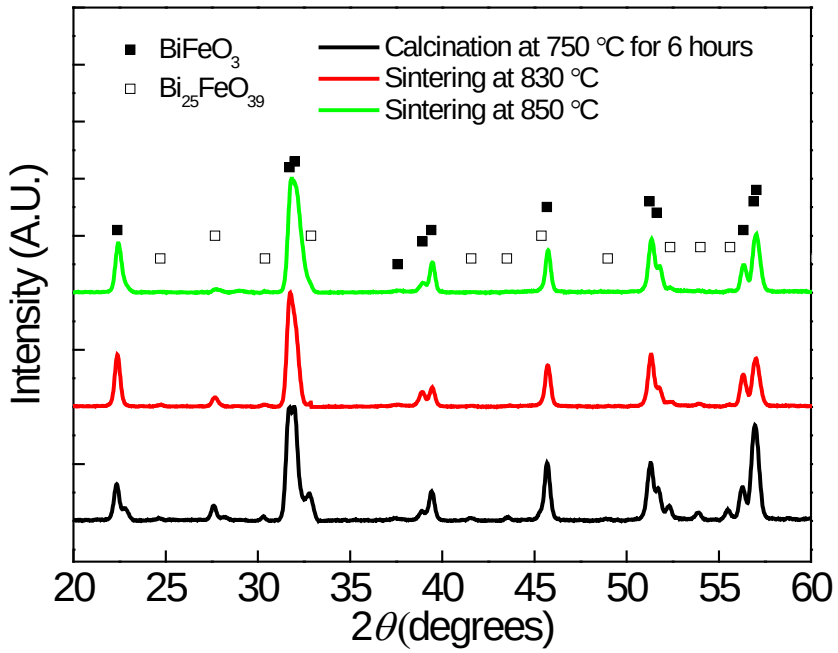

(b)

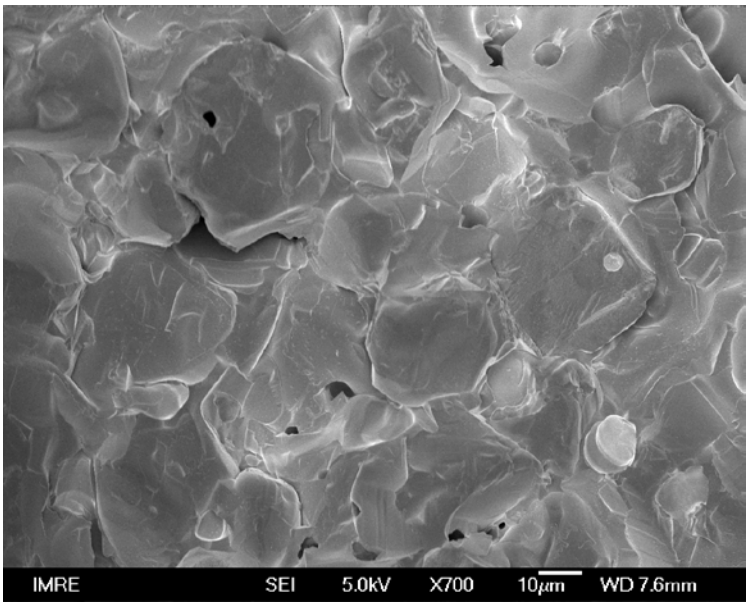

Figure 3.2 (a) XRD patterns of the BFO ceramic pellets after different processing. (b) SEM image of the BFO pellet sintered at 850 ˚C.

3.3. Vicinal $SrTiO_3$ substrates

Vicinal surfaces of the substrate (Fig. 3.3) were obtained by a combination of chemical etching with BHF and high temperature annealing [99]. The surface was imaged by tapping mode AFM (Fig. 3.3).

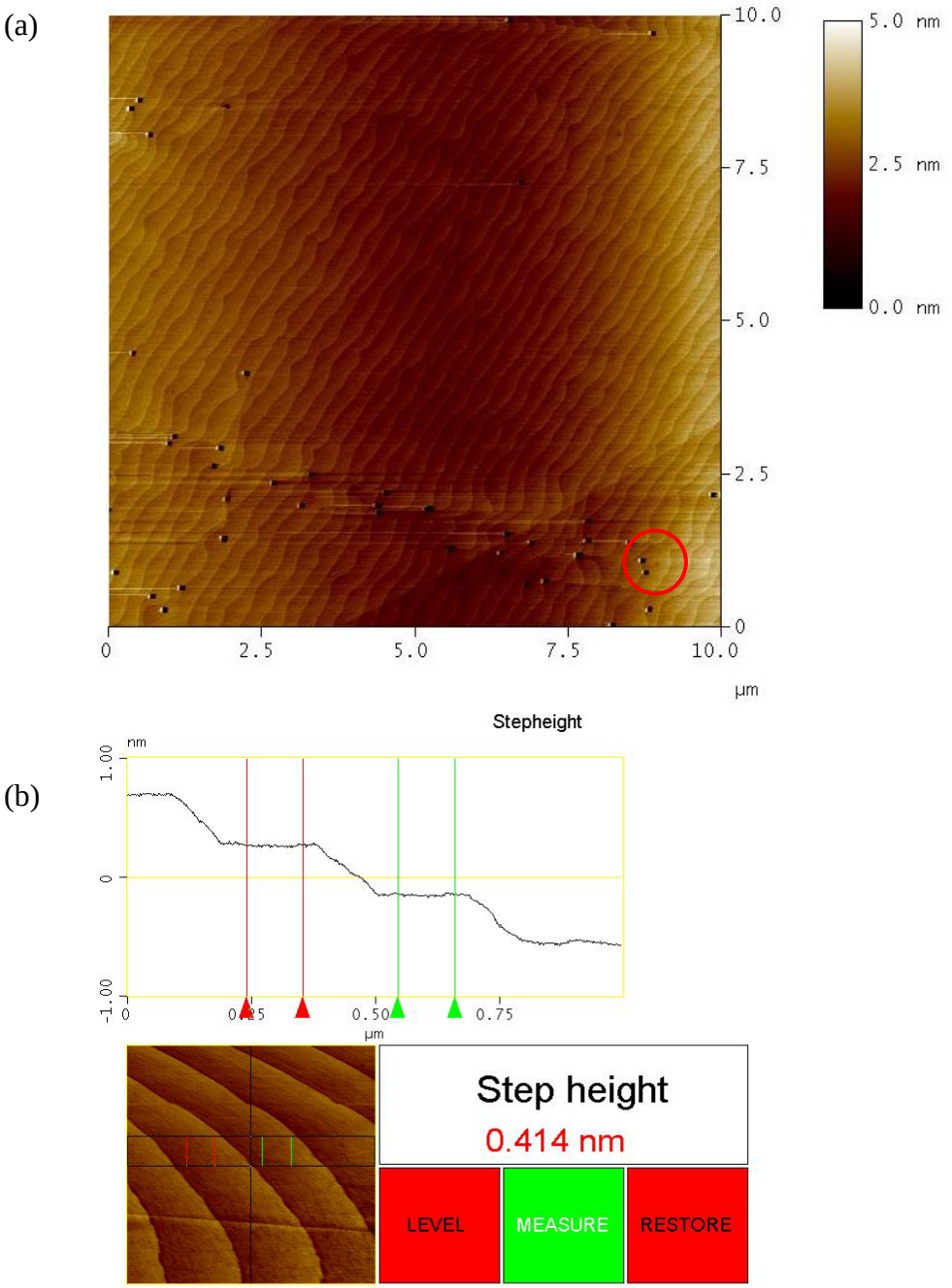

Figure 3.3 (a) AFM image of processed STO substrate [supplier: KMT, nominally exact (001)]. Black square dots (some are marked by a red circle) are probably etch pits. (b) surface with single-unit steps.

The black square dots in Fig. 3.3(a) are probably etch pits, which are difficult to eliminate entirely. However, their amount can be reduced by using diluted BHF. The measured step height is 0.414 nm, close to the STO unit cell parameter of 0.395 nm [Fig. 3.3(b)].

3.4. Epitaxial $SrRuO_3$ bottom electrode buffer layer

SRO has an orthorhombic unit cell with a pseudo-cubic lattice constant of 3.93 Å (Fig. 3.4). Its good conductivity and small lattice mismatch of -0.96% with BFO make it an ideal bottom electrode material.

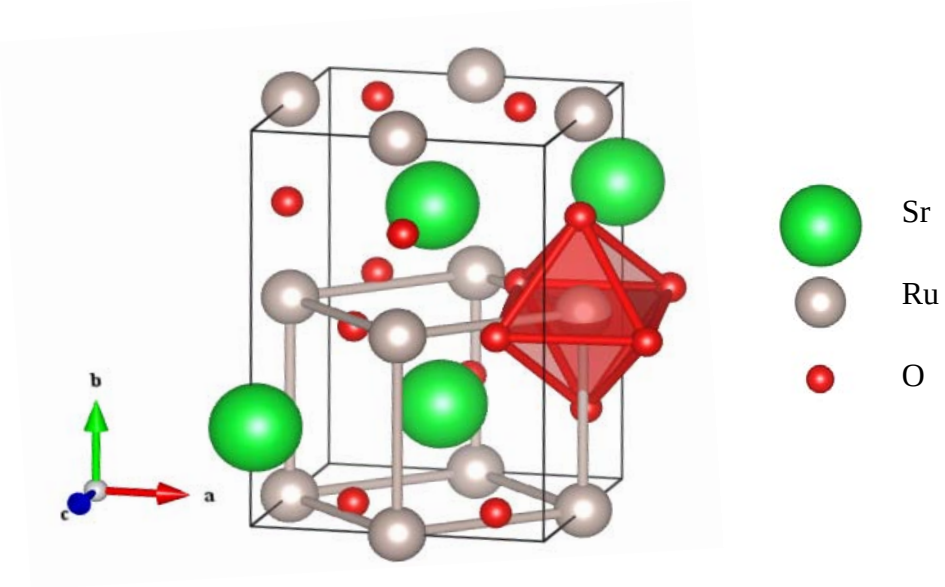

Figure 3.4 Orthorhombic unit cell of SRO with the pseudocubic cell shown in grey. One RuO_6 octahedron is illustrated (it is partially outside the unit cell).

3.4.1. RF magnetron sputter deposition of SRO thin films

The deposition conditions of epitaxial SRO films are summarized in Table 1. It has been found that a high working pressure improves the conductivity and the crystallinity of the SRO films [112]. In this project the working pressure was chosen to be as high as possible without causing the deposition rate to be impractically low.

Table 1. SRO Sputtering Condition							
System	Target size (inch)	Ar:O2	Power (W)	Temp (˚C)	Pressure (mTorr)	Rate (Å/min)	Thickness (nm)
ACL Oerlikon	2	3:1	70	680	20	5.6	60
IMRE Oerlikon	3	4:1	150	600	26.25	1.66	50

3.4.2. Crystalline structure

High quality epitaxial SRO films have been obtained (Fig. 3.5). The full-width at half-maximum (FWHM) of the (002) peak from HRXRD scan is 0.09°. The out-of-plane pseudo-cubic unit cell lattice spacing $d_{(001)pc}$ is about 3.978 Å, larger than the bulk value of 3.924 Å, due to the in-plane compressive strain.

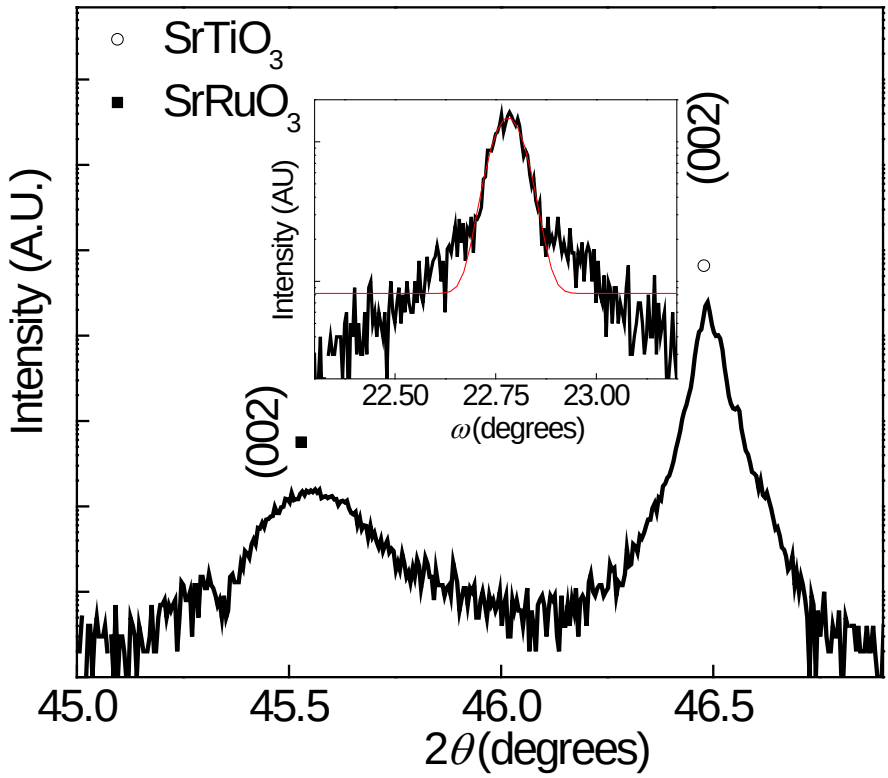

Figure 3.5 HRXRD scans of SRO/STO(001). Inset shows the ω-scan of the SRO peak.

3.4.3. Surface morphology

The AFM measurement shows a very smooth surface of the SRO films deposited on the STO(001) substrates. The root-mean-square roughness R_a is 0.214 nm and 1.176 nm for SRO on STO(001) and on STO(111) substrates, respectively. SRO deposited on STO(111) shows island growths. The surface of SRO/STO(001) shows probable 3D island growth rather than pure step flow growth even though the substrates are vicinal. This is probably because the adatom diffusion length is short compared to the terrace length and they nucleate before they reach the ledge sites. At higher miscut angles, the terrace length is reduced and single mode step flow growth could be achieved [113]. However it is much harder to prepare vicinal STO substrates with high miscut angles, and they are not used in this project due to the formation of severe step bunching.

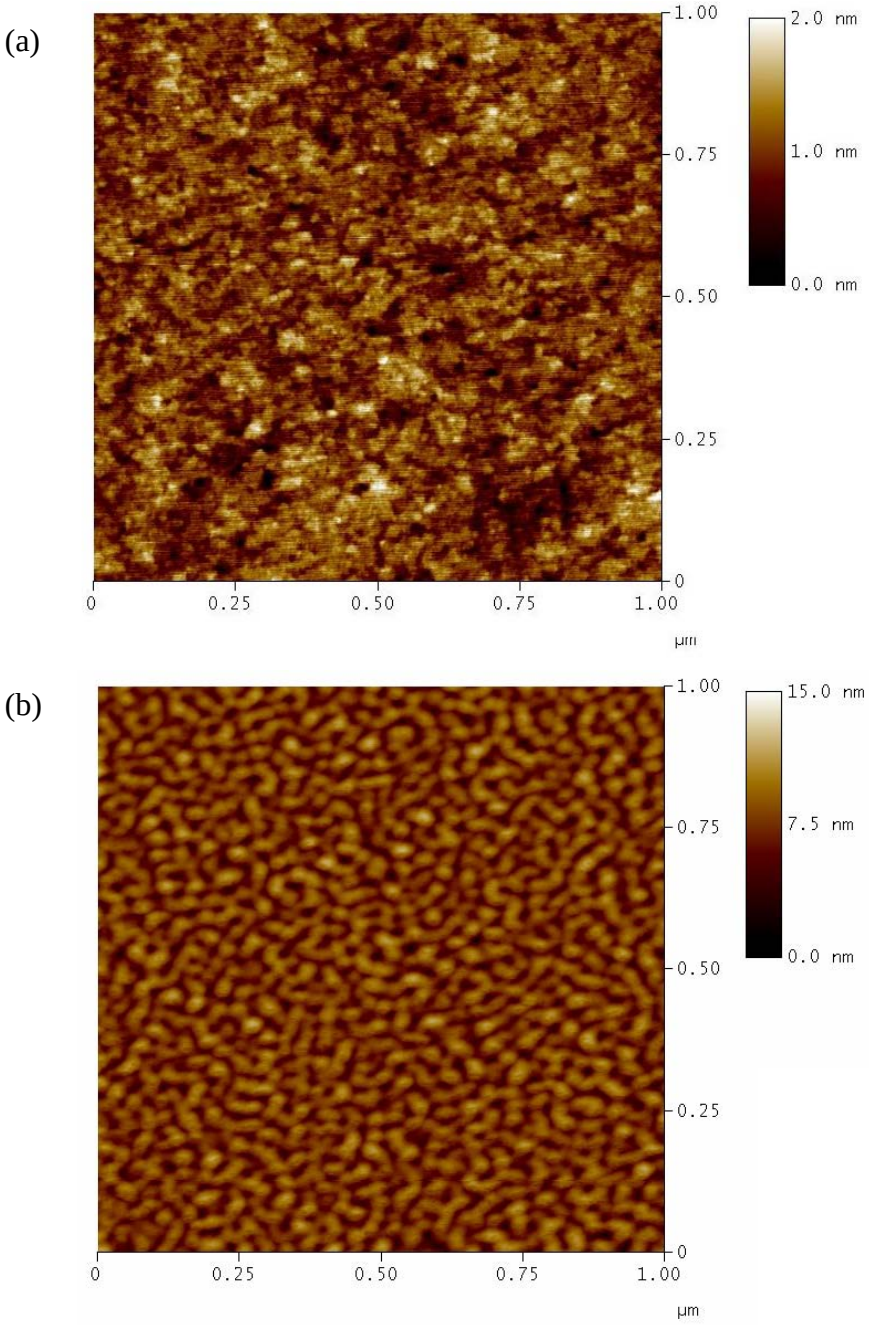

Figure 3.6 AFM images of (a) SRO/STO(001) and (b) SRO/STO(111).

3.4.4. Electrical properties

The electrical property of the SRO layer was measured by the Hall System. The conductivity is 1.33 mΩ cm, comparable to other reports of SRO thin-film samples [112, 114]. The sheet resistance is about 221.8 Ω/□. The Hall coefficient is positive but very small (on the order of 10^{-11} m^3/C), similar to the values in Ref. [115]. It has

been shown that SRO is a highly compensated material [116]. Thus it is not possible to obtain meaningful information on the carrier density and mobility from the Hall measurement alone.

3.5. Epitaxial $BiFeO_3$ films

BFO thin films were deposited by RF magnetron sputtering using the Oerlikon sputtering systems at ACL and IMRE, and the UBM sputtering system at IMRE. High quality epitaxial BFO films with good ferroelectric properties are obtained. The growth conditions are summarized in Table 2.

Table 2. BFO Sputtering Condition

System	Target size (inch)	Ar:O2	Power (W)	Temp (˚C)	Pressure (mTorr)	Rate (nm/min)
ACL Oerlikon	2	7:1	120	680	5.6	1.88
IMRE Oerlikon	2	9:1	120	570	6.1	0.55
IMRE UBM	4	10:1	250	600	12	1.86

3.5.1. Crystalline structure

The HRXRD measurements show a FWHM of 1.08° for the $(002)_{pc}$ peak of the epitaxial BFO films obtained from ACL (Fig. 3.7). Twinning structures are observed from the reciprocal space mapping (RSM) (Fig. 3.8). The split of the (110) peak is clearly seen in Fig. 3.8(a). The split of the (002) peak is not observed here. It is possible that the low intensity of the signal makes it difficult to resolve individual (002) peaks here. The formation of the twinning structures in BFO thin films can result in reduced leakage current and improved ferroelectric properties [117].

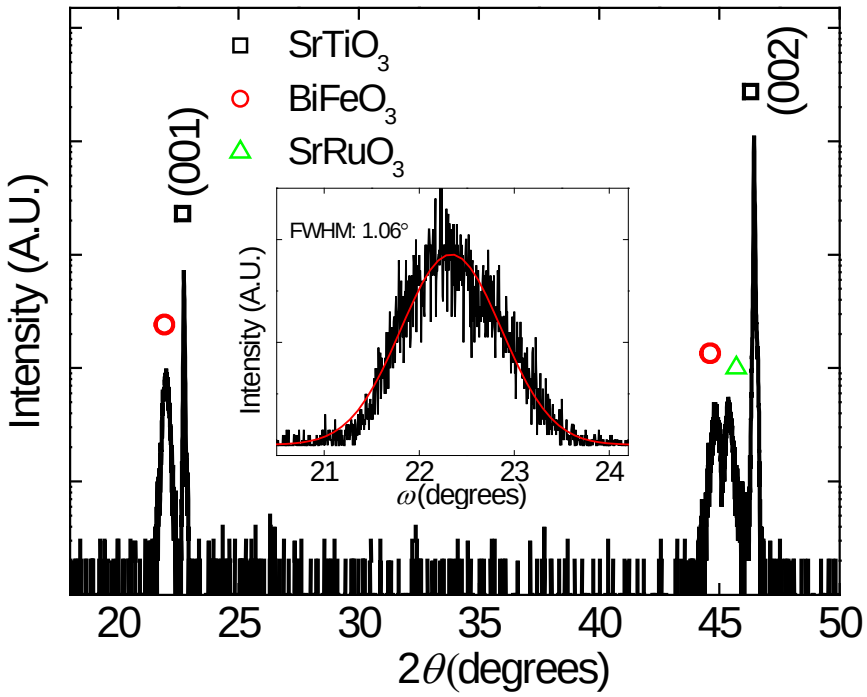

Figure 3.7 HRXRD scans of BFO/SRO/STO(001) results of BFO films. Inset shows the ω-scan of BFO(002) peak.

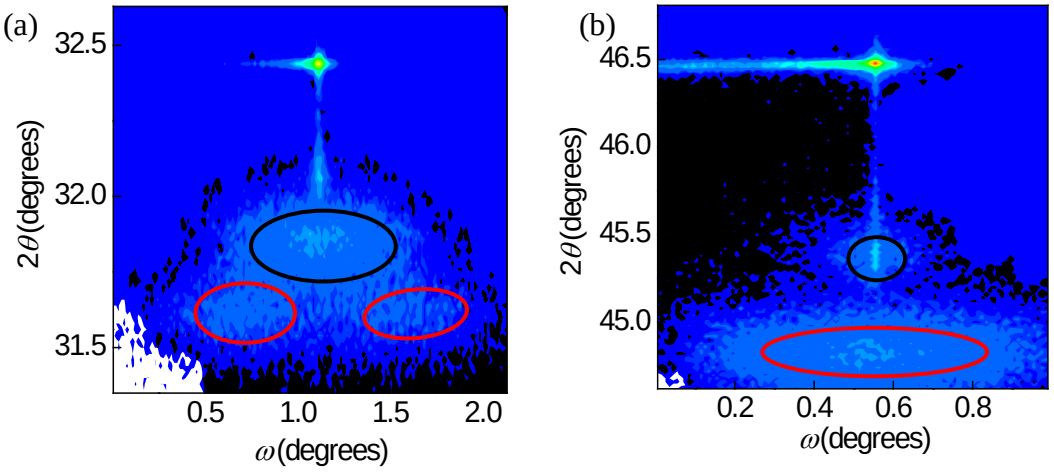

Figure 3.8 RSM of BFO (170 nm)/SRO/STO(001) of (a) (110) and (b) (002) diffractions. Black circles: SRO, and red circles: BFO.

High quality epitaxial BFO films have been successfully obtained from the UBM sputtering system in IMRE as well. The deposition temperature was optimized (Fig.

3.9). It is found that the iron-rich phase $Bi_2Fe_4O_9$ starts to form at above 720 ˚C due to Bi volatility. At 760 ˚C, BFO completely disappears and only $Bi_2Fe_4O_9$ exists. Pure BFO phase is obtained at below 680 ˚C. As the temperature goes down, the out-of-plane lattice parameter increases, indicating better epitaxial quality due to coherent strains. However, at 560 ˚C the BFO peaks become very weak as a result of the poor crystallinity. The optimal deposition temperature is found to be 600 ˚C.

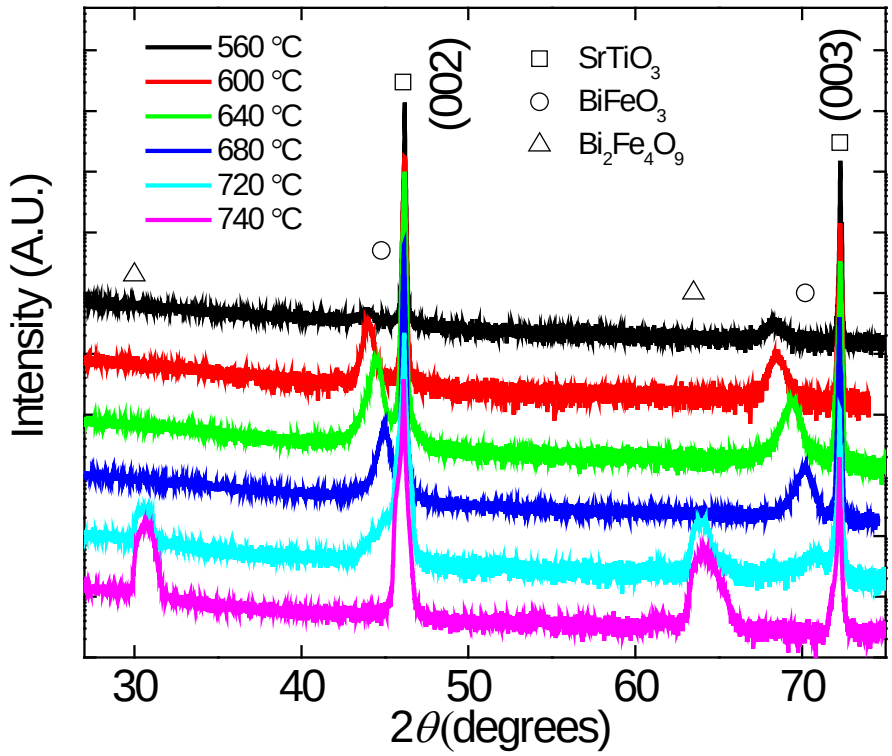

Figure 3.9 HRXRD of BFO/STO(001) at different deposition temperatures.

On the STO(001) substrates, the out-of-plane lattice unit cell parameter $d_{(001)pc}$ of BFO is about 4.095 nm for the 135-nm-thick film [Fig. 3.10(a)], larger than the single crystal parameter of 3.968 nm. This is due to the in-plane compressive strain. It is interesting to notice that the BFO on SRO-buffered STO(001) shows a strain-induced T phase with a very large out-of-plane lattice parameter. Those 20-nm-thick films are entirely made of this phase, while at the 135-nm-thick films show an R-phase with a

smaller out-of-plane parameter. At 40 nm, it is a mixture of both phases. The existence of the T phase in BFO thin films has been reported by other researchers [118, 119], but only on substrates with a much larger lattice mismatch with BFO than STO, such as $LaAlO_3$ (LAO). Recently Liu et. al. reported the observation of the T-phase BFO on SRO-buffered STO substrates. By using high resolution synchrotron XRD, they showed that the formation of this phase is induced by the formation of the parasitic Bi_2O_3 layer near the substrate [120]. No Bi_2O_3 phase is observed in the XRD results here but its existence could not be ruled out due to the much weaker XRD signals here. At the thickness of 135 nm, only the R phase is observed. The BFO lattice is relaxed further in thicker films. At the thickness of 446 nm, the BFO peaks are merged together with the SRO peaks. The out-of-plane lattice unit cell parameter of these thickest films is about 4.034 nm.

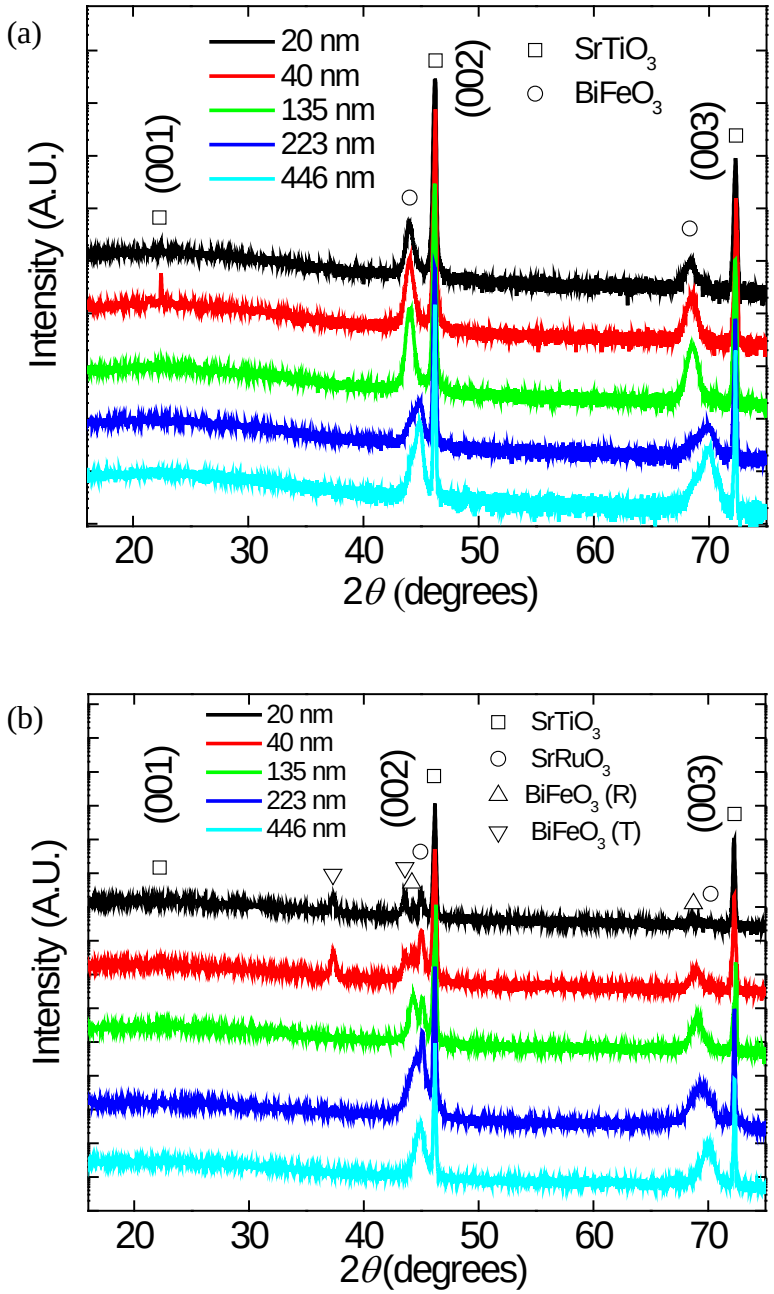

Figure 3.10 HRXRD spectra of (a) BFO/STO(001) and (b) BFO/SRO/STO(001)

Epitaxial BFO films are also obtained on STO(111) substrates (Fig. 3.11). Reciprocal space mapping (RSM) is used to characterize the crystal structure (Fig. 3.12). In RSM, a series of Gonio scans at different ω angles are carried out to map one section of the reciprocal space. High resolution RSM can reveal peak splittings, which are used for

the precise determination of the film crystal structure. The interplanar spacing d is calculated from the Bragg law $d = 2\sin\theta/\lambda$. In the 466-nm-thick film, the interplanar spacings $d_{(006)h}$ and $d_{(024)h}$ are 2.312 Å and 1.985 Å, respectively. In the 40-nm-thick film, $d_{(006)h}$ and $d_{(024)h}$ are 2.312 Å and 1.984 Å, respectively. They are almost the same as the values reported for bulk BFO [121]. This shows that the BFO films grow epitaxially on the STO(111) substrates with a rhombohedral structure for all the samples [122].

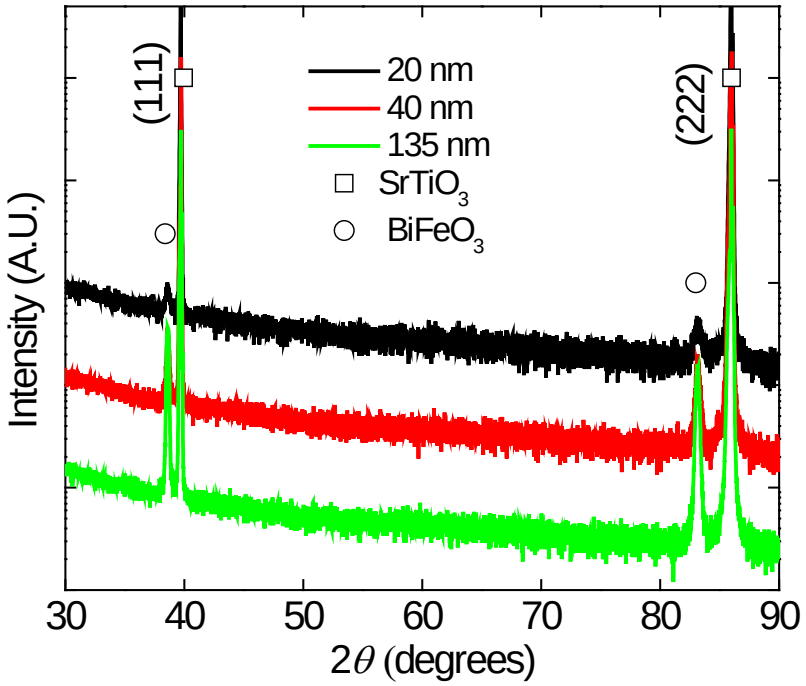

Figure 3.11 HRXRD Gonio scan of BFO/STO(111) sample deposited using UBM.

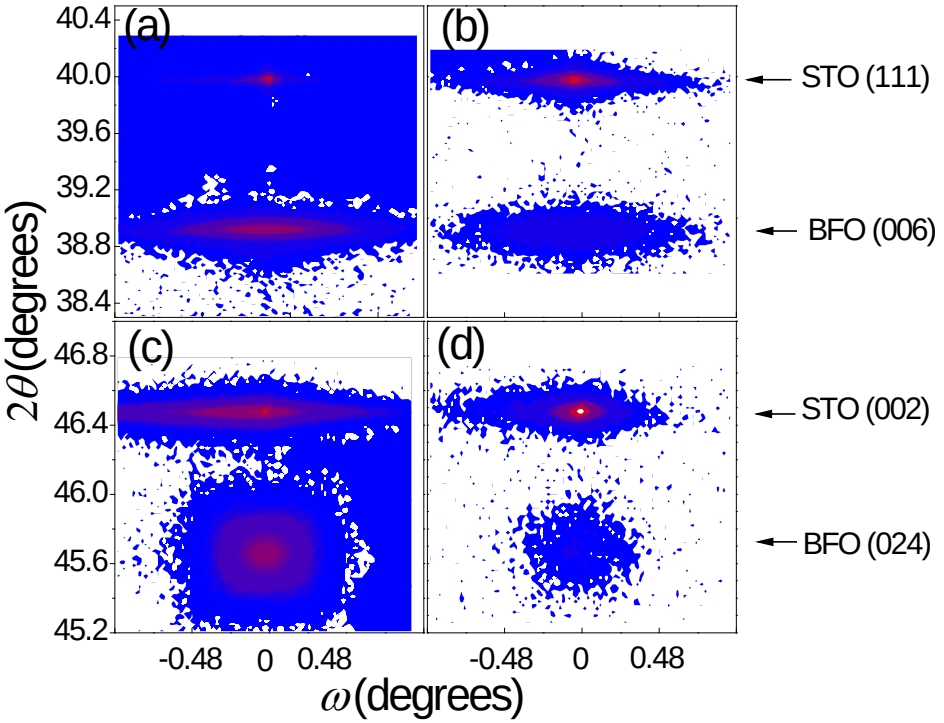

Figure 3.12 RSM of epitaxial BFO thin films on STO substrates: (a) (111) 446-nm film, (b) (111) 40-nm film, (c) (002) 446-nm film and (d) (002) 40-nm film.

3.5.2. Surface morphology

The surfaces of the BFO films have been characterized by the AFM and the SEM. The surfaces of the BFO films deposited on the STO and the SRO-buffered STO show regular square features (Fig. 3.13). The root-mean-square roughness R_a for the 135-nm thick films is about 0.351 nm for films on SRO-buffered STO(001) and 0.378 nm for those directly on STO(001).

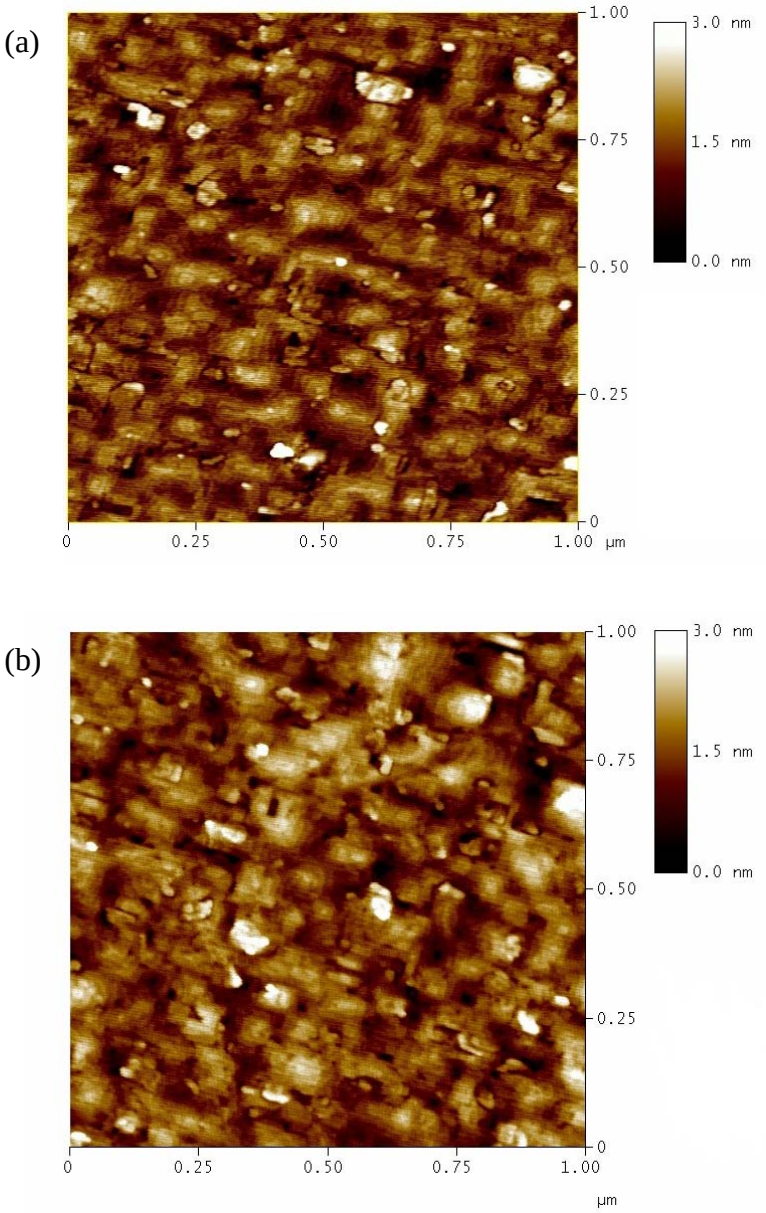

Figure 3.13 AFM images of 135-nm-thick BFO film on (a) STO(001) and (b) SRO/STO(001).

The topography of BFO on the STO(111) substrates (Fig. 3.14) is very different from those on the STO(001) substrates. It shows 3D island growth, similar to the topography of the SRO bottom electrode. The root-mean-square roughness R_a is about 5.238 nm and 5.982 nm for the 135-nm thick film on the SRO-buffered STO(111) and the bare STO(111) substrates, respectively.

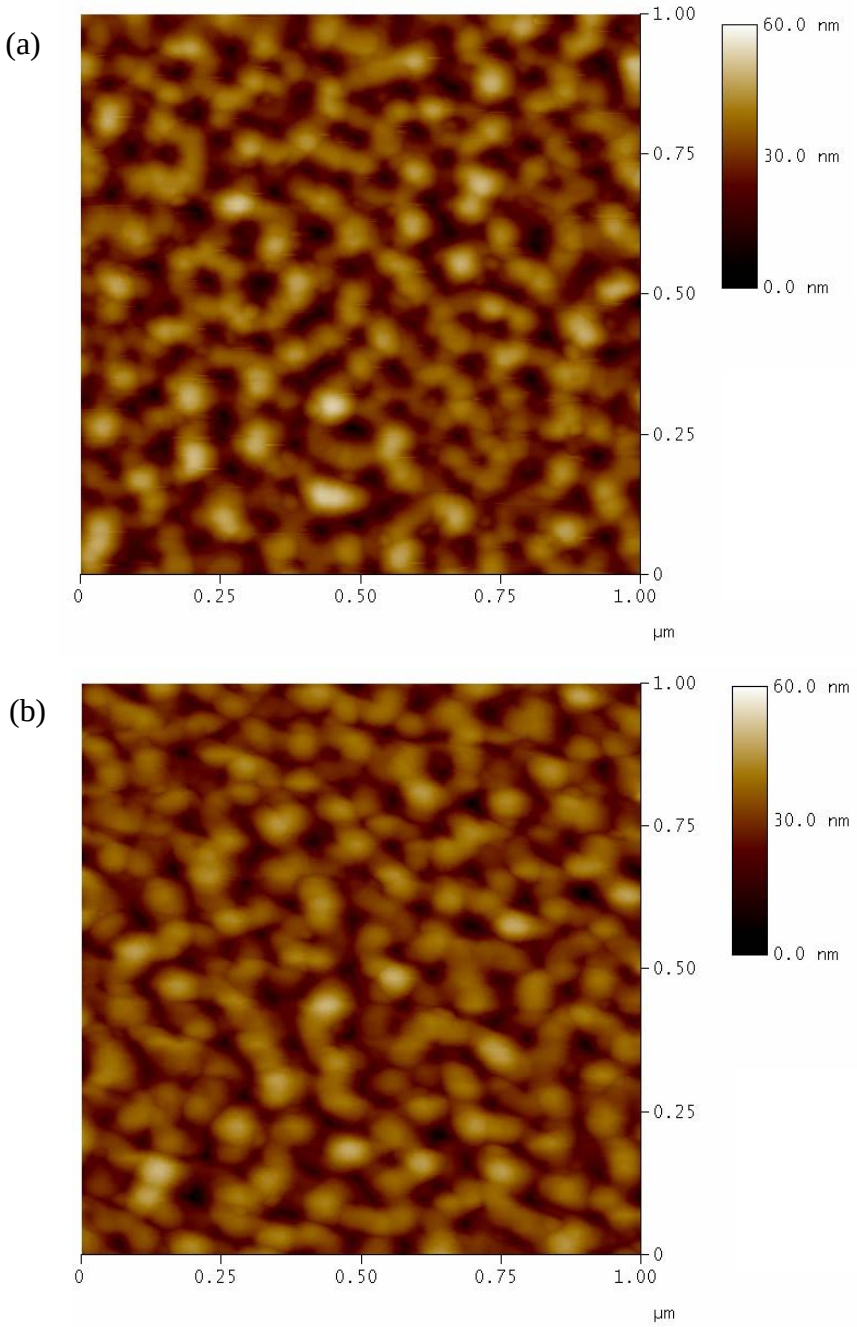

Figure 3.14 AFM images of 135-nm-thick BFO film on (a) STO(111) and (b) SRO/STO(111).

The surface of BFO on SRO/STO(111) is also inspected by SEM (Fig. 3.15). Dense uniform grains of about 100-nm wide are observed. In some areas, there are some larger grains of about 200 to 300 nm in diameter. They appear to have a six-fold symmetry in-plane, as can be expected from the three-fold [111] axis of BFO.

(a)

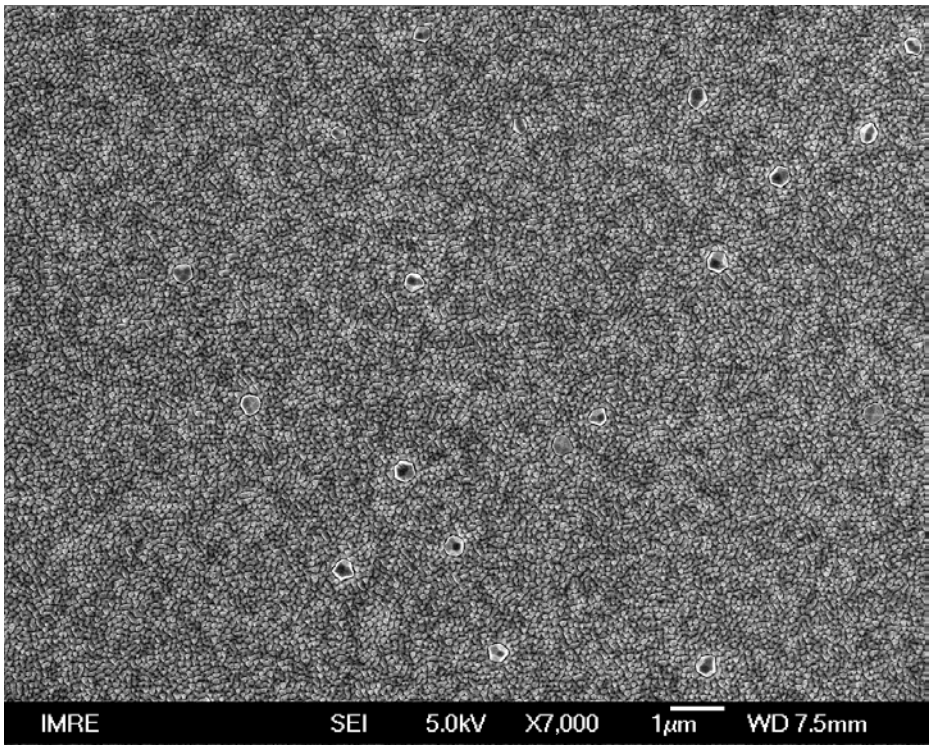

(b)

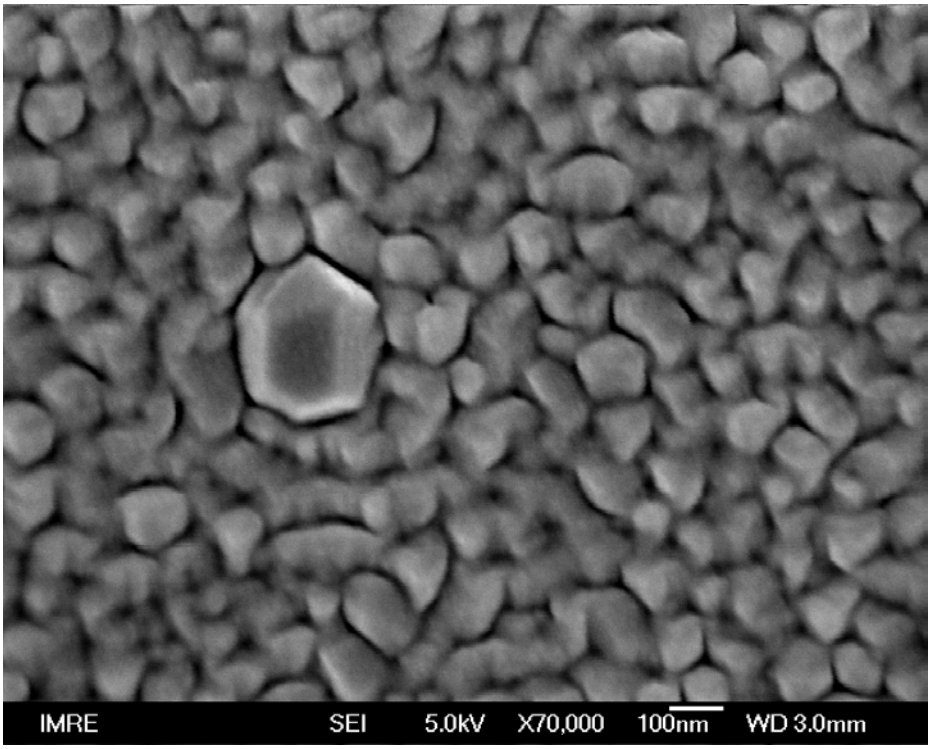

Figure 3.15 SEM images of BFO/SRO/STO(111) at (a) 7000 and (b) 70,000 magnification.

3.5.3. Dielectric properties

The dielectric constants are calculated from the impedance measurement. Samples with small loss factors, on the order of 10^{-2} or less, are used to minimize the effects from interfacial polarization and DC conductivity [123]. It is found that the low frequency dielectric constant ε' increases with the film thickness from an average of 61.7 for the 135-nm-thick films to about 89.7 for the 446-nm-thick films (Fig. 3.16). As shown in Fig. 3.10, thinner films are compressively-strained. Consequently, their polarizability is decreased and the dielectric constants are reduced. The thicker films are more relaxed and their dielectric constants are close to the reported values in the literature [123, 124]. Because BFO is considered as a hard ferroelectric with a high Curie temperature [125], it is not surprising to find such small values for the dielectric constant.

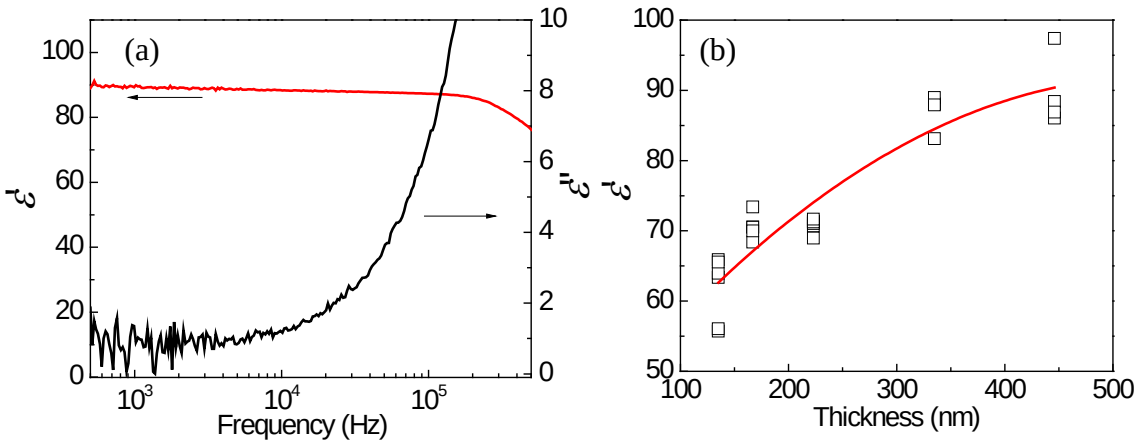

Figure 3.16 Dielectric constants of BFO/SRO/STO(001) films. (a) Dielectric constants vs. frequency in a 446-nm-thick film and (b) dielectric constant at 1 kHz vs. film thickness.

3.5.4. Optical properties

The optical bandgap of the BFO films are measured by UV-visible absorption spectroscopy. The result is plotted in Fig. 3.17(a) and a direct bandgap of 2.72 eV is obtained from the linear extrapolation to $(\alpha\varepsilon)^2 = 0$. The photocurrent spectral response shows a maximum current density near the band absorption edge of 2.7 eV (460 nm) [Fig. 3.17(b)].

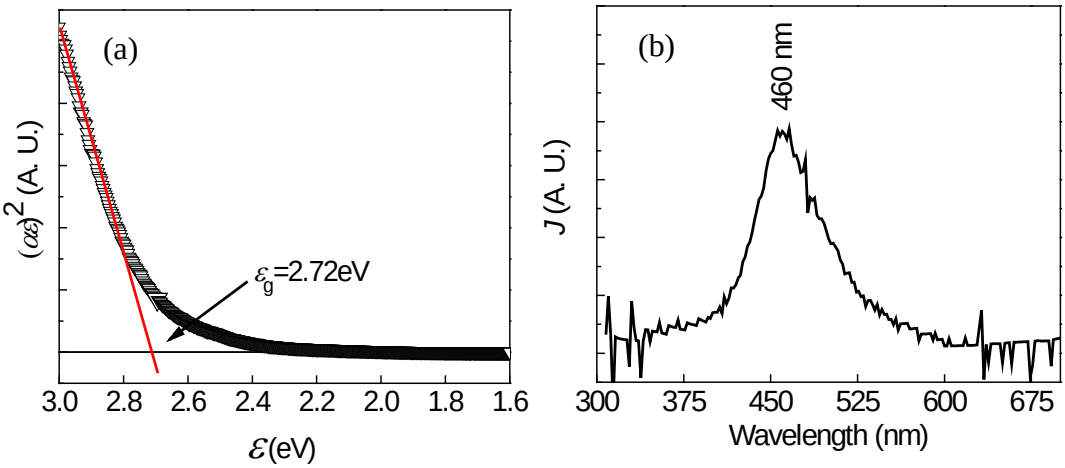

Figure 3.17 (a) Plot of $(\alpha\varepsilon)^2$ vs. photon energy ε of the UV-visible absorption spectrum of the BFO film. The linear extrapolation gives a direct bandgap of 2.72 eV. (b) Spectral response of the short-circuit photocurrent (J_{sc}) of the BFO film, showing a maximum response at 460 nm, corresponding to 2.7 eV.

The refractive index of BFO is measured by spectroscopic ellipsometry. BFO film of 400-nm thickness is prepared on STO(001) substrates. Ellipsometric spectra were collected between 55° and 70° incident angels at an interval of 5°. The result is fitted to a three-layer optical model consisting of a 0.5-mm-thick STO substrate , the bulk film and a surface roughness layer modeled by a Bruggeman effective-media approximation with 50% void and 50% bulk film. The dielectric function parametrization of BFO consists of four Tauc-Lorentz oscillators with a common bandgap [85]. The refractive index and extinction coefficient are extracted from

fitting the ellipsometric spectra to the optical model (Fig. 3.18). The film thickness is fitted to 401.67 ± 0.76 nm. The reflective index at 465 nm is about 3.09, giving an optical dielectric constant of about 9.55.

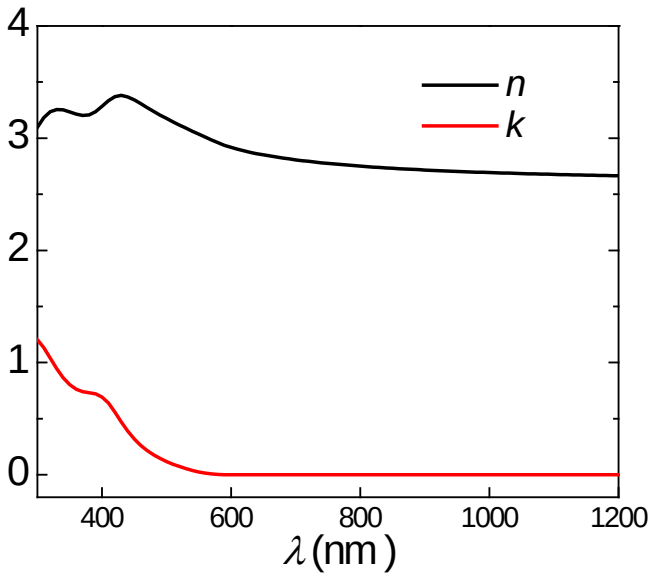

Figure 3.18 Refractive index n and extinction coefficient k extracted from the spectroscopic ellipsometric data.

3.5.5. Ferroelectric properties

Saturated *P-E* hysteresis loops with minimum leakage currents are obtained. The remanent polarization P_r is more than 65 μC/cm^2 in samples of BFO(001) with Au top electrodes from ACL (Fig. 3.19). At low electric fields the hysteresis loops are shifted to the positive side of the *E*-axis, indicating a negative self-polarization (polarization vector pointing to the film surface).

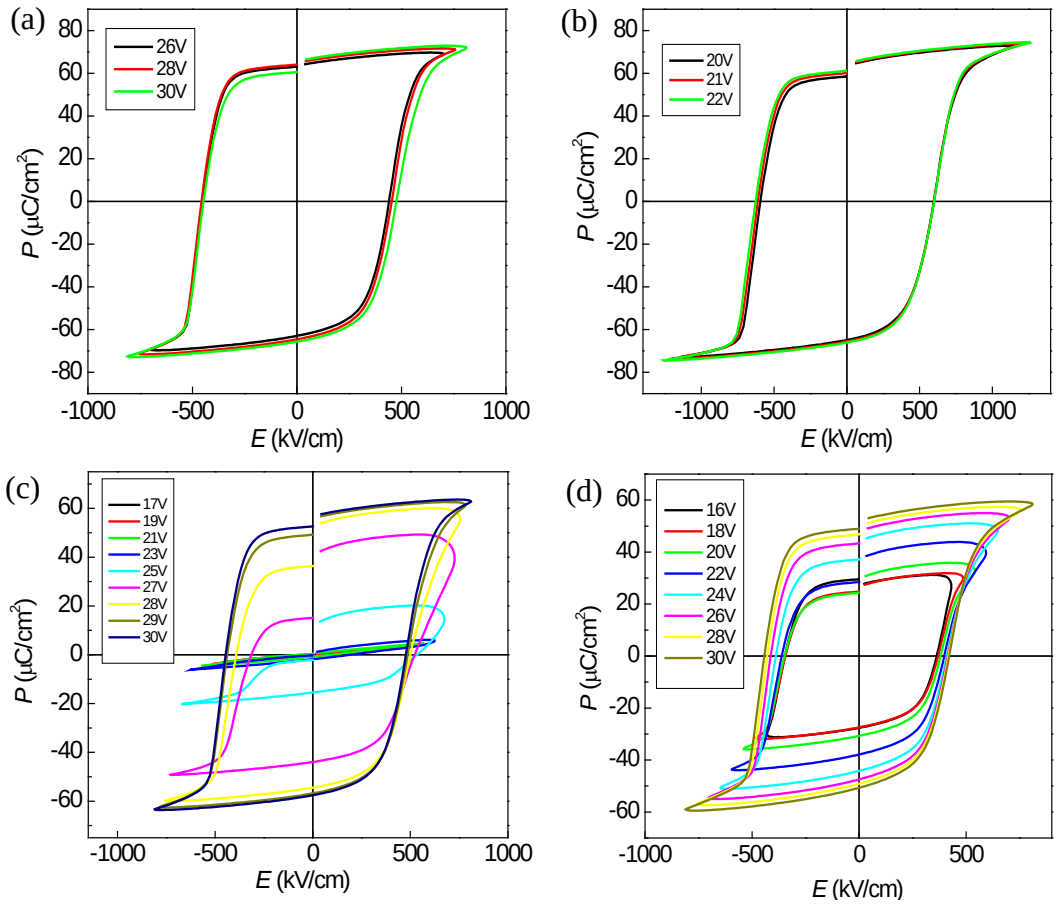

Figure 3.19 *P-E* hysteresis loops measured at 10 kHz. Bias is applied on the top electrode. (a) BFO film with Au top electrode. (b) BFO film with ITO top electrode. (c) A series of hysteresis loops for a BFO film measured with increasing maximum voltage starting from its virgin state. At low field, the hysteresis loop is offset to the positive side of the *E*-axis, showing that polarization in the as-deposited film points to the top electrode. At high field, the hysteresis loop becomes almost symmetric. This occurs since the self-polarized domains could not be reoriented by the low electric fields, but could be rotated at higher fields. (d) Hysteresis loops of the same device as in (c), after high field cycling. The *P-E* loops remain symmetric even when measured at low electric fields.

Samples from UBM show a P_r of 84.9 μC/cm^2 and 108.5 μC/cm^2 for the (001)-oriented and the (111)-oriented BFO films, respectively (Fig. 3.20). The values of the P_r obtained here are consistent with the theoretical prediction of 90 to 100 μC/cm^2 by first principles calculations [19]. The *P-E* loops have a small offset towards the positive *E*-axis, similar to the results obtained at ACL, indicating these films are also negatively self-polarized. The leakage current does show up in the hysteresis loops of

the BFO(001) samples, most probably as a result of the large electric field used for the measurements. The coercive fields increase at higher frequencies [126], leading to unsaturated hysteresis loops (Fig. 3.21). However, the weak dependence of the P_r on the measurement frequencies and the voltages indicates that the ferroelectric polarization switches are intrinsic [127].

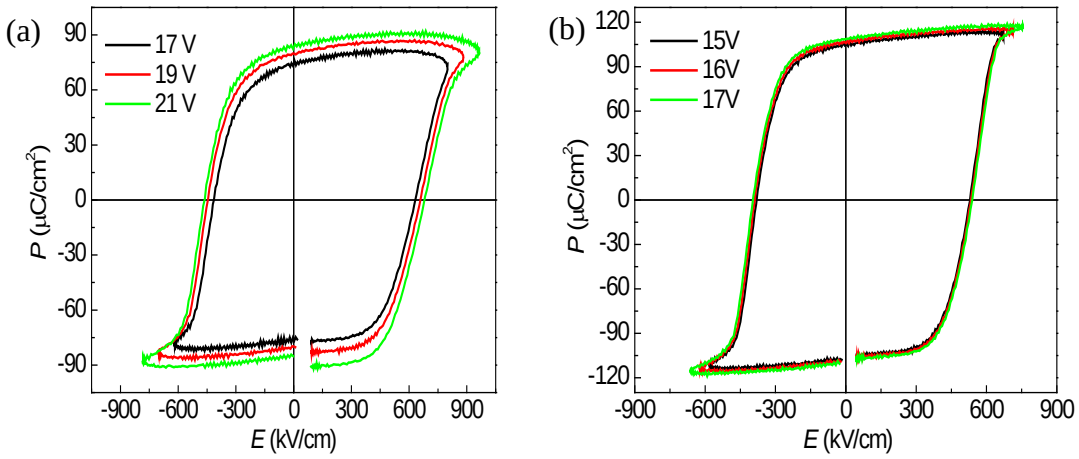

Figure 3.20 *P-E* hysteresis loops of 223-nm-thick BFO samples from UBM. (a) BFO/SRO/STO(001) and (b) BFO/SRO/STO(111). Measurement frequency is 5 kHz.

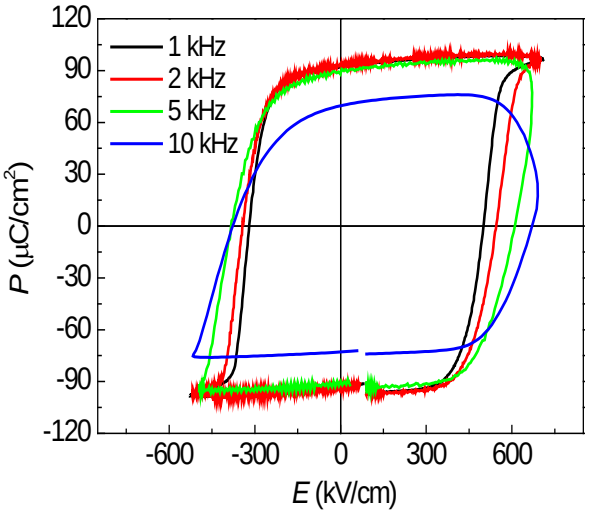

Figure 3.21 Frequency dependence of the *P-E* hysteresis loops of BFO/SRO/STO(111).

The electrical leakage in BFO is often believed to originate from oxygen vacancies, which cause the Fe ions to have different valences. The valence states of the Fe ions are investigated by measuring the 3/2 and 1/2 spin-orbit doublet components of the Fe 2p states (Fig. 3.22). Only the Fe^{3+} peaks are observed, which are located at 711.1 and 724.6 eV for the 3/2 and 1/2 peaks, respectively [128]. This indicates a low density of oxygen vacancies and may be one of the reasons for the small leakage current in these samples.

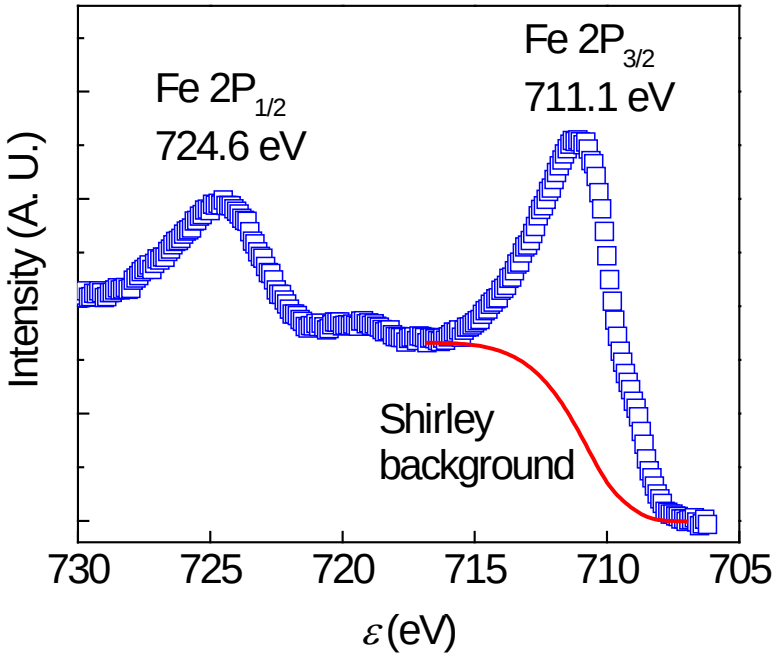

Figure 3.22 XPS spectrum of Fe 2p doublet in BFO films.

3.5.6. Piezoelectric properties

The piezoelectric properties of the BFO films were investigated with an LSV. It was found that the as-deposited films exhibit significant piezoelectric response, which confirms that they are self-polarized (Fig. 3.23). To determine the self-polarization direction, the displacement phase of the films was monitored and compared with the phase of the driving signal (Fig. 3.24). In this experiment, the driving AC signal was

applied on the top electrode with the bottom electrode grounded (Fig. 3.24 inset). The displacement phase is about -70˚ for both the as-deposited and the negatively-poled films. For the positively-poled films, the displacement phase is about -130˚. This shows that the self-polarization is pointing up to the top electrode, same as the negatively-poled film. In addition, the effective longitudinal piezoelectric coefficient d_{33} for both samples is about 30.9 pm/V, indicating that the as-deposited film is completely polarized during the deposition process.

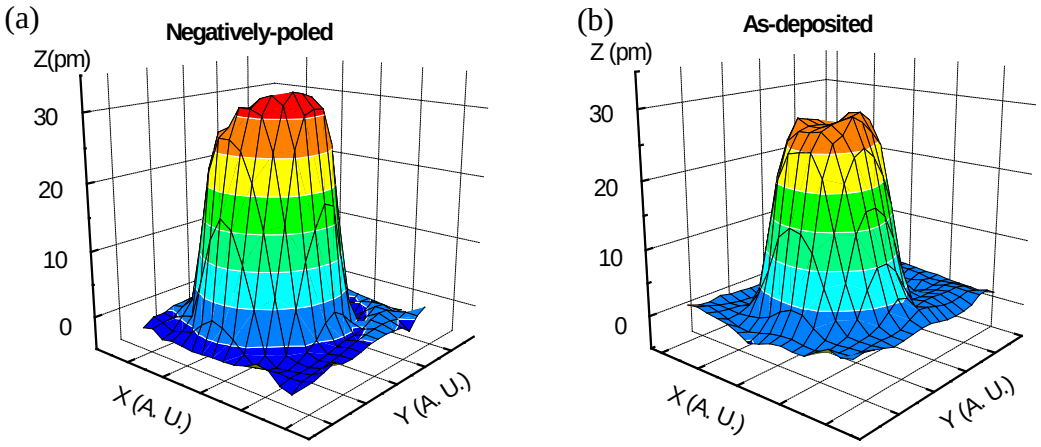

Figure 3.23 Piezoelectric displacements measured with an LSV for (a) negatively-poled and (b) as-deposited samples.

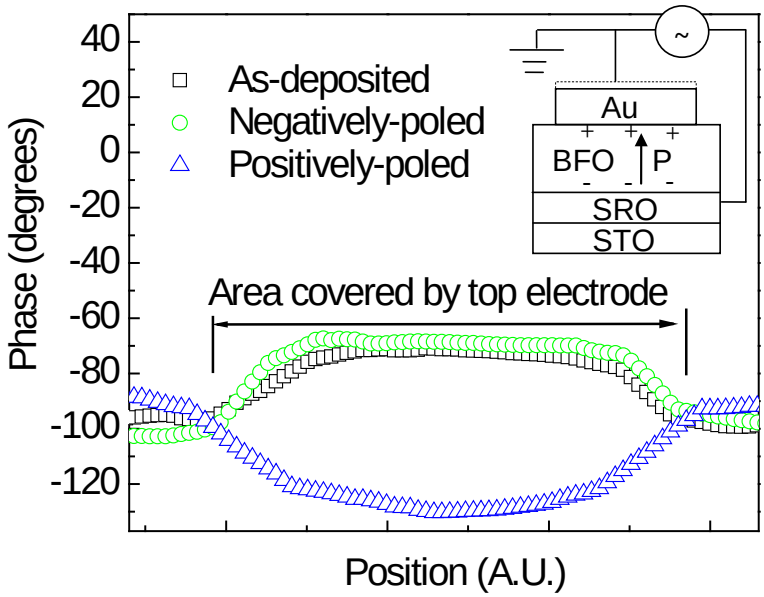

Figure 3.24 The phases of the piezoelectric displacements for the as-deposited and the poled BFO thin-film samples measured with an LSV. The as-deposited sample shows similar phase as that of the negatively-poled sample, while the positively-poled sample is out of phase. The inset shows a schematic of the experimental setup with the negatively-poled BFO film. During the positive cycle of the driving signal, the film covered by the Au top electrode expands in thickness direction, as illustrated by the dotted line.

Self-polarization in as-deposited ferroelectric films can be caused by many factors [129]. The Schottky barrier field is excluded since leakage current measurements (Fig. 4.3) show that the barriers at the two electrode interfaces are comparable and opposite (Fig. 4.7). The *P-E* hysteresis loop measurement shows that the self-polarization is removed and un-recoverable after high field cycling (Fig. 3.19). It is believed that the self-polarization occurs during the sputtering process but the exact mechanism is not yet clear.

3.6. Conclusions

High quality epitaxial BFO films have been successfully obtained on both bare and BFO-buffered STO substrates with magnetron sputter deposition. The BFO/SRO/STO(001) samples show a mixture of the T phase and the R phase below the thickness of 40 nm, while only the R phase is observed for films thicker than 135 nm. The films are compressively strained and the out-of-plane unit cell parameter is 4.084 nm and 4.034 nm for films of thickness of 135 nm and 446 nm, respectively. The films show smooth surface with regular square features. BFO deposited on STO(111) substrates show rhombohedral structure similar to that of the bulk single crystal and the surface shows 3D island growth.

The low frequency dielectric constant ε' increases with film thickness from an average of 61.7 for 135-nm-thick films to about 89.7 for 446-nm-thick films, accompanied by the relaxation of the in-plane strain. The refractive index at 465 nm is about 3.09, giving an optical dielectric constant of about 9.55.

Absorption spectroscopy shows the BFO thin films have a direct bandgap of 2.72 eV. BFO is one of the few ferroelectric materials with a direct bandgap in the visible light region of the electromagnetic spectrum.

The BFO samples show a large ferroelectric polarization [up to 108.5 $\mu C/cm^2$ in the BFO(111) films] with a minimum leakage current. The samples are found to be self-polarized with negative polarization (i.e., the polarization vector pointing to the film surface). The effective longitudinal piezoelectric coefficient d_{33} for both poled and self-poled samples is about 30.9 pm/V.

The high quality BFO films with a large ferroelectric polarization and a bandgap in the visible light spectrum provide the basis for the studies of the PV effect in ferroelectric thin films. Furthermore the self-polarization observed in this films can facilitate direct device applications as the poling process can be eliminated.

Chapter 4. Effect of polarization on the photovoltaic responses of $BiFeO_3$ thin films

4.1. Introduction

While silicon-based diodes have been the dominant solar cell type, novel photovoltaic mechanisms [130, 131] are being explored in pursuit of lower cost or improved efficiency. In a semiconductor photodiode, such as a Si solar cell, photons with higher energies than the bandgap are absorbed to produce electron-hole pairs, which are separated by the internal electric field in the p-n junction and then collected by the electrodes. However, a p-n junction is not a prerequisite for photovoltaic effect. For exitonic solar cells, photon absorption creates excitons, which dissociate at a heterojunction [52]. In materials without a center of symmetry, such as ferroelectric materials, the BPVE can cause steady-state photocurrents in a homogeneous medium under uniform illumination [55].

The photovoltaic effect in ferroelectric materials has many unique features, such as large photovoltages above the energy bandgap [54], photocurrents proportional to the polarization magnitude [132], and charge carrier separations in homogeneous media [55]. Observed in bulk ferroelectrics in as early as 1950s [53], the PV effects in ferroelectric materials have seen a resurgent interest recently, especially in ferroelectric thin films. It has been proposed that remarkably higher photovoltaic efficiency can be achieved in thin films [68, 70]. On the other hand, open-circuit voltages much larger than the bandgap have also been achieved in ferroelectric thin films with in-plane interdigital electrodes [79], which has led to the development of UV sensors and dosimeters [80].

As reviewed earlier, the relatively small direct bandgap, high absorption coefficients, and a large remanent ferroelectric polarization make BFO an ideal material for the investigation of the PV effect in ferroelectrics. Recently switchable diode effect and visible light photovoltaic effect have been observed with BFO bulk crystals [86]. However, no significant photovoltaic response or any value of photovoltage has been reported for ferroelectric BFO films prior to this study. It is also unclear if the photovoltaic response in BFO is due to the Schottky junctions, the depolarization field, the BPVE, or any other mechanisms. Here I study the photovoltaic effect in epitaxial BFO thin films and obtain an open-circuit voltage V_{oc} as high as 0.55 V. I further demonstrate that the photocurrent direction can be switched by the polarization direction of the BFO film, and that the ferroelectric polarization contributes significantly to the observed photovoltaic effect. Moreover, the as-deposited BFO films are self-polarized, and they could readily function as a photovoltaic cell without any poling.

4.2. Hypotheses

Pintilie and Alexe investigated the ferroelectric properties on the photovoltaic effect in a ferroelectric thin film sandwiched by metal electrodes [73]. By treating the ferroelectric polarization as a sheet charge located within the ferroelectric at a finite distance from the electrode interface, they formulated that the built-in filed of the Schottky junction formed at the ferroelectric-electrode interface can be modified by the ferroelectric charges. Adapting their model for a p-type semiconductor, the modified built-in field for an n-type semiconductor is

$$V_{bi} = V_{bi}^{0} \pm \frac{P}{\varepsilon_0 \varepsilon'} \zeta, \qquad 4\text{-}1$$

where the superscript 0 denotes the built-in field without the influence of the ferroelectric polarization, and ζ is the thickness of the interface layer [73]. The built-in potential is reduced if the polarization charges and the charges in the depletion region have the same sign. It is increased if they have different signs.

The ferroelectric polarization has a large impact on the Schottky barrier height as well. The modified SBH is

$$\Phi_{SB} = \Phi_{SB}^{0} \pm \sqrt{\frac{qP}{4\pi\varepsilon_0^2\varepsilon_\infty\varepsilon'}}, \qquad 4\text{-}2$$

where the superscript 0 denotes the SBH without the influence of the ferroelectric polarization [133]. The modified SBH is reduced if the polarization charges and the charges in the depletion region have the same sign. It is increased if they have different signs.

The work function for ITO and SRO is 0.43 and 0.48 eV, respectively. BFO is normally n-type due to oxygen vacancies. Because the BFO films used in this work are insulating, their Fermi level is expected to be slightly higher than the middle of the bandgap, at around 4.6 eV below the vacuum level. The band alignment is shown in Fig. 4.1 according to the Schottky-Mott theory. Both the bottom and the top electrodes form Schottky junctions with BFO that would produce a positive photocurrent (i.e., it flows out of the bottom electrode). With the negative polarization (i.e., the polarization vector points from the bottom electrode to the top electrode), the depolarization field is in the same direction as the built-in fields of both Schottky junctions. The photocurrents from the depolarization field and the Schottky barriers are in the same direction. As a result, they add up to improve the efficiency. With a

positive polarization, the photocurrents are in the opposite directions and should cancel each other.

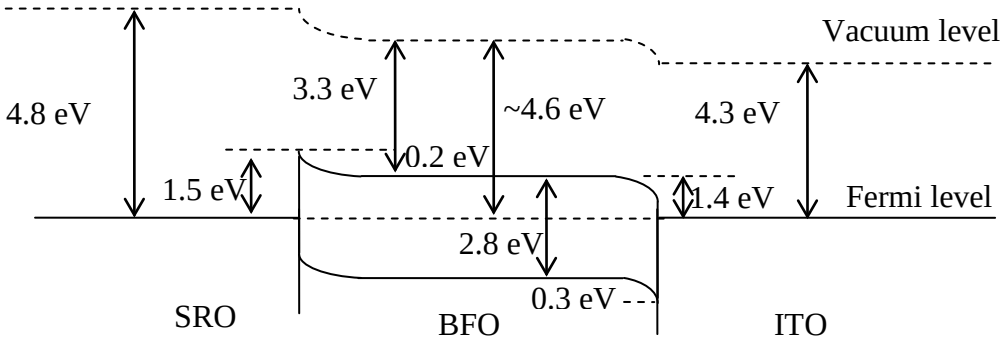

Figure. 4.1 Band alignment for ITO/BFO/SRO at equilibrium according to the Schottky-Mott theory.

The low frequency dielectric constant ε' is about 67 for the 170-nm-thick BFO films (Fig. 3.16). The optical dielectric constant ε_∞ of BFO is 9.55 as calculated from the refractive index in Fig. 3.18. The remanent polarization P_r is 84.9 μC/cm^2 (Fig. 3.20). The SBH change due to the ferroelectric polarization is therefore about 0.42 eV according to Eq. (4-2). The thickness of the interface layer ζ is usually taken as the unit cell length and is 0.4 nm for BFO. The change in the built-in potential due to the polarization is about 0.57 V according to Eq. (4-1). As the built-in potentials of the ITO/BFO and the SRO/BFO junctions are about 0.3 V and 0.2 V, respectively, the directions of the built-in fields are expected to be switched by the presence of negative polarization charges at the ITO/BFO interface, and positive charges at the SRO/BFO interface (i.e., positive polarization). On the other hand, with the negative polarization, the built-in field is predicted to be enhanced, and the photovoltaic efficiency to be improved.

By using BFO, the new films will be able to absorb light in the visible region. The use of ITO and SRO as the top and the bottom electrodes, respectively, should help to

enhance the photovoltaic efficiency in the BFO thin films. Furthermore, the ferroelectric polarization is expected to enhance the photovoltaic efficiency when it is negative. When it is poled in the opposite direction, the photocurrent is expected to be reduced.

4.3. Experimental methods

Epitaxial BFO thin films were grown by the RF sputter deposition method on the SRO-buffered STO substrates. The SRO layer was chosen as the epitaxial template as well as the bottom electrode. Transparent ITO was used as the top electrode.

The photovoltaic effect was measured by an in-house setup (Fig. 4.2). A xenon light source (Hamamatsu LC8 with L8253 super-quiet xenon lamp) was used for the *J-V* measurement. A hot mirror (SP730, Island Optical) was used to remove the infrared spectrum. Two deep blue band pass filters (BP435) were used to select the incident light wavelength at 435 nm, slightly above the bandgap. The incident intensity was calibrated with a low power detector (Newport 818-UV). The photovoltaic *J-V* measurement was conducted using an electrometer (Keithley 6517A), with the sample connected in the force-voltage-measure-current configuration. The sample point interval was set at 5 seconds. The electrical poling was conducted at an electric field of about 1 MV/cm (twice of the coercive field strength). The poling direction is termed positive if a positive bias voltage is applied to the top electrode with the bottom electrode grounded. The same convention is used for the *J-V* measurement.

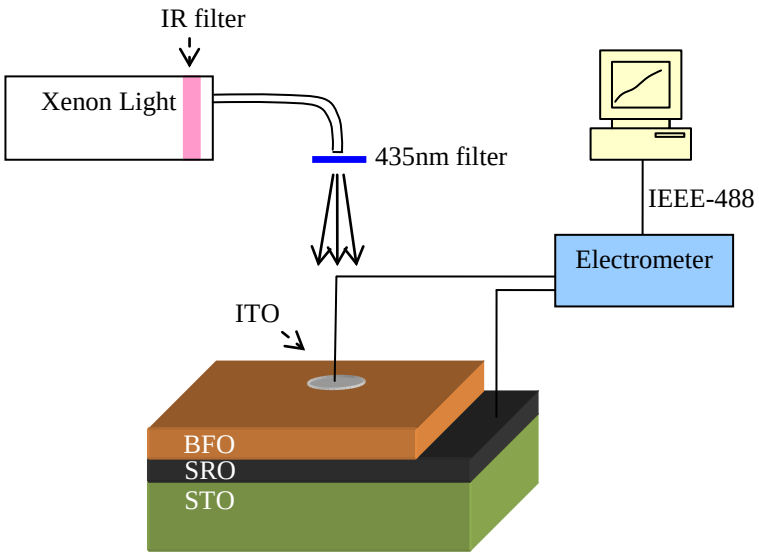

Figure 4.2 Schematic of the photovoltaic measurement setup.

4.4. Results and discussions

4.4.1. Leakage current measurements

The leakage current measurements were carried out to understand the conduction mechanisms of these samples (Fig. 4.3). At low electric fields (below about 20 kV/cm), the conduction is Ohmic in all the tested films. At high fields (more than 100 kV/cm), FN emission dominates. The dominant conduction mechanism at moderate fields is Schottky emission. Although fitting to Poole-Frenkel emission gives a straight line as well, the extracted dielectric constants at optical frequency are too large (the optical dielectric constant at 465 nm is about 9.55 from Fig. 3.18) [107, 127]. The Schottky barrier height (SBH) Φ_{SB} depends very weakly on the effective electron mass in the Richardson's constant. Assuming that the effective electron mass is 5 times of the rest mass [134], Φ_{SB} is estimated to be 0.87 eV for SRO on BFO, and 0.85 to 0.88 eV for ITO on BFO [Fig. 4.3(b)] .

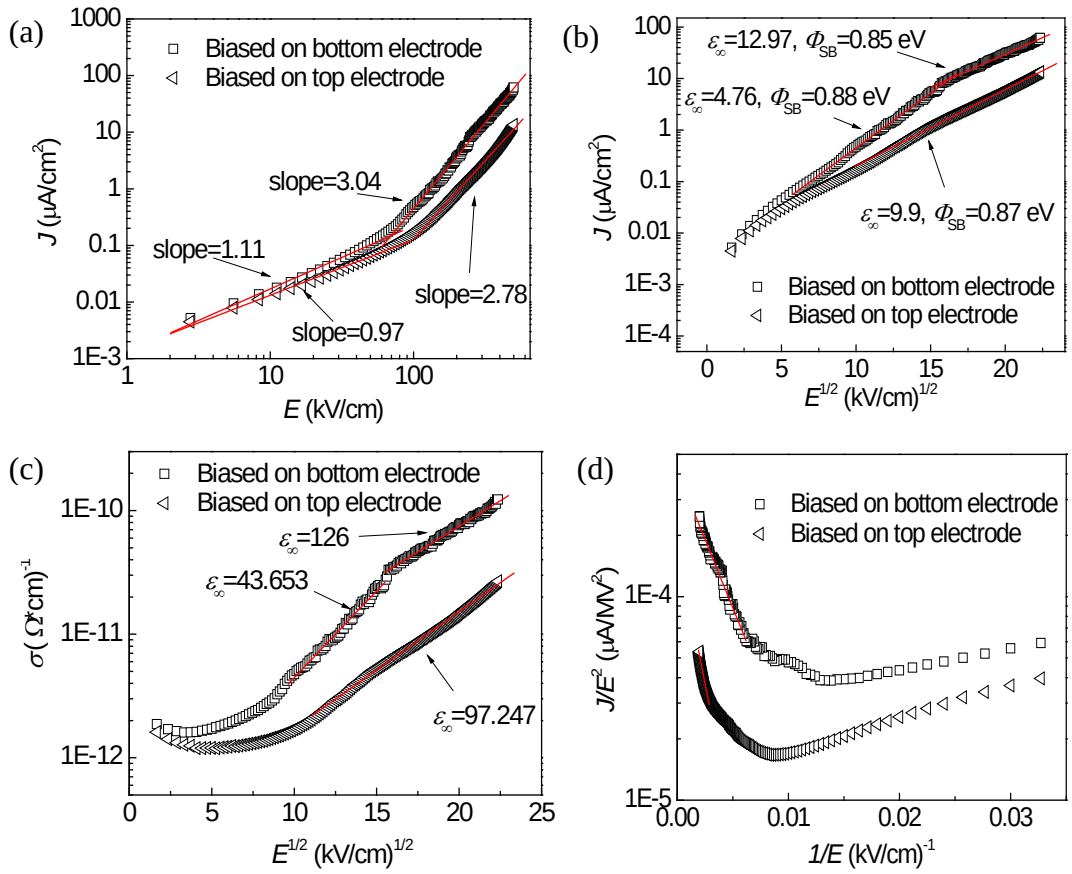

Figure 4.3 Leakage current measurements and analyses for ITO/BFO/SRO/STO(001). All samples were poled first and the current was measured by applying the bias in the same direction as the polarization. (a) Log-log plot shows that the conduction is Ohmic at low field. (b) Schottky emission plot. (c) Poole-Frenkel emission plot . (b) and (c) show that the conduction mechanism is Schottky emission at intermediate field strength with a barrier height between 0.85 and 0.88 eV in both directions. Here $\varepsilon_\infty = n^2$ is the extracted dielectric constant at the optical frequency. (d) Fowler-Nordheim emission plot.

This result shows the current conduction is dominated by the Schottky emission in both directions. Consequently, both interfaces form Schottky barriers, contrary to the hypotheses. This can be explained by the metal-induced gap states (MIGS) model. Clark and Robertson calculated that the SBH of the conductive oxide SRO on BFO is 0.9 eV. This agrees well with the results obtained in this experiment. Although they did not calculate the SBH for ITO, they showed that the SBH is limited to a small range from above 0.7 eV to about 1 eV even when the work function of the electrode

materials differs by more than 1 eV. Consequently, it is reasonable that the ITO forms a Schottky barrier on BFO with a SBH in the range of 0.85 to 0.88 eV here. The much larger SBH compared to the prediction of the Schottky-Mott theory is due to the Fermi-level pinning by the metal-induced gap states [135].

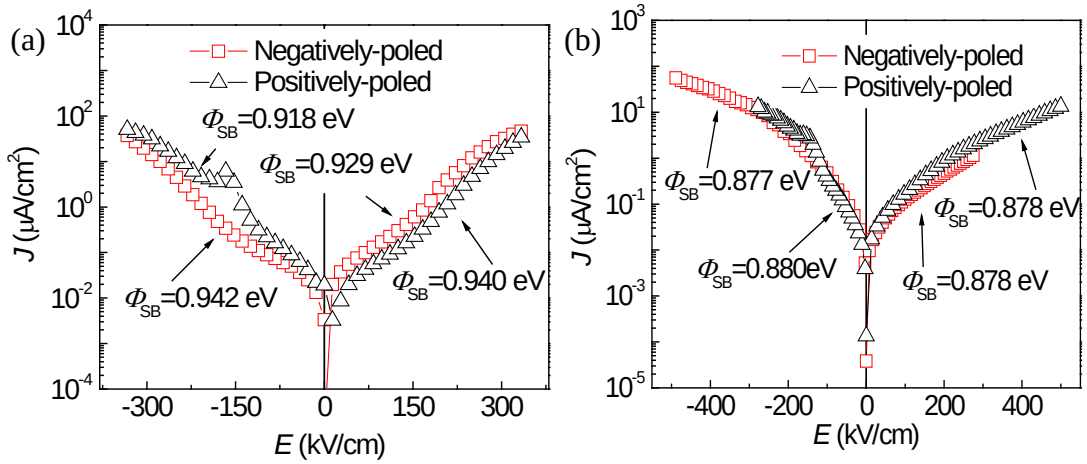

Figure 4.4 Leakage current measurements of ITO/BFO/SRO/STO(001) for two different samples (a) and (b). For each polarization direction, leakage was measured by applying both positive and negative voltages.

The magnitudes of the leakage current in the two directions are not exactly the same. The leakage currents were measured again after poling the samples in different directions. The change in the magnitude of the dark leakage current is typically very small and the diode direction is not always changed after poling (Fig. 4.4). In Fig. 4.4(a), the SBH changes by up to 0.024 eV after poling, while in Fig 4.4(b) the SBH remains practically the same. Contrary to the theories by Pintilie and Alexe [73], the results here show that the SBH is insensitive to the effects of the polarization charges.

4.4.2. Photovoltaic properties with different polarizations

The results of the photovoltaic measurements are plotted in Fig. 4.5. Sustainable and repeatable photocurrents were observed [Fig. 4.5(a)]. Figure 4.5(b) shows that for the positively-poled samples, the photocurrent is negative (i.e., it flows out of the top electrode). In contrast, after the negative poling, the photocurrent direction is reversed. The magnitudes of both the photocurrent and the photovoltage are smaller in the positively-poled samples than in the negatively-poled samples.

Sustainable photocurrent was obtained in the as-deposited BFO thin films as well. A positive photocurrent was obtained, similar to those negatively-poled samples [Fig. 4.5(b)]. Because the leakage measurements show that the two Schottky barriers at the ferroelectric-electrode interfaces are back-to-back and of similar height, this could not be explained by the Schottky junctions. The as-deposited films are self-polarized with the polarization vector pointing towards the film surface (Secs. 3.5.5 and 3.5.6). The similar orientation and magnitude of the ferroelectric polarizations in the as-deposited and the negatively-poled films result in their similar photovoltaic responses. This suggests that the observed photovoltaic effect is related to and may even originates from the ferroelectric depolarization field.

The short-circuit photocurrent density J_{sc} is observed to increase almost linearly with the illumination intensity [Fig. 4.5(c)], while the open-circuit voltage V_{oc} approaches saturation at high illumination intensities [Fig. 4.5(d)]. Both observations agree with the previous studies in bulk samples by Glass and Lines [8]. For the sample of 170 nm in thickness, at the highest illumination intensity measured, V_{oc} is 0.286 V and 0.307 V in the negatively-poled and the as-deposited samples, respectively. It is later found that the photovoltage in fact does not completely saturate at this value but slowly

increases at even higher intensity (Fig. 4.6). The highest V_{oc} obtained is about 0.55 V at an intensity of 260 mW/cm^2.

Compared to other reports on the sandwich-structure BFO thin-film samples, the substantial V_{oc} obtained here is probably a result of the low conductivity of our samples, which is on the order of 10^{-12} Ω^{-1} cm^{-1}, six orders of magnitude smaller than that reported by Basu et al. [83] and also much smaller than that by Choi [86] as well.

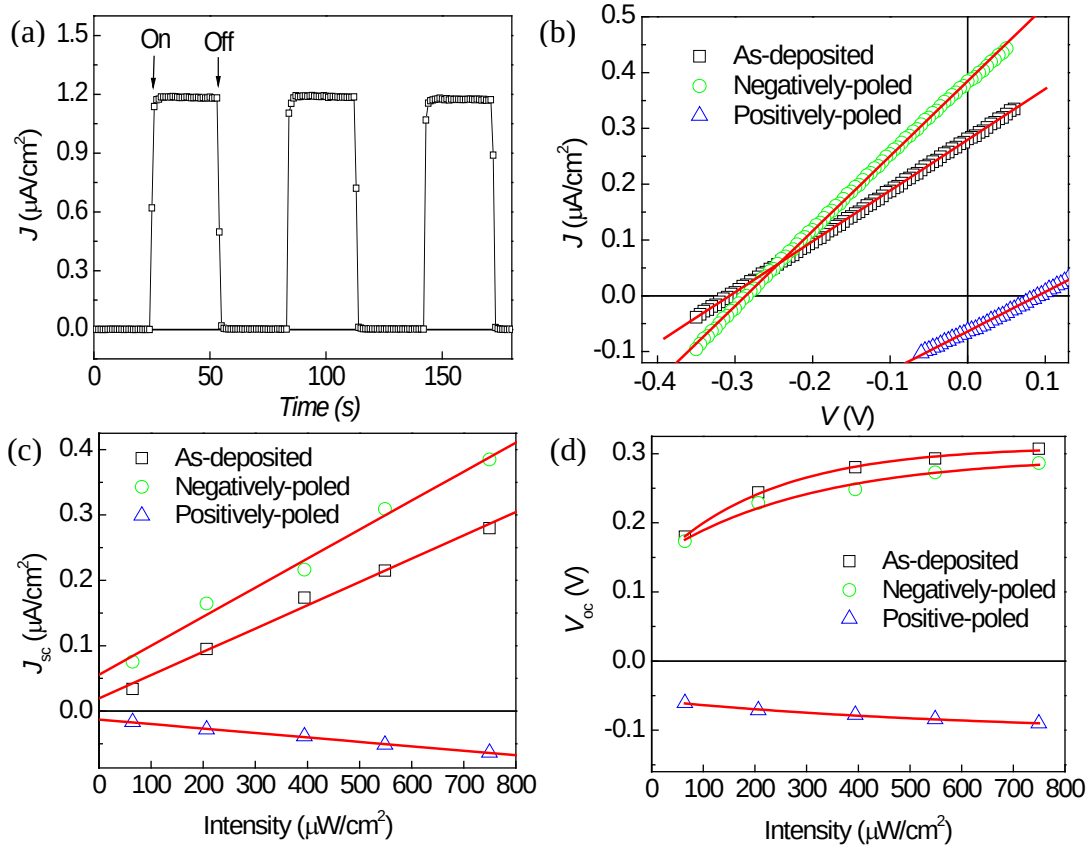

Figure 4.5 Photovoltaic responses for ITO/BFO(170 nm)/SRO/STO(001). (a) Repeatable photocurrents. (b) *J-V* characteristics measured with the incident light of 435 nm at 750 μW/cm^2 for the films before poling, and after positive and negative poling. (c) The open-circuit voltage V_{oc} as a function of the light intensity. (d) The short-circuit photocurrent density J_{sc} as a function of the light intensity.

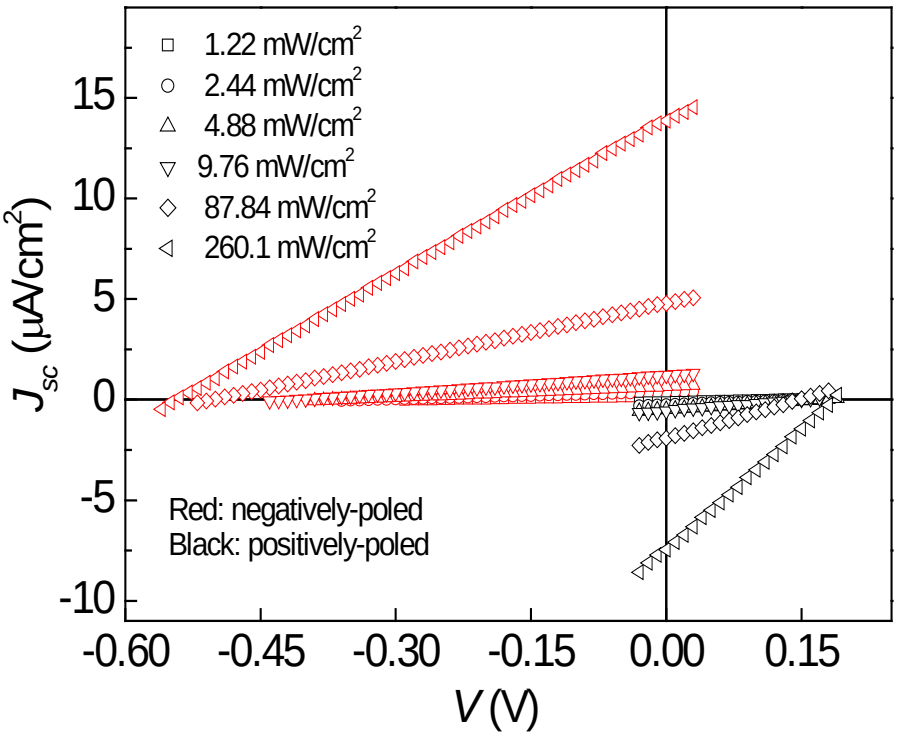

Figure 4.6 Photovoltaic *J-V* curves of ITO/BFO/SRO/STO(001) at higher incident intensities.

The energy band alignment of the device can be modeled as two back-to-back Schottky diodes of similar SBH (Fig. 4.7). The Schottky barriers are insensitive to the ferroelectric polarization charges. As a result, the effects of the Schottky barriers on the photovoltaic properties of the samples are expected to be very small. The back-to-back Schottky junction configuration in Fig. 4.7 shows that the collection of photoexcited electrons will not be efficient. This is one of the limitations to the PV efficiencies in these devices.

The switchable nature of the photocurrent and the photovoltage by poling BFO along the two opposite directions indicates that the ferroelectric polarization has a dominant role in the observed photovoltaic effect. However, the larger magnitude in the negatively-poled films indicates that there is an internal bias field E_{bi} pointing towards

the bottom electrode, as illustrated in Fig. 4.7. Such a bias field might exist in the bulk of the film due to a nonuniform distribution of oxygen vacancies or other defects.

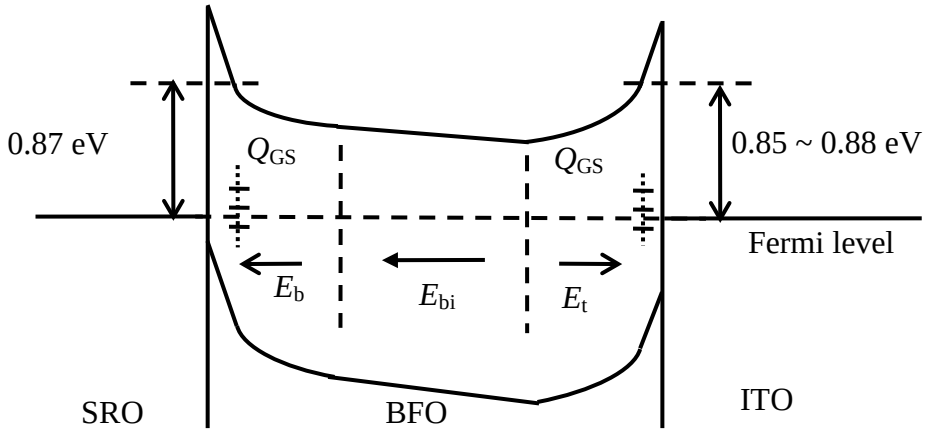

Figure 4.7 Schematic of energy band alignment for the ITO/BFO/SRO capacitor according to the fixed separation model of MIGS (not to scale). E_b and E_t are the built-in fields at the bottom and top electrode interfaces, respectively. E_{bi} is the unswitchable built-in field in the film bulk possibly due to nonuniform distribution of defects. Q_{GS} denotes the gap state charges.

4.4.3. Mechanism of the photovoltaic effects

The contribution from the ferroelectric polarization can be estimated by separating the overall photovoltaic response into two independent components [136]: one from the ferroelectric polarization, and the other from the internal bias field. The switchable open-circuit voltage component due to the switchable polarization $V_{OC,p}$, and the unswitchable component due to the unswitchable internal bias field $V_{OC,bi}$ can be estimated by

$$\left|V_{OC,p}\right| = \frac{1}{2}(V_+ - V_-), \qquad 4\text{-}3$$

$$\left|V_{OC,bi}\right| = \frac{1}{2}(V_+ + V_-), \qquad 4\text{-}4$$

where V_+ and V_- are the open-circuit voltage after positive poling and negative poling, respectively. The short-circuit photocurrent can be treated in the same way. The results for the open-circuit voltage and the short-circuit current are plotted in Figs. 4.8(a) and 4.8(b), respectively. The contribution from the switchable polarization is much larger than that from the unswitchable internal field. Notably, the contribution from the switchable polarization to the photovoltage is about twice of that from the unswitchable internal field.

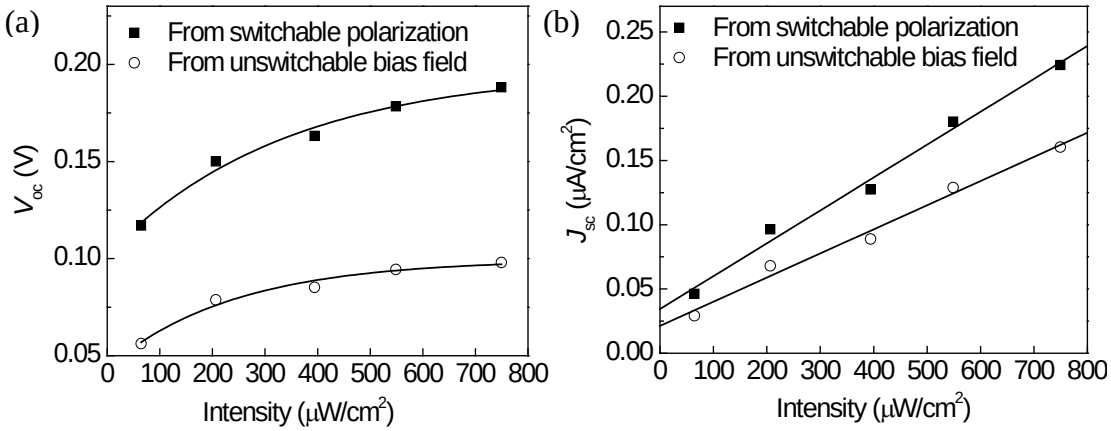

Figure 4.8 Separated contributions from the switchable polarization and unswitchable internal bias field in the 170-nm BFO film. (a) Open-circuit voltage and (b) short-circuit current density.

In some devices the PV effects can be almost completely switched by poling in different directions. The effect of the polarization on the PV effect can be best visualized by measuring the J_{sc} and V_{oc} after poling the films to different voltages. The J_{sc} and V_{oc} are plotted against the poling voltages in Fig. 4.9, and they form hysteresis loops similar to the *P-E* hysteresis loop. This shows the deciding effect of the ferroelectric polarization on the PV effect in the BFO thin-film samples.

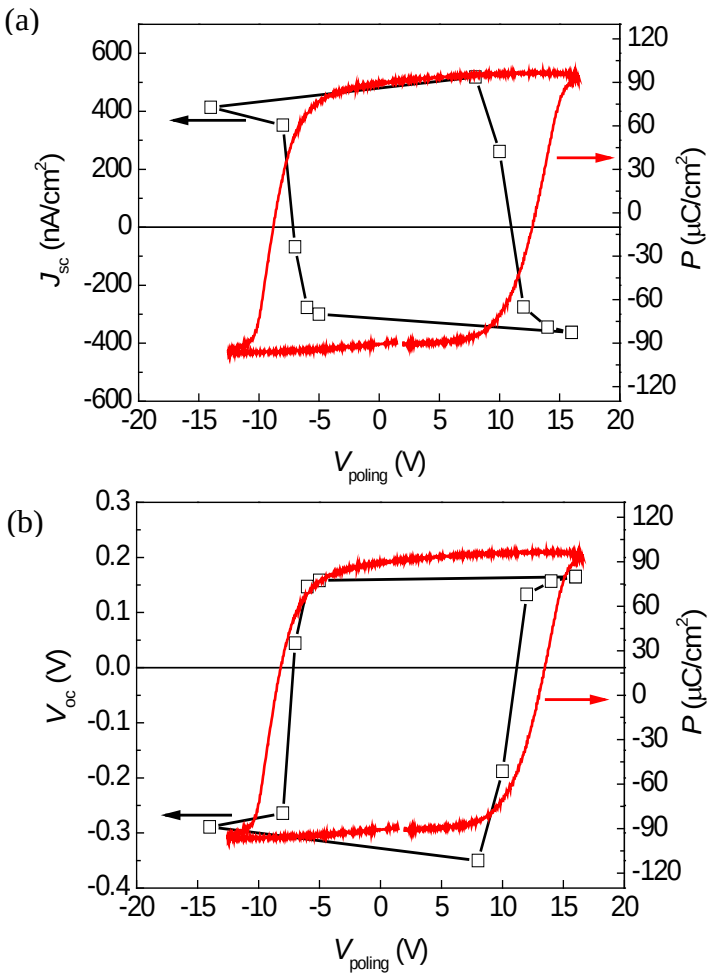

Figure 4.9 (a) J_{sc} and (b) V_{oc} measured at different poling voltages (black) to form hysteresis loops. *P-E* hysteresis loops (red) are superimposed to illustrate the direct correlation of the ferroelectric polarization with J_{sc} and V_{oc}.

The origin of the BPVE has been studied by many papers. Chen observed that the photocurrent was opposite the polarization direction, and postulated that this was caused by an internal electric field anti-parallel to the polarization [75]. The same dependence of the photocurrent on the polarization direction was observed in our experiments. Although Chen did not identify the origin of the internal field in his original work, it might be interpreted as the depolarization field in thin films [68], which results from the incomplete screening of the ferroelectric polarization charges [69].

It has been shown that in bulk ferroelectrics the depolarization field is negligibly small and thus has little effect on the PV processes [78]. As a result, other theories, which do not make use of an internal electric field, have been proposed to explain the PV effect in ferroelectrics. Glass et al. proposed that the photocurrent results from charge scattering by local asymmetric potentials [8]. Sturman and Fridkin also explained the BPVE as the result of the asymmetry of elementary processes, such as photoexcitation and scattering, in a noncentrosymmetric medium [57]. Tonooka and Uchino proposed that the BPVE results from a DC field created by the optical rectification effect [61]. But this second-order effect is in general very weak and requires high intensity light sources such as lasers, while in this experiment PV effect is observed even with light intensity below one mW/cm^2. The dark leakage current measurements for some of our samples show a small diode-like effect (Fig. 4.4), but this effect is not substantially reproduced in all the samples. The change in the magnitude of dark leakage current is typically very small and the diode direction is not always changed when the sample is poled in different directions (Fig. 4.4), while the photocurrent direction is always opposite to the polarization direction (Fig. 4.9). This is in contrast to the results of Ref. [86], where the photocurrent direction follows the diode direction. Consequently, the observed polarization-dependent photovoltaic effect in this study could not be explained by the effect of a polarization-dependent diode.

The photocurrent observed in this experiment is anti-parallel to the ferroelectric polarization vector. However, this is not always the case in the literature [132]. Photocurrents perpendicular to the polarization direction have also been observed in bulk ferroelectric materials [58, 137]. In fact, studies in ferroelectric single crystals have shown that the photocurrent depends on the incident light polarization and the

material symmetry (point group) [56, 57, 86]. This dependence is described by a photovoltaic tensor of rank three in the theory of the BPVE [138]. In this study, The measured photocurrent is along the same direction as the depolarization field.

It is rather surprising and counter-intuitive that the ferroelectric polarization changes the direction of the photocurrent but has so little effect on the Schottky barrier height at the ferroelectric-electrode interface and the dark leakage behavior in the ITO/BFO/SRO system. This shows that the ferroelectric polarization can affect the PV processes in more ways than one. In this case, the depolarization field alters the band bending in the bulk of the ferroelectric thin films and drives the carrier separation and transportation. The maximum open-circuit voltage obtained in this experiment is 0.55 V, corresponding to 24.5 kV/cm. By a simple application of the Poisson's equation, one can show that it only takes about 0.15 $\mu C/cm^2$ of polarization charge to build up a depolarization field of this magnitude. This is much smaller than the remanent polarization of the BFO films. It seems very plausible that the depolarization field due to incomplete screening of the ferroelectric polarization is the cause of the PV effect observed here. The Schottky junctions do not play an important role here and are insensitive to the polarization charges because of the strong Fermi-level pinning. However, the photocurrent might also have some contribution from the BPVE. Both mechanism can generate photocurrents along the polarization direction, and in both cases the current will reverse the direction with the switching of the polarization. The experimental configuration here does not allow the separate measurements of the photocurrent components from the BPVE and that from the depolarization field. As a result, the contributions to the PV effect from these two mechanism cannot be unambiguously separated in this experiment.

4.5. Optimization of the electrodes

The highest PV efficiency of the BFO films obtained here is 0.0052%. The low efficiency is partly because of the ineffective charge collections at the Schottky barriers. In an attempt to improve the device efficiency, other electrode materials were considered. For the bottom electrode, there is an additional requirement of a small lattice mismatch with BFO and STO to act as an epitaxial growth template. This limits the possible candidates to only a few conducting oxides. As the ITO forms a Schottky barrier on BFO, ideally the bottom electrode should have a small work function to form a nonrectifying barrier.

One possible material is the Nb-doped STO (Nb:STO), which has a work function of 4.3 eV [139]. Epitaxial BFO thin films were prepared on the Nb:STO(001) substrates. However, the hysteresis *P*-*E* loops in these samples were not saturated, even at an electric field of more than 1000 kV/cm [Fig. 4.10(a)]. This indicates that the ferroelectric polarization in these samples is probably pinned in a preferable orientation. Piezoelectric responses were measured with an LSV in an as-deposited sample [Fig. 4.10(b)]. The sample is negatively self-polarized. These results suggest that the internal fields of both Schottky junctions point to the bottom electrode, and they enforce and pin the negative self-polarization.

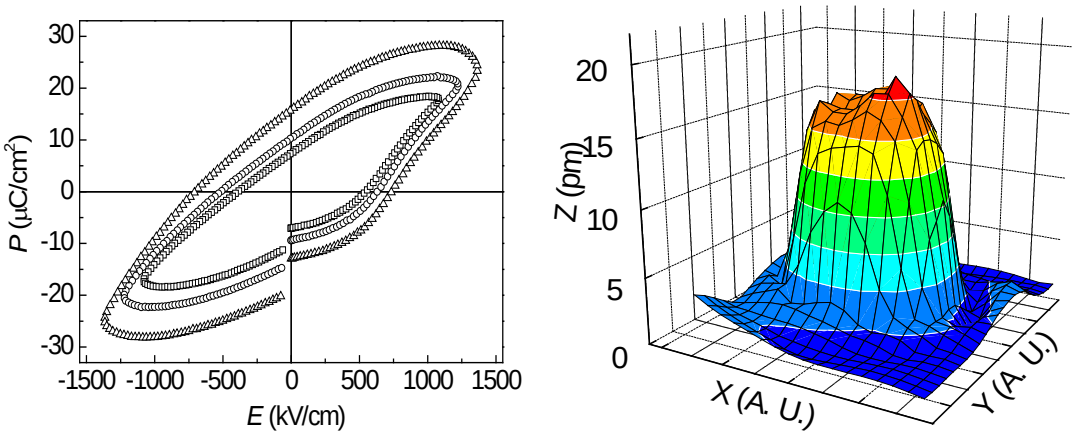

Figure 4.10 (a) Hysteresis *P-E* loops and (b) piezoelectric displacements of ITO/BFO/Nb:STO(001).

The photocurrent in the ITO/BFO/Nb:STO samples is practically zero (Fig. 4.11). The transient component of the current in Fig. 4.11 is from the pyroelectric effect. As discussed earlier, the photocurrent from the depolarization field is positive, while the photocurrent from both Schottky barriers are negative. They cancel each other and result in a negligibly small photocurrent. The PV effect is insensitive to poling. This is probably because the polarization is pinned and cannot be switched (Fig. 4.10).

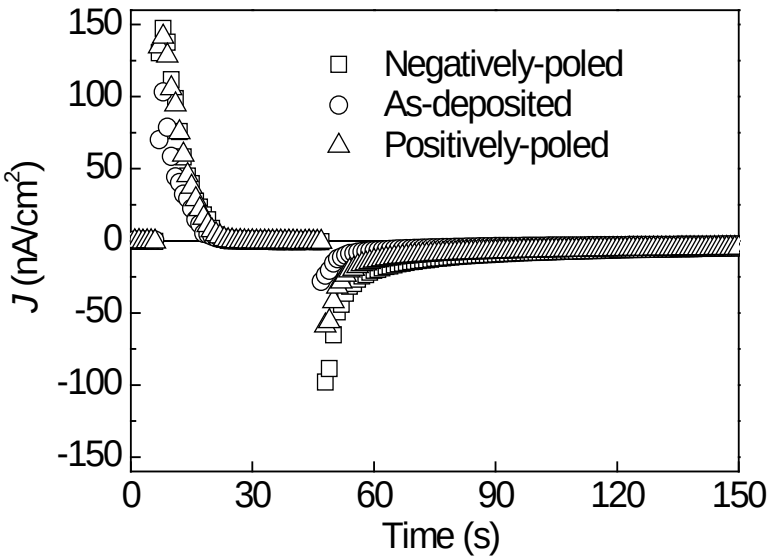

Figure 4.11 Short-circuit current density vs. time in ITO/BFO/Nb:STO(001) with different polarizations.

Although these ITO/BFO/Nb:STO samples have not been successfully poled to different directions, a different growth method might be able to produce samples that are positively self-poled. In that case, both photocurrents can be aligned in the same direction and add up to a larger current.

Another bottom electrode material $LaNiO_3$ was also tested. It has a work function of 4.5 eV [140], smaller than SRO by 0.3 eV. The V_{oc} and J_{sc} are smaller than those obtained in the BFO films grown on SRO bottom electrode (Fig. 4.12). As the lattice mismatch of $LaNiO_3$ with BFO is about -2.83%, much larger than SRO, the drop in the performance could be due to the larger amount of defects present.

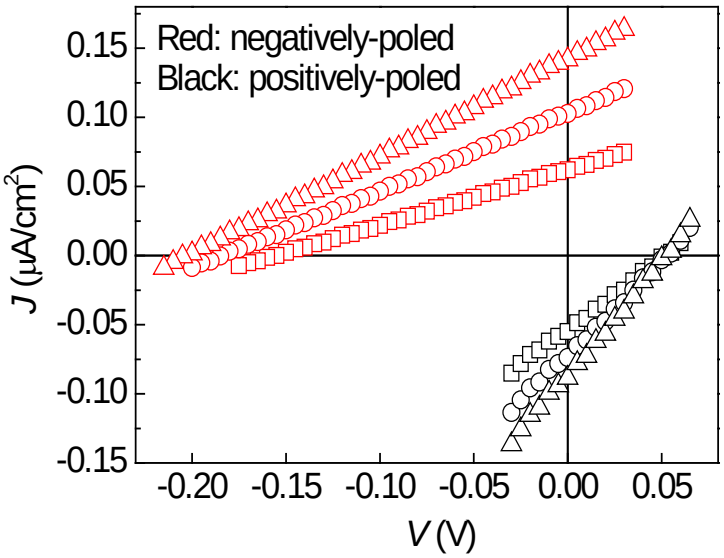

Figure. 4.12 Photovoltaic *J-V* curves of ITO/BFO/$LaNiO_3$/STO(001) at different intensities, (□) 2.3 mW/cm^2, (○) 4.2 mW/cm^2, and (△) 6.3 mW/cm^2.

The top electrode has to be transparent. Apart from ITO, available materials include fluorine-doped tin oxide (FTO) and Al-doped ZnO. However, FTO has a similar work function as ITO at 4.4 eV [141], while Al-doped ZnO has a slightly higher work

function at 4.6 to 4.7 eV [142]. As a result, these are expected to result in similar performances as ITO on BFO and are not tested.

Recently Zang and his coworkers investigated the PV performance of polycrystalline BFO grown on Pt bottome electrode [143]. They found that both J_{sc} and V_{oc} were enhanced with graphene as the top electrode over those with the ITO top electrode. The performance is further enhanced by HNO_3 treatment of the graphene, which reduces its work function by 0.13 V. However, the highest efficiency they obtained is only 2.5×10^{-3}%. One of the reasons for such a low efficiency could be the high density of defects commonly found in polycrystalline BFO films. Nevertheless, their results demonstrated that the PV effect can be enhanced by the proper selection of the electrode materials to improve charge collections.

4.6. Conclusion

In summary, appreciable photovoltaic response in the visible wavelength has been demonstrated with epitaxial multiferroic BFO thin films, which is prepared by scalable sputter deposition process. The as-deposited BFO films are completely self-polarized and produce a large open-circuit photovoltage up to 0.55 V (24.6 kV/cm). However the back-to-back Schottky junctions formed at the two ferroelectric-electrode interfaces in ITO/BFO/SRO impede the efficient collection of charge carriers. Higher photovoltaic output could be obtained with optimized electrode materials that provide selective charge collections for electrons and holes.

Ferroelectric polarization has a dominant effect on the PV properties of the device. A large portion, in some cases almost all, of the photovoltage and the photocurrent is switchable in response to the switching of the ferroelectric polarization, with the

direction of the photocurrent opposite to that of the polarization vector. In contrast, the Schottky barriers are found to be insensitive to the ferroelectric polarization due to Fermi-level pinning. The PV effect here can be caused by the depolarization field or the BPVE. These two mechanisms, however, cannot be separated in this experiment. This is because the photocurrents from both mechanisms are aligned in the out-of-plane direction, and they both will switch directions with the ferroelectric polarization. A new experiment must be designed to resolve this question and this will be the topic of the next chapter.

Chapter 5. Evidence for bulk photovoltaic effect in ferroelectric thin films

5.1. Introduction

In the last chapter, the PV effect in the sandwich-structure BFO thin films illuminated by the visible light is investigated. The photocurrent is found to be switchable with the direction of the ferroelectric polarization. The Schottky junctions at the two BFO-electrode interfaces are found to be back-to-back Schottky diodes and are almost symmetric due to the Fermi-level pinning effect. As a result, Schottky junctions do not significantly affect the observed PV results. However, switchable photocurrents strongly affected by the interfaces with electrodes was observed by Choi et al. in a BFO bulk single crystal [86]. It was also reported that the photovoltaic current in some BFO thin films cannot be switched at all and was entirely attributed to the interface depletion layer between the BFO and electrode [144]. Yang et al. demonstrated photovoltaic effect in BFO films that arises from domain walls [63]. Some results in the reports from Choi et al. [86] and Kundys et al. [145] showed an angular dependence of the photocurrent on the light polarization direction, although this has never been interpreted as the result of the BPVE. It should be highlighted that in all the studies above on BFO and PLZT, only the photocurrent in the ferroelectric polarization direction has been studied, which makes it difficult to separate the effects of the interfacial barriers and the depolarization field from the BPVE. As a result, none of the earlier studies can give insights to if and how the BPVE contributes to the photovoltaic effect in ferroelectric thin films. In order to answer these questions, it is necessary to investigate the photocurrent in the plane perpendicular to the ferroelectric polarization (i.e., perpendicular to the depolarization field) with

symmetric electrodes to clearly separate it from the significant effects of the interfacial energy barriers and the depolarization field.

BFO has the crystallographic point group of 3m and belongs to the trigonal system. Its photovoltaic tensor has a nonzero component of G_{22}. Consequently, a photocurrent should exist in the direction perpendicular to the ferroelectric polarization [55]. In order to investigate the photovoltaic response in the direction perpendicular to the polarization direction, epitaxial BFO thin films were prepared directly on the STO(111) substrates, and the photocurrent were measured in the direction perpendicular to the polarization direction under a linearly polarized light. The BFO films grown on the STO(111) substrates are found to be rhombohedral (Sec. 3.5.1 and in particular Fig. 3.12). By investigating the angular dependence of this photocurrent on the incident light polarization, for the first time, it is shown that the BPVE exists in epitaxial BFO film as thin as 40 nm and the photovoltaic tensor coefficient β_{22} of BFO is about five orders of magnitude larger than other typical ferroelectric materials at visible light wavelength.

5.2. BPVE in epitaxial $BiFeO_3$ thin films

5.2.1. Experimental methods

As discussed before, BFO belongs to the rhombohedral group of R3m and can be indexed in the trigonal or the hexagonal system. In this study the hexagonal system is adopted [121]. The relationship between the trigonal, the rhombohedral, the pseudo-cubic unit cells, and the Cartesian coordinates is illustrated in Fig. 5.1(a).

The coordinate transformation between the hexagonal and the pseudo-cubic cells is given below. The relationship of the basis vectors between the hexagonal lattice frame and the pseudo-cubic lattice frame is

$$\vec{a}_{i,\mathrm{h}} = \alpha_{ij}\vec{a}_{j,\mathrm{pc}}, \tag{5-1}$$

$$\vec{a}_{i,\mathrm{pc}} = \alpha_{ij}^{-1}\vec{a}_{j,\mathrm{h}}, \tag{5-2}$$

with the transformation matrices expressed as

$$\boldsymbol{\alpha} = \begin{pmatrix} 1 & 1 & 0 \\ -1 & 0 & 1 \\ 2 & -2 & 2 \end{pmatrix}, \tag{5-3}$$

$$\boldsymbol{\alpha}^{-1} = \frac{1}{3}\begin{pmatrix} 1 & -1 & \frac{1}{2} \\ 2 & 1 & -\frac{1}{2} \\ 1 & 2 & \frac{1}{2} \end{pmatrix}. \tag{5-4}$$

It can be shown that the lattice vector $[110]_{\mathrm{pc}}$ is equivalent to the vector $[100]_{\mathrm{h}}$ (the x axis):

$$\vec{R}_{\mathrm{pc}} = [100]_{\mathrm{h}}\begin{pmatrix} 1 & 1 & 0 \\ -1 & 0 & 1 \\ 2 & -2 & 2 \end{pmatrix} = [110]_{\mathrm{pc}}. \tag{5-5}$$

The small distortion of the pseudo-cubic structure can be ignored. The lattice direction $[001]_{\mathrm{pc}}$ is perpendicular to $[110]_{\mathrm{pc}}$ because

$$[110]_{\mathrm{pc}} \cdot [001]_{\mathrm{pc}} = 0. \tag{5-6}$$

Therefore the projection of the lattice $[001]_{pc}$ in the $(001)_h$ plane is the y axis of the hexagonal lattice.

In order to calculate the BPVE tensor properties, one has to work in the Cartesian frame, rather than the crystallographic hexagonal frame. The z axis of the Cartesian coordinates coincides with the *c* axis of the hexagonal cell and is in the same direction as the ferroelectric polarization. The samples from our RF magnetron sputtering are self-polarized with the polarization direction pointing out of the film surface [146]. The direction of the z axis is the same as the direction of the polarization vector. The x axis of the Cartesian coordinates coincides with the crystallographic axis *a* ($[100]_h$) in the hexagonal cell [147]. The y axis is perpendicular to both the z and the x axes, forming a right-hand coordinate system, as shown in Fig. 5.1(a). Au in-plane electrodes with a gap of 0.14 mm were patterned by a standard photolithography process [Fig. 5.1(b)].

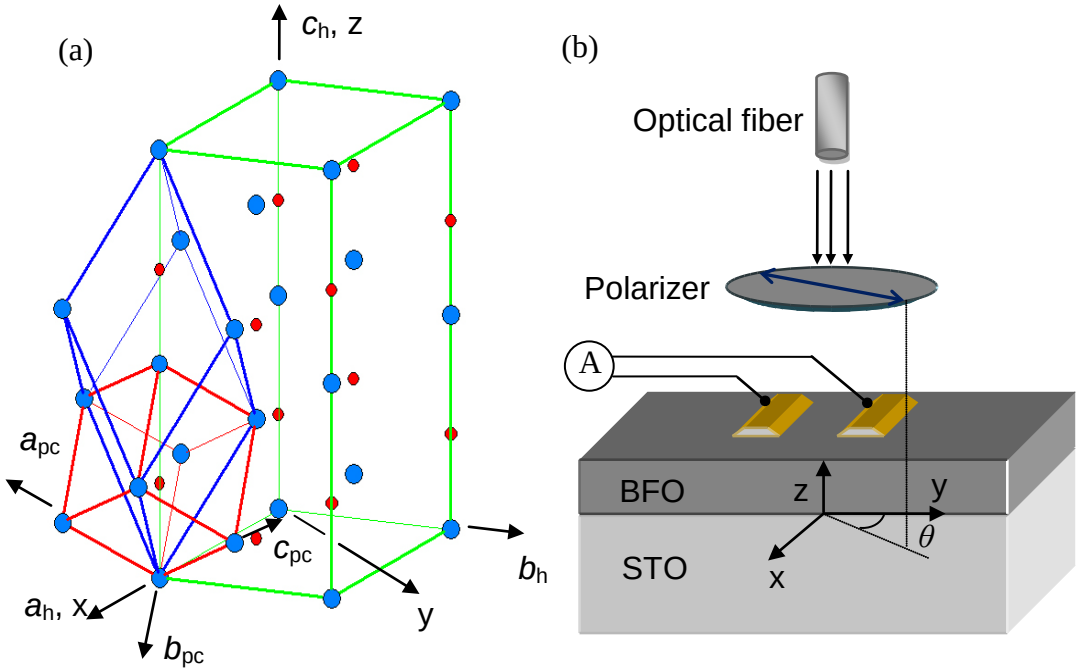

Figure 5.1 (a) Relationship between the conventional hexagonal (green), the rhombohedral (blue), and the pseudo-cubic (red) unit cells for BFO and the Cartesian coordinates. The large blue spheres are Bi atoms and the small red spheres are Fe atoms. Oxygen atoms are omitted for clarity. (b) Schematic illustration of the epitaxial BFO thin film with in-plane electrodes and polarization along thickness direction under polarized light. The angle between the polarizer transmission axis and the y axis is θ.

The short-circuit photocurrent was measured with an electrometer (Keithley 6517A) at an incident light wavelength of 435 nm [146]. The light propagated perpendicular to the sample surface, and the incident intensity was 20 mW/cm^2. A Glan-Taylor polarizer was used to rotate the light polarization in the $(001)_h$ plane at an interval of 45 degrees. At each polarizer angle the short-circuit photocurrent was measured. The steady-state readings were used for the calculations.

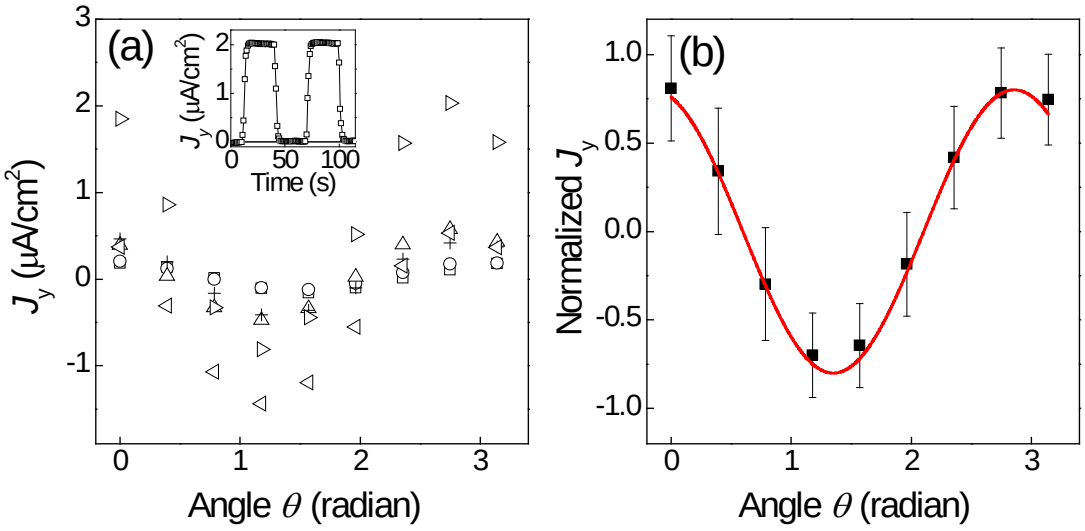

Figure 5.2 Short-circuit photocurrent density J_y. (a) J_y of samples with different thicknesses, (□) 446 nm, (○) 335 nm, (△) 223 nm, (+) 135 nm, (◁) 80 nm, (▷) 40 nm. Inset shows the time dependence of $J_{y.}$ (b) Normalized J_y at different polarizer angles. The error bar is one standard deviation of the readings from different samples.

The in-plane orientation of the BFO films was determined by the XRD azimuthal scans. The (200) planes of the substrate and the $(200)_{pc}$ of BFO films were found to coincide with each other. This was used to determine the y axis of the Cartesian coordinates. The projection of the $[001]_{pc}$ lattice vector in the $(001)_h$ plane is the y axis of the hexagonal lattice.

5.2.2. Tensorial photocurrent in $BiFeO_3$ thin films

Repeatable and continuous photocurrents were obtained when the samples were illuminated [Fig. 5.2(a) inset]. The short-circuit current densities at different polarizer angles for the samples with six different thicknesses are plotted in Fig. 5.2(a). Since the magnitude of the photocurrent varies with the sample thickness, the results for individual samples are normalized. The current density is also slightly affected by the minor variation in light intensity when the polarizer is changed to a different angle. To minimize the effect of these minor variations in our analysis, the average of the

normalized photocurrent densities for all the samples is calculated for each polarizer angle. The result is fitted very well to a cosine function, as shown in Fig. 5.2(b). The fitting function is

$$J_y = 0.801\cos[2.087(\theta + 0.154)]. \quad 5\text{-}7$$

Equation (5-7) shows an offset of about 8.8° from the origin. This is mainly caused by the misalignment between the crystal axes, the in-plane electrodes, and the incident light polarization direction.

It should be emphasized that the photocurrent measured here is perpendicular to the ferroelectric polarization vector. Therefore, unlike the works in Refs. [69, 86, 146], our results cannot be explained by the depolarization field. The direction of the photocurrent and the low incident intensity employed here rule out the second-order optical effects [61] as well. The effect of the asymmetric energy barriers [73] is also excluded by the use of the symmetric in-plane electrodes. The theory of the electrostatic potential at domain walls [63] cannot explain the angular dependence of the photocurrent here. This angular dependence can be described in the framework of the BPVE theory, where the photocurrent is produced as a consequence of the asymmetric microscopic processes [57]. According to this theory, the dependence of the photocurrent on the incident light polarization can be expressed by a bulk photovoltaic tensor. As BFO has high absorption coefficient at the incident wavelength [146], it is necessary here to modify the formulae by explicitly expressing the light intensity as a function of the film thickness.

The incident light propagates along the z-axis can be expressed as

$$\begin{aligned}\vec{E} &= |E|\left[\hat{e}_{\mathrm{x}}\sin(\theta)\exp i(k_{\mathrm{o}}z-\omega t)+\hat{e}_{\mathrm{y}}\cos(\theta)\exp i(k_{\mathrm{o}}z-\omega t)\right] \\ &= |E|\left[\hat{e}_{\mathrm{x}}e_1+\hat{e}_{\mathrm{y}}e_2\right].\end{aligned} \tag{5-8}$$

For a sample with a weak absorption coefficient, uniform absorptions can be assumed. The resultant photocurrent density can be calculated as

$$\begin{aligned}\vec{J} &= I_{\mathrm{L}}\begin{bmatrix} 0 & 0 & 0 & 0 & \beta_{15} & -\beta_{22} \\ -\beta_{22} & \beta_{22} & 0 & \beta_{15} & 0 & 0 \\ \beta_{31} & \beta_{31} & \beta_{33} & 0 & 0 & 0 \end{bmatrix}\begin{bmatrix} e_1^2 \\ e_2^2 \\ 0 \\ 0 \\ 0 \\ e_1e_2^* \end{bmatrix} = I_{\mathrm{L}}\begin{bmatrix} -\beta_{22}e_1e_2^* \\ -\beta_{22}e_1^2+\beta_{22}e_2^2 \\ \beta_{31}e_1^2+\beta_{31}e_2^2 \end{bmatrix} \\ &= I_{\mathrm{L}}\alpha\begin{bmatrix} -G_{22}\sin\theta\cos\theta \\ -G_{22}\sin^2\theta+G_{22}\cos^2\theta \\ G_{31} \end{bmatrix}.\end{aligned} \tag{5-9}$$

The components of the photocurrent density along different axes are

$$J_{\mathrm{x}} = -I_{\mathrm{L}}\alpha G_{22}\sin\theta\cos\theta = -\frac{1}{2}I_{\mathrm{L}}\alpha G_{22}\sin 2\theta, \tag{5-10}$$

$$J_{\mathrm{y}} = I_{\mathrm{L}}\alpha G_{22}\left(-\cos^2\theta+\sin^2\theta\right) = I_{\mathrm{L}}\alpha G_{22}\cos 2\theta, \tag{5-11}$$

$$J_{\mathrm{z}} = I_{\mathrm{L}}\alpha G_{31}. \tag{5-12}$$

In a medium with strong absorption, however, the photocurrent is mainly generated near the illuminated surface and becomes a function of the penetration depth. As a result, the above equations need to be modified. Next, we consider explicitly the nonuniform absorption of light in thin films. For clarity, we first derive J_{y} when the light polarization coincides with the y axis (θ = 0). We denote the parameters as follows:

s: length of electrode

l: electrode gap

δ: film thickness

$I_L(x)$: incident intensity at the depth of *x*

The current density by absorption in a differential volume of d*x*d*y*d*z*

$$J_y = \alpha G_{22} I_L = \alpha G_{22} I_L(0)\exp(-\alpha z). \quad 5\text{-}13$$

The current through a differential area dzdx is

$$dI_y = J_y dzdx = \alpha G_{22} I_L(0)\exp(-\alpha z)\, dzdx. \quad 5\text{-}14$$

The total current through the face $s\times\delta$ is

$$I_y = \int_{0,0}^{z=\delta,x=s} J_y dzdx = \alpha G_{22} I_L(0) \int_{0,0}^{z=\delta,x=s} e^{-\alpha z} dzdx = sG_{22} I_L(0)[1-\exp(-\alpha\delta)]. \quad 5\text{-}15$$

The current density is

$$J_{y,\theta=0} = \frac{I_y}{s\delta} = G_{22} I(0)\frac{[1-\exp(-\alpha\delta)]}{\delta}, \quad 5\text{-}16$$

where

$$G_{22} = \frac{\beta_{22}}{\alpha}. \quad 5\text{-}17$$

Similar expressions can be derived for the photocurrent in other directions. The current density with angular dependence along the y axis is

$$J_y = I_L(0) G_{22} \frac{1-\exp(-\alpha\delta)}{\delta} \cos 2\theta = I_L(0) \beta_{22} \frac{1-\exp(-\alpha\delta)}{\alpha\delta} \cos 2\theta, \quad 5\text{-}18$$

where $T(0)$, G, β, α, and δ are the incident intensity, Glass constant, tensor coefficient, absorption coefficient and film thickness, respectively. Equation (5-18) describes the current along the y direction as a cosine function of 2θ, in which θ is the angle between the light polarization and the y axis. The experimental results [Fig. 5.2 and Eq. (5-7)] agree well with the theoretical calculation of Eq. (5-18).

The photocurrent density increases with the decrease in the film thickness, as shown in Fig. 5.3. By fitting our results to Eq. (5-18), we can obtain the values of α, G_{22}, and β_{22}. The Glass coefficient G_{22} is 4.48×10^{-10} cm/V, comparable to other ferroelectric materials such as LNO and BTO [57]. The absorption coefficient α is found to be $2.5\text{x}10^{5}$ cm^{-1}. This strong absorption is believed to be a consequence of the direct bandgap of BFO. The tensor coefficient β_{22} is around $1.1\text{x}10^{-4}$ V^{-1}, which is about five orders of magnitude larger than the typical values of both $LiNbO_3$:Fe and $LiTaO_3$ [57], which belong to the same 3m point group as BFO, and is six orders of magnitude larger than that of PLZT [148]. The enhancement of the β_{22} in BFO can be attributed to the large absorption coefficient α. Although a small internal resistance could also enhance the photocurrent output, this is ruled out here as the samples display a high resistivity of about 10^{12} cm Ω at low fields. It is interesting that in Ref. [148] the PV effect of PLZT is measured with a UV light of 365 nm, above the bandgap of the material. According to the literature, the absorption coefficient of PLZT at this wavelength is $2\text{x}10^{4}$ cm^{-1} [68], only one order of magnitude smaller than that of BFO. The effect of the BPVE in BFO may be much stronger due to its larger polarization (i.e., stronger asymmetry). However it is also possible that the BPVE coefficient in PLZT was underestimated in Ref. [148] .The photocurrent is measured in a PLZT

sample of the sandwich structure. The polarization is in the thickness direction and so is the measured photocurrent. The photocurrents caused by the BPVE, the interfacial Schottky junctions, and the depolarization field can compete with each other. The total photocurrent can be reduced if their directions are opposite to each other.

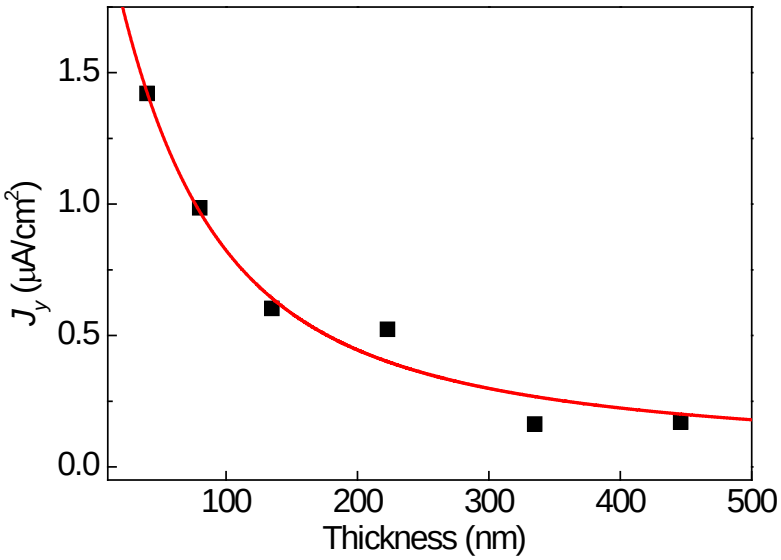

Figure 5.3 BPVE current density J_y for samples with different thicknesses. Solid line shows the fitting curve to Eq. (5-18).

From the theoretical analysis, it is difficult to conclusively determine the direction of the BPVE photocurrent along the z axis because of the unknown sign of G_{31}. However, our experimental PV results in epitaxial BFO films on SRO-buffered STO(001) and STO (111) substrates with ITO top electrodes provided the clues about this issue. The polarization vector in these films pointed to the top electrode [146]. The experimentally observed photocurrent flew from top electrode to the bottom electrode inside the films, e.g., in the direction of the depolarization field. What is interesting is that the current density is two orders of magnitude larger in the (001)-oriented film than in the (111)-oriented film (Fig. 5.4). This can be explained if the BPVE current is opposite to the depolarization field. From experimental data of other

bulk ferroelectric materials it is known that the magnitude of BPVE tensor coefficients β_{31} and β_{33} are normally one order of magnitude larger than β_{22} [57]. Hence here they can be estimated to be on the order of $1x10^{-3}$ V^{-1}. Thus the estimated magnitude of the BPVE photocurrent density along the z axis is on the order of a few $\mu A/cm^2$ at the illumination intensity of 5.8 mW/cm^2, which is comparable with the magnitude of the photocurrent observed in the (001)-oriented films. The two currents originating from the depolarization field and the BPVE have similar magnitudes but opposite directions, and therefore only a very small current can be detected in the case of the BFO(111) films. However, as the polarization vector of BFO(001) forms an angle of 54.7° with the surface normal, the BPVE current collected at the $(001)_{pc}$ face is reduced by about half, resulting in a much larger photocurrent in the direction opposite to the polarization (i.e., aligned with the depolarization field).

Therefore, I believe that the BPVE current in BFO along the thickness direction should flow in the same direction as the ferroelectric polarization, and opposite to the depolarization field. This means that the switchable PV effect in the BFO thin films observed in Chapter 4 is mainly due to the depolarization field, not the BPVE. In fact, its magnitude is probably reduced by the BPVE photocurrent in the opposite direction. The photocurrent along the depolarization field direction as reported in BFO in the literature may be significantly cancelled by the BPVE, and the understanding developed here may lead to the designs that dramatically improve the PV response in ferroelectric thin films.

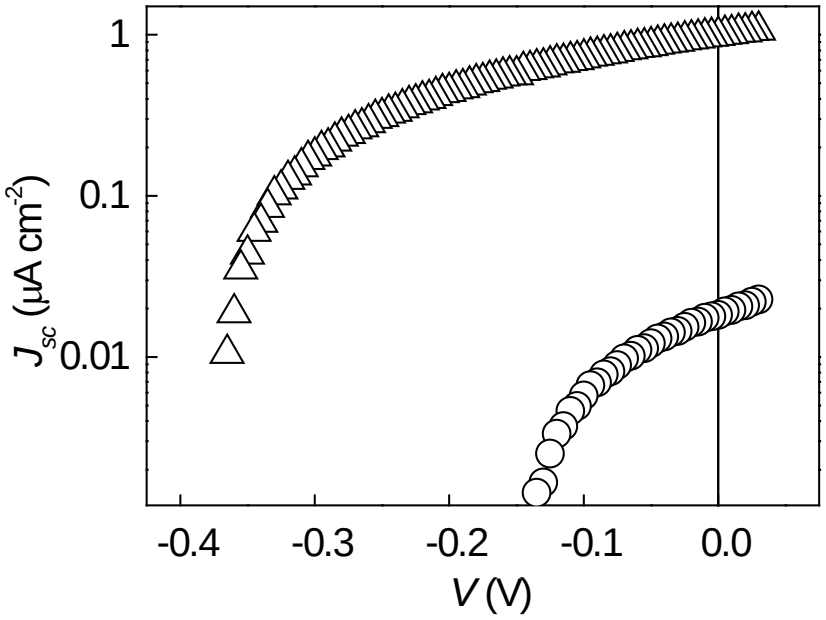

Figure 5.4 Short-circuit photocurrent densities along the surface normal in a BFO(111) film (○) and a (001)BFO film (△) at the same light intensity of 5.8 mW/cm^2, both with SRO and ITO as the bottom and the top electrode, respectively.

5.3. BPVE in polycrystalline films

There have been many reports on the PV effect in polycrystalline ferroelectric films, especially in the PLZT family. The measurement has always been along the polarization vector. Some have reported the BPVE coefficients by treating the effect entirely as the BPVE [148]. However, as has been shown by other studies, the effect of the interface and depolarization field could not be ignored in thin films [69]. Thus it is still unclear how strong the BPVE is in polycrystalline samples. In order to understand this, it is necessary to design an experiment similar to the BPVE measurements in epitaxial BFO to measure the photocurrent perpendicular to the ferroelectric polarization. The results can provide additional insight to previous results, such as the origin of the large photovoltage obtained from a WO_3-modified $(Pb_{0.97}La_{0.03})(Zr0_{.52}Ti_{0.48})O_3$ (PLWZT) sample with in-plane electrodes [79].

5.3.1. Experimental methods

Polycrystalline ferroelectric films are isotropic and belong to the point group$\infty\infty$m. Poling breaks the symmetry along the poled direction and lowers its symmetry to∞m . Its BPVE matrices are the same as point group 6mm, which has a nonzero G_{15}. As a result, there should be a photocurrent perpendicular to the polarization vector in poled polycrystalline ferroelectric films.

Polycrystalline PLWZT films with 0.5 at.% WO_3 of 1.2-μm thickness were prepared by the sol-gel method on Si with a yttria-stabilized zirconia (YSZ) buffer layer. Au in-plane electrodes were deposited by a photolithography process, and the films were poled in silicone oil. The poling direction defined the positive orientation of the z axis (Fig. 5.5). The PV effect between the in-plane electrodes was measured to verify the effectiveness of the poling process. Afterwards, a second pair of in-plane electrodes was patterned within the first pair, with the measurement direction perpendicular to the first pair. Electrodes of different dimensions were prepared. The gaps between the first pair of electrodes are 150, 200, 250 and 300 μm. The gaps between the second pair of electrodes are 5, 20 and 50 μm.

The samples were illuminated by a linearly-polarized UV light at the wavelength 365 nm. The photocurrent was measured across the second pair of electrodes while the UV light polarization angle was rotated in the plane of the film surface (Fig. 5.5).

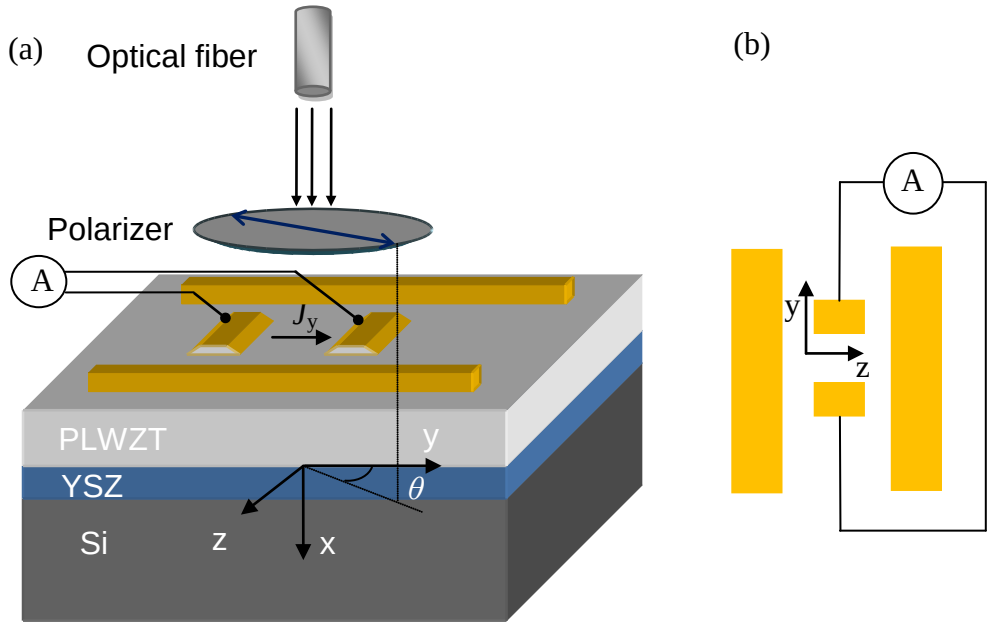

Figure 5.5 Experimental setup for the measurement of the BPVE in poled polycrystalline PLWZT. (a) Three-dimensional representation of the setup and (b) top view of the electrodes. The longer electrodes along the y axis are patterned first. The smaller electrodes are patterned after poling the first pair.

5.3.2. Theoretical model

The polarization is in-plane and defines the z axis. The incident light is perpendicular to the film surface. Its propagation direction is defined as the x axis. The y axis is determined according to the right-hand rule (Fig. 5.5).

The incident light propagates along the x axis can be expressed as

$$\begin{aligned}\vec{E} &= |E|[\hat{e}_y \cos\theta \exp i(k_o x - \omega t) + \hat{e}_z \sin\theta \exp i(k_e x - \omega t)] \\ &= |E|[\hat{e}_y e_2 \exp i(k_o x - \omega t) + \hat{e}_y e_3 \exp i(k_e x - \omega t)],\end{aligned} \qquad 5\text{-}19$$

The photocurrent tensor is calculated as before

$$[J] = I_L \alpha \begin{bmatrix} 0 & 0 & 0 & 0 & G_{15} & 0 \\ 0 & 0 & 0 & G_{15} & 0 & 0 \\ G_{31} & G_{31} & G_{33} & 0 & 0 & 0 \end{bmatrix} \begin{bmatrix} 0 \\ e_2^2 \\ e_3^2 \\ e_2 e_3^* \\ 0 \\ 0 \end{bmatrix} = I_L \alpha \begin{bmatrix} 0 \\ G_{15} e_2 e_3^* \\ G_{31} e_2^2 + G_{33} e_3^2 \end{bmatrix} \tag{5-20}$$

$$= I_L \alpha \begin{bmatrix} 0 \\ G_{15} \cos\theta \sin\theta \exp i(k_o - k_e)x \\ G_{31} \cos^2\theta + G_{33} \sin^2\theta \end{bmatrix}.$$

The photocurrent density along the y axis is

$$J_y = \frac{\alpha I_L}{2} G_{15} \sin 2\theta \exp i(k_o - k_e)x, \tag{5-21}$$

where

$$k_o - k_e = (n_o - n_e)k_{vac} = \Delta n k_{vac} = \Delta n \frac{2\pi}{\lambda_{vac}}, \tag{5-22}$$

and

$$S = \frac{2\pi}{k_o - k_e} = \frac{\lambda_{vac}}{\Delta n}, \tag{5-23}$$

Equations (5-21) to (5-23) show that the photocurrent along the y axis oscillates in the x direction with a period of *S*. It is known that PLZT has a relatively small birefringence on the order of 0.001 [1]. For the incident wavelength of 365 nm, *S* is on the order of hundreds of μm, much larger than the film thickness. As a result, the oscillation in the x direction can be ignored and the photocurrent J_y can be approximated as uniform in the thickness direction. Taking into account of the nonuniform absorption, the final expression for J_y is

$$J_y = \frac{\alpha I_L G_{15}}{2} \frac{[1 - \exp(-\alpha\delta)]}{\delta} \sin 2\theta = \frac{I_L(0)\beta_{15}}{2} \frac{[1 - \exp(-\alpha\delta)]}{\alpha\delta} \sin 2\theta, \tag{5-24}$$

where G_{15}, β_{15}, α, δ, and $I_L(0)$ are the Glass constant, the BPVE coefficient, the absorption coefficient, the film thickness, and the incident light intensity, respectively. The angle between the light polarization and the y axis is denoted as θ. The photocurrent J_y along the y axis should oscillate with the angel θ at a period of π.

5.3.3. Tensorial photocurrents in films

As shown in Fig. 5.6 negative photocurrents in the y direction is detected when the incident light is polarized parallel to the y axis. However, the magnitude of this current decreases with time. After nine repeated measurements, the photocurrent is of the same order of magnitude as the background noise. After resting the sample overnight in the dark, similar photocurrents are again detected. However, the photocurrent again decreases with time. Due to this rapid decrease of the photocurrent, it is not possible to reliably measure the photocurrent at different angles of the light polarization.

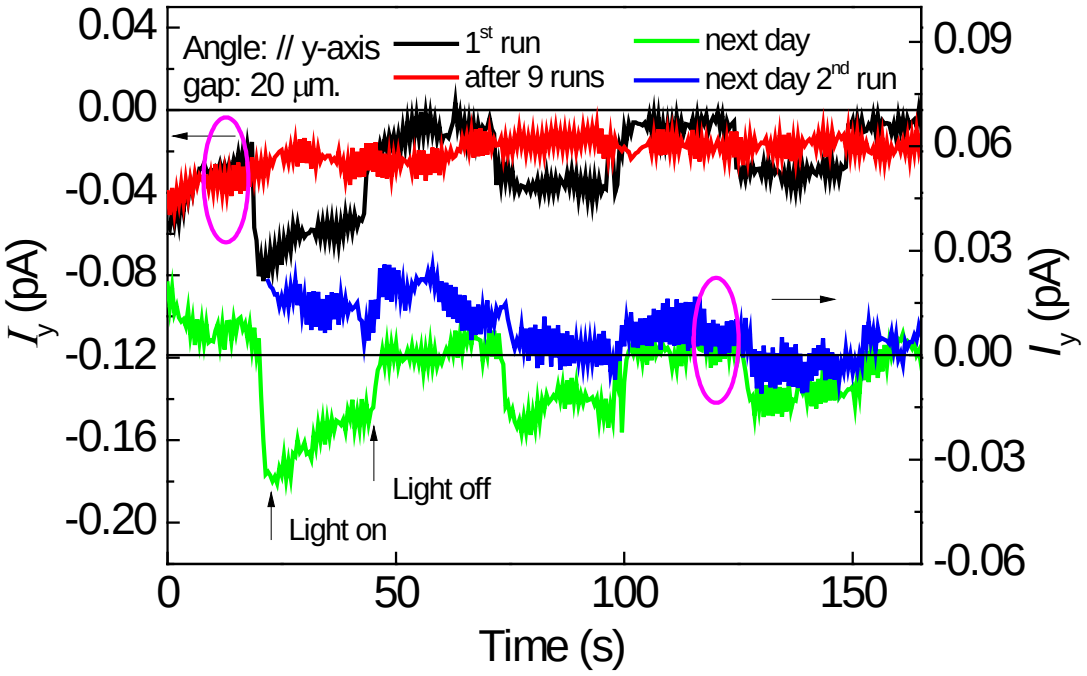

Figure 5.6 Photocurrent I_y vs. time of a PLWZT/YSZ/Si sample. Incident light is linearly polarized to be parallel to the y axis. The gap between the electrodes is 20 μm. Measurements are taken over a course of two days.

Photoexcited charge carriers can be trapped at potential wells formed at discontinuities such as defect sites and grain boundaries. Kim and Choi found that the peak PV current in their $(Pb_{1-x}La_x)TiO_3$ ceramic sample is limited by the electro-potential barrier built from the trapped photoexcited charge carriers [149]. Qin et al. have shown that photovoltage can be reduced by these trapped photoexcited charge carriers at the interfaces with electrodes [150]. Pintilie et al. have proposed that the nonuniform distribution of the trapped charges by the UV excitation caused the reversal of the photocurrent direction in repeated PV measurements in their epitaxial PZT films [132]. It appears that similar mechanism caused the degradation of the PV response in the present experiment. The photoexcited holes and electrons can be trapped near opposite electrodes and induce an electric field opposing the further migration of the charge carriers. In Ref. [150], the photovoltaige was reduced with

repeated UV irradiation. However, they did not mention if the photovolage could recover after leaving the samples in the dark for a long time. In Ref. [132], the reversal of the photocurrent occurs after leaving the samples for days in the dark. This suggests that the trapped states have a relatively long lifetime and can take hours or even days to detrap. The BPVE appears to be too weak in these polycrystalline samples to be accurately measured.

5.4. BFO as a photovoltaic material

The highest efficiency of the BFO films obtained here is 0.0052% with a blue light. At air mass (AM) 1.5, the highest efficiency is only about 5.3×10^{-4}% at a photovoltage of 0.2 V (Fig. 5.7). This efficiency is very small compared to those obtained in Si solar cells, or even in the organic solar cells. At such a low efficiency, BFO is not ideal to be used for solar energy harvesting.

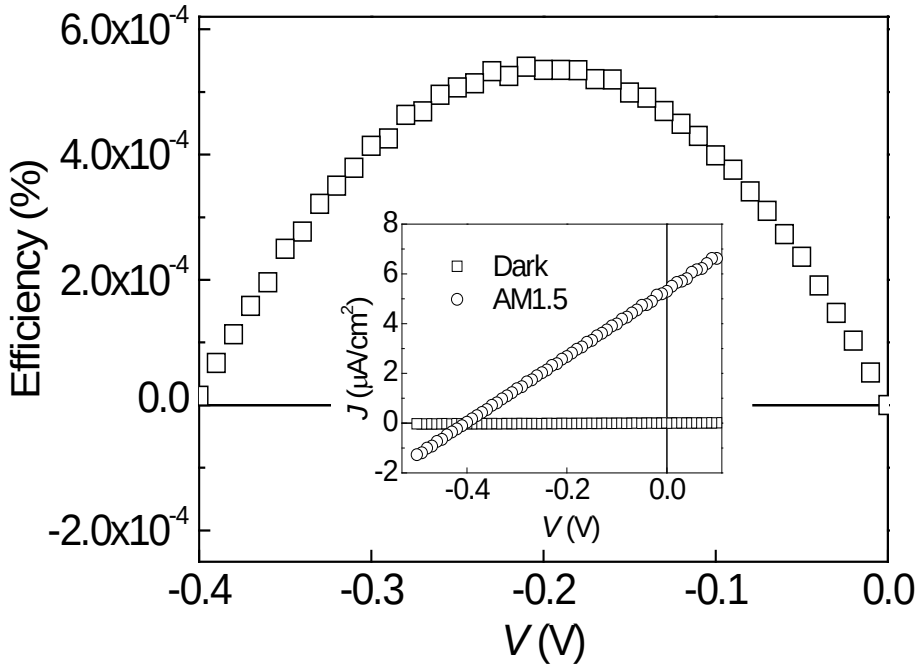

Figure 5.7 Efficiency of ITO/BFO/SRO/STO(001) at AM 1.5. Inset shows the corresponding *J*-*V* curves.

However, as the works in Chapters 4 have demonstrated, the efficiency of the BFO films can be increased by the optimization of the electrode materials. The works in this chapter also show that the low efficiency in BFO films is partly because the photocurrent from the depolarization field and the BPVE cancels each other. A different ferroelectric material with the BPVE current in the same direction as the polarization would probably improve the efficiency. Alternatively ferroelectrics can be used in a heterostructure with other materials to improve the performance and the efficiency. One example is the use of ferroelectric polymers in organic solar cells, which sees an efficiency improvement from 1-2% to 4-5% [151]. Yang and coworkers incorporated narrow bandgap AgO nanoparticles in PZT and obtained an efficiency of 0.195% under white light. Cao et al. obtained an efficiency of 0.57% at AM 1.5 by incorporating an n-type Cu_2O layer between the PZT and the Pt electrode [152]. These encouraging results show that the PV performance of ferroelectric materials can be improved if we can overcome their limitations by optimal designs.

Apart from solar energy harvesting, the works on the photovotlaic effects in ferroelectric materials could have other applications. As noted by Kreisel et al, it is the coupling of the polarization with other properties in ferroelectric materials that make them interesting [153]. The various photo-induced effects in ferroelectrics can lead us to a "wide field of possible investigations into interesting physics and possible new applications" [153].

5.5. Conclusions

The photocurrent under polarized visible light in the plane of the surface in epitaxial BFO thin films with polarization in the thickness direction is investigated. The

photocurrent in the plane perpendicular to the ferroelectric polarization (i.e., perpendicular to the depolarization field) was observed in a ferroelectric thin film for the first time. The effects from film-electrode junctions were eliminated by the use of symmetric in-plane electrodes. This gives the first evidence of a strong BPVE in the epitaxial BFO films as thin as 40 nm. The direction of the BPVE photocurrent along the film thickness direction is postulated to be the same as the polarization. Combined with the results from Chapter 4, this indicates that in a sandwich-structure device with thin film BFO the photocurrent is predominantly from the depolarization field. The photocurrent is probably reduced to some extent by the photocurrent from the BPVE that flows in the opposite direction. In addition, it was noted that the bulk PV tensor coefficient in BFO thin films is about five orders of magnitude larger than that of other typical ferroelectric materials at visible light wavelength, making BFO a much more suitable material for further investigation for PV applications compared to other ferroelectric materials, such as LNO and PLZT.

In contrast, in a polycrystalline PLWZT sample the magnitude of the photocurrent perpendicular to the ferroelectric polarization decreases with time. This photocurrent is probably caused by the BPVE as the electrodes are symmetric and the current direction is perpendicular to the depolarization field. But it cannot be determined conclusively here as the fast-dying photocurrent does not allow the determination of the relationship between the photocurrent and the incident light polarization. It is possible the photoexcited charge carriers are trapped by the large amount of defects and grain boundaries. The trapped charge carriers establish an electric field opposing the further movement of carriers and quickly quench the photocurrent.

The results here show that both the BPVE and depolarization field cause photocurrents in ferroelectric thin film devices. In BFO the direction of the photocurrent from these two mechanisms are probably opposite. For designing a PV device with ferroelectric materials, it is important to consider both effects in the sandwich-structure thin films in order to achieve the desired performance.

Chapter 6. Photoelectrolysis with $BiFeO_3$ thin films as photoelectrodes

6.1. Introduction

The PV effect in ferroelectric materials has unique features such as larger-than-bandgap photovoltages and switchable photocurrents. However, as energy harvesting materials, most ferroelectrics face a fundamental problem that limits their efficiencies. That problem is their large bandgaps. There have been efforts recently to engineer the bandgap of the ferroelectric materials, in particular by layered B-cation ordering, in order to break this limit [154, 155]. On the other hand, solar power can also be converted into chemical energy directly by the photoelectrolysis of water. It is known that the minimum bandgap for this reaction is 1.23 eV, while for a practical device the bandgap should be larger to overcome Ohmic losses and provide enough overvoltage. BFO has a relatively small bandgap of about 2.7 eV, corresponding to the blue light. Its band positions also straddle the water redox levels. As a result, BFO might be a suitable material for photoelectrolysis.

6.2. Theory of photoelectrolytic water splitting reaction

In the water splitting reaction, water molecules are dissociated into oxygen and hydrogen. The two half-cell reactions are

$$2OH^- \leftrightarrow H_2O + \frac{1}{2}O_2 - 2e^- \qquad 6\text{-}1$$

for the oxygen evolution reaction at the anode, and

$$2H^+ + 2e^- \leftrightarrow H_2 \qquad 6\text{-}2$$

for the hydrogen evolution reaction at the cathode. The standard half-cell potentials for the anode and the cathode reaction are 1.23 V and 0 V, respectively. By convention, the standard electrode potential of the full cell can be calculated as

$$E^{o} = E^{o}_{\text{cathode}} - E^{o}_{\text{anode}} = \text{-1.23 V.} \qquad 6\text{-}3$$

The full reaction can be written as

$$\mathrm{H_2O} \leftrightarrow \frac{1}{2}\mathrm{O_2} + \mathrm{H_2}. \qquad 6\text{-}4$$

The standard Gibbs free energy change ΔG^{O} for the reaction is

$$\Delta G^{O} = -2FE^{o} = 237 \text{ kJ/mol}, \qquad 6\text{-}5$$

where F is the Faraday's constant ($F = qN_A$ = 96485.3 C/mol). The number 2 denotes the number of electrons exchanged between the reactant and the oxidant.

The free energy change in Eq. (6-5) is positive. This reaction is thermodynamically impossible and cannot proceed spontaneously. In order to dissociate the water molecules into oxygen and hydrogen, energy needs to be supplied from an external source. Conventionally hydrogen has been produced by water electrolysis, where a voltage larger than 1.23 V is applied. Alternatively, this energy can be supplied by photons as well

$$\mathrm{H_2O} \xrightarrow{\mathrm{hv}} \frac{1}{2}\mathrm{O_2} + \mathrm{H_2}. \qquad 6\text{-}6$$

However, because water does not absorb photons efficiently, a catalyst is usually required to do the job. TiO_2 has been successfully demonstrated to catalyze the water

splitting by absorbing light in the UV region, although an external electrical bias is often required due to its unfavorable band positions.

A typical photoelectrolytic cell uses an n-type semiconductor as the photoanode to produce oxygen, while hydrogen is evolved at a metal cathode. A different approach can be adopted, where a p-type semiconductor is used as the photocathode and a metal as the anode. In the first approach an oxide is commonly used as the n-type semiconductor due to its stability during an anodic reaction. The operation of a photoelectrolytic cell with an n-type semiconductor photoanode and a metal cathode is illustrated in Fig. 6.1. In Fig. 6.1(a), there is no contact between the semiconductor, the electrolyte, and the metal. Upon contact the Fermi levels of the semiconductor and the metal align at equilibrium, as shown in Fig. 6.1(b). Illumination creates excess charge carriers and splits the Fermi level in the semiconductor to ε_{Fn} for the majority electrons and ε_{Fp} for the minority holes [Fig. 6.1(c)]. The band bending at the semiconductor surface is reduced due to the excess charge carriers. At high incident intensities the band bending can be almost zero and the position of the Fermi level is called the flatband (ε_{FB}). In the case of Fig. 6.1(c), electrons are not able to move from the metal to reduce protons into hydrogen as its Fermi level is lower than the hydrogen redox level H^+/H_2. With an anodic bias (positive on the anode), the Fermi level of the metal cathode can be brought higher than H^+/H_2 and the full water splitting reaction can be sustained [Fig. 6.1(d)].

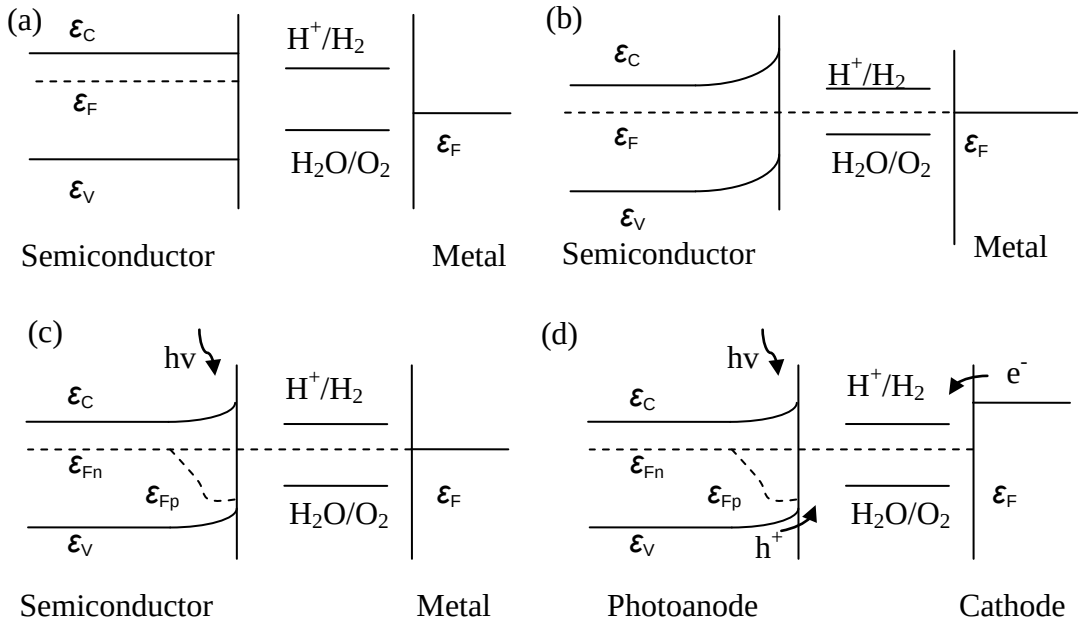

Figure 6.1 Energy diagram of a semiconductor-metal photoelectrolysis cell: (a) no contact, (b) in contact at equilibrium in dark, (c) under illumination and (d) under illumination with an external anodic bias.

From the analyses above, one can summarize the necessary conditions for a semiconductor to be useful as a photoanode in a photoelectrolytic cell to split water into hydrogen and oxygen. First, the bandgap should be larger than 1.23 eV. This is the thermodynamic limit. In any real experiment, certain amount of overpotential is required to drive the reaction at a reasonable rate. There is also some Ohmic loss in the electrolyte and the electrodes. The ideal bandgap for water splitting is from 1.6 to 2.4 eV [156]. Secondly, the quasi-Fermi levels of electrons and holes are required to straddle the redox levels. However, as the quasi-Fermi levels are not easily determined, it is common to require that the conduction and valence band edges of the semiconductor should straddle the hydrogen and oxygen redox levels. Lastly, in order to achieve unassisted photolysis, the flatband should be higher than the hydrogen

redox level for hydrogen production, or lower than the oxygen redox level for oxygen production.

6.3. $BiFeO_3$ as photoelectrodes

Semiconductor metal oxides have been widely used as photoanodes in photoelectrolytic cells. In order to achieve unassisted photoelectrolysis of water, the flatband position of the semiconductor should be higher than the H^+/H_2 potential. However, most of the semiconductor materials studied so far require certain amount of external biasing to realize water splitting. In many oxides, such as TiO_2 and STO, the valence band consists essentially of the O 2p orbital. As a result, the valence band edge of these materials is universally located near -7.44 eV (with respect to vacuum) [157]. One important consequence is that it is almost impossible to find an oxide that will simultaneously possess a small bandgap with a flatband position higher than the H^+/H_2 potential.

However, it has been shown that mixing the d-orbital from metal cations modifies the band structures and often results in smaller bandgaps. In Fe_2O_3, for example, the strong hybridization of the O 2p orbital with Fe 3d orbital results in a small bandgap of about 2.1 eV [158]. The soft and polarizable $5d^{10}6s^2$ shell of Bi^{3+} can mix with the O 2p orbital and result in a high-lying valence band [156]. These considerations led us to consider BFO for photoelectrolytic applications. Theoretical analyses show that the valence band of BFO consists of the O 2p orbital hybridized with the Fe d orbital, which also extends into the conduction band [135]. The electron affinity and the bandgap are estimated to be 3.3 eV and 2.8 eV, respectively [135]. Experimental results show that BFO has a direct bandgap of around 2.72 eV [146]. This places the BFO valence band edge below the H_2O/O_2 potential, and the conduction band edge

above the H^+/H_2 potential, with a bandgap almost ideal for water splitting. Photovoltaic measurements show that BFO is responsive to visible light and photovoltages larger than the bandgap has been reported [63]. These results indicate that BFO could possibly fulfill all the requirements as stated in Section 6.2 for unassisted water splitting reaction.

It is known that the ferroelectric polarization can modify the surface electronic structure of the material. The screening of the polarization charges by mobile carriers can cause band bending at the surface and induce depletion regions [62]. Positive polarization charges cause downward band bending (Fig. 6.2), which could facilitate the hydrogen evolution reaction. The ferroelectric polarization can modify the electron affinity as well, and thus the band edges at the surface [159]. In this case, positive polarization charges increase the electron affinity at the surface, and should promote the oxygen production. Experimentally, Inoue has shown that H_2 production is enhanced on the positive surface of the Sr-doped PZT [160], which seems to favor the first interpretation. In BFO, as the energy bands are expected to straddle the water redox levels, there is a unique opportunity to use this effect to achieve unassisted water splitting in a monolithic cell (Fig. 6.3).

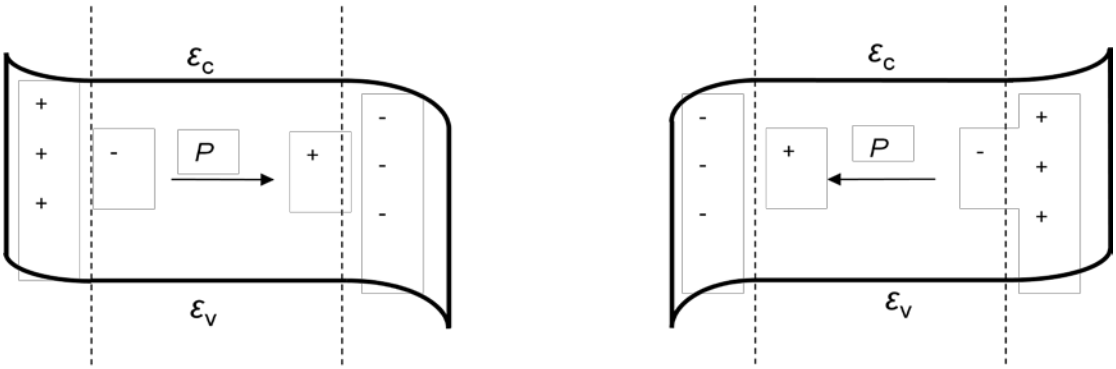

Figure 6.2 Possible ways to affect the surface electronic properties by ferroelectric polarization. Here Band bending at the surface is induced by the screening of the ferroelectric polarization.

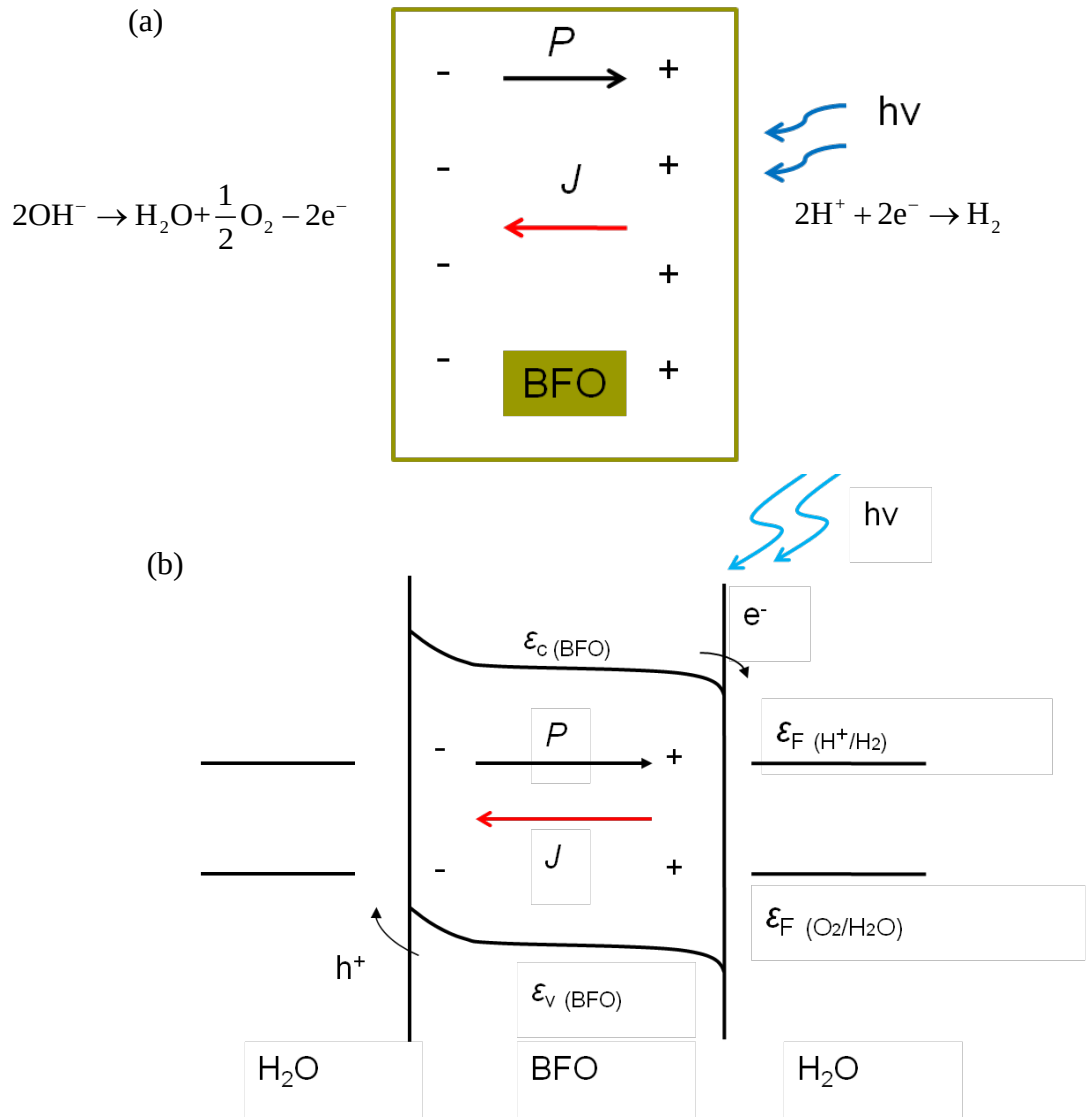

Figure 6.3 Monolithic photolytic cell for water splitting. (a) Schematic representation showing separated reaction sites on surfaces caused by the polarization charges. (b) The corresponding energy band diagram.

As a proof of concept, the first step is to study the veracity of the model, i.e., to investigate the effect of the polarization on the catalytic properties of BFO for water splitting. Although nanoparticles are often used in photoelectrolytic experiments in order to achieve large reaction areas, their polarization is difficult to control. On the other hand, epitaxial BFO thin films on SRO/STO(001) substrates have large and

well-determined polarization that can be switched. For this reason, epitaxial BFO thin films are used for this experiment.

6.4. Experimental methods

The photoelectrolytic effect of BFO thin films was investigated by linear sweep voltammetry with a three-electrode configuration (Figs. 6.4 and 6.5). Epitaxial BFO thin-film samples were prepared on the SRO/STO(001) substrates by RF sputter deposition. The bottom electrode was bonded to a gold wire and then sealed by epoxy to prevent it from direct contacts with the electrolyte. It was then connected to the working electrode of an Autolab potentiostat. The BFO surface was covered by epoxy to expose only one small area (the electrode) for the photoelectrochemical reaction and the electrical poling. The typical size of the BFO electrode is 0.017 cm^2. The counter electrode was connected to a Pt foil. A Ag/AgCl electrode was used as the reference. The experiment was carried out in a Plexiglas cell fitted with a quartz window, through which the sample was illuminated. Electrolyte Na_2SO_4 of 1 M concentration was used.

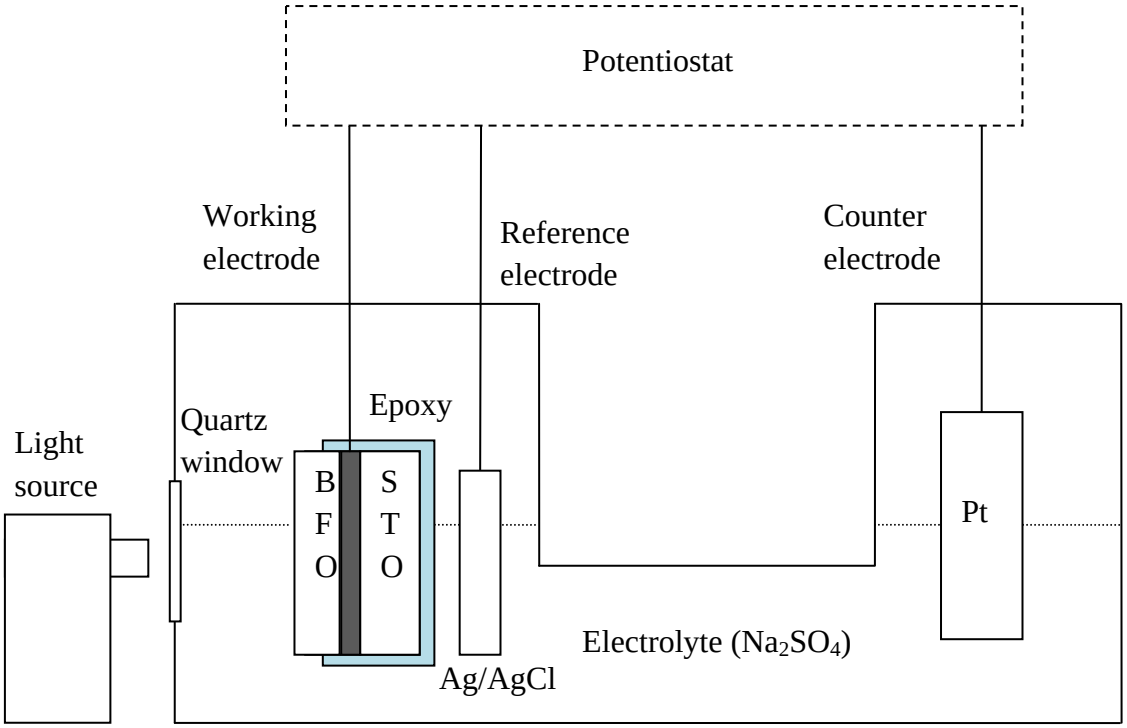

Figure 6.4 BFO photoelectrolysis experiment setup. The black strip between BFO and STO is the bottom electrode SRO, which is sealed by epoxy, except for a bonded gold wire which connects the SRO electrode to the working electrode of the potentiostat.

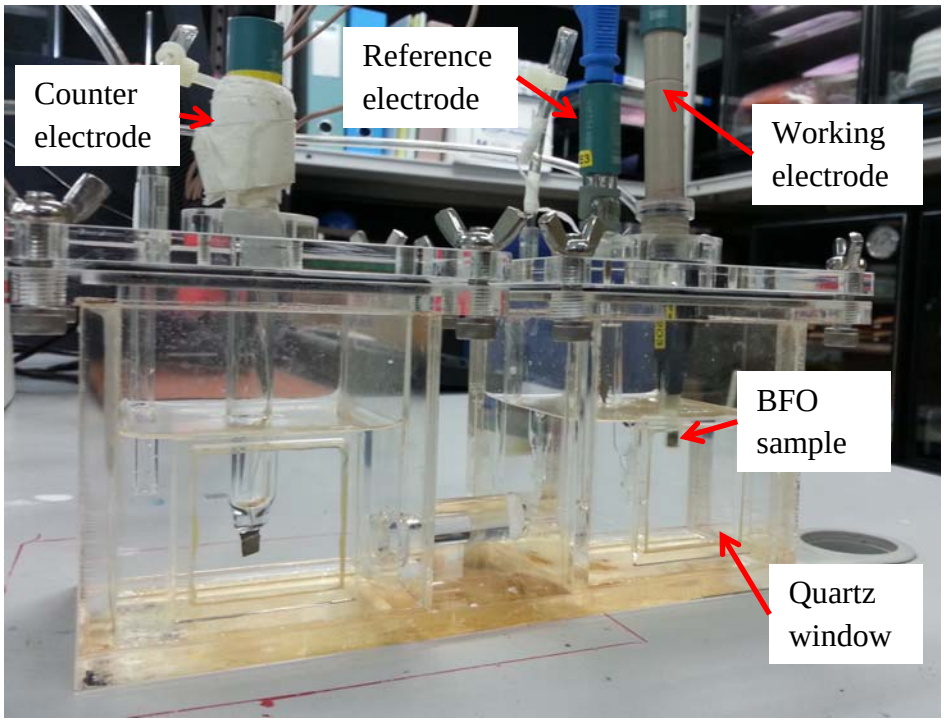

Figure 6.5 Photograph of the BFO photoelectrolysis experiment setup.

6.5. Results and discussions

For the 223-nm-thick film, considerable photocurrents are observed when the sample is under an anodic bias beyond 0.21 $V_{Ag/AgCl}$ at an incident intensity of about 121 mW/cm^2. The onset of the photocurrent is decreased to 0.18 $V_{Ag/AgCl}$ when the incident intensity is doubled [Fig. 6.6(a)]. The photocurrent is verified by using a chopper to turn on and off the light periodically. The saturated photocurrent is observed at about 0.64 $V_{Ag/AgCl}$. The magnitude is about 10 $\mu A/cm^2$ and 15 times of the dark current at the same bias voltage. In the thinner samples of 112-nm thickness, the onset of the anodic photocurrent is at -0.0157 $V_{Ag/AgCl}$ at the intensity of 121 mW/cm^2 and it is reduced to -0.0358 $V_{Ag/AgCl}$ with about double the incident intensity [Fig. 6.6(b)]. Subsequent measurements with a chopper show that the dark current increases significantly after the first two sweeps up to 0.9 $V_{Ag/AgCl}$. Upon inspection under the microscope it is found that some areas of the BFO films have been stripped off, which caused bottom SRO electrode to contact the electrolyte directly. This is probably caused by some electrocorrosion process, as indicated by the dark current onset at about 0.5 $V_{Ag/AgCl}$ in Fig. 6.6(b).

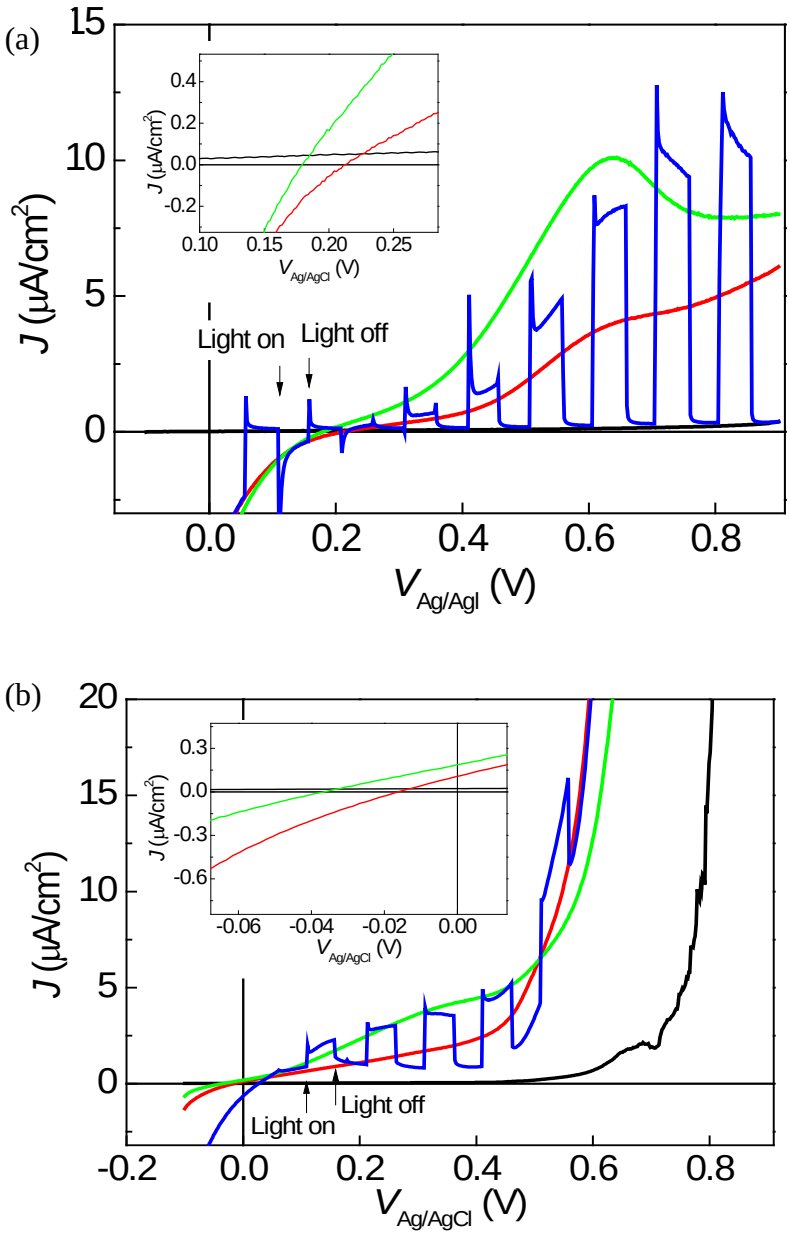

Figure 6.6 Linear sweep voltametry curves of BFO/SRO/STO(001) with different thicknesses of (a) 223 nm and (b) 112 nm. Insets show the magnified portion of the photocurrent onset. Black: dark, red: 121 mW/cm^2, blue and green: 250 mW/cm^2.

The energy band diagrams of BFO with respect to SRO, water redox levels, and Pt Fermi level are shown in Fig. 6.7. The conduction band position is determined from the electron affinity of 3.3 eV as estimated by Clark and Robertson [135]. The valence band position is then determined using the bandgap value of 2.72 eV. The band

positions straddle the water redox levels. The anodic photocurrents observed in Fig. 6.6 are probably the result of the oxygen evolution reaction. However the onset of the anodic photocurrent in the BFO thin films in this experiment is more anodic than the reports in Ref. [161], which uses BFO nanoparticles. This can be caused by the voltage drop across the bulk of the BFO films, as well as at the Schottky junctions that form at the SRO/BFO interface. Under contact at equilibrium, there is a Schottky junction between BFO and the bottom electrode SRO [Fig. 6.7(b)]. Under an anodic bias electrons need to overcome the potential barrier introduced by the band bending at the SRO/BFO interface to move from the SRO electrode into BFO. There is a smaller voltage drop in the thinner films. Furthermore, thinner films can be almost fully depleted and the band bending is reduced. As a result, the onset of the anodic photocurrent is shifted towards more negative values.

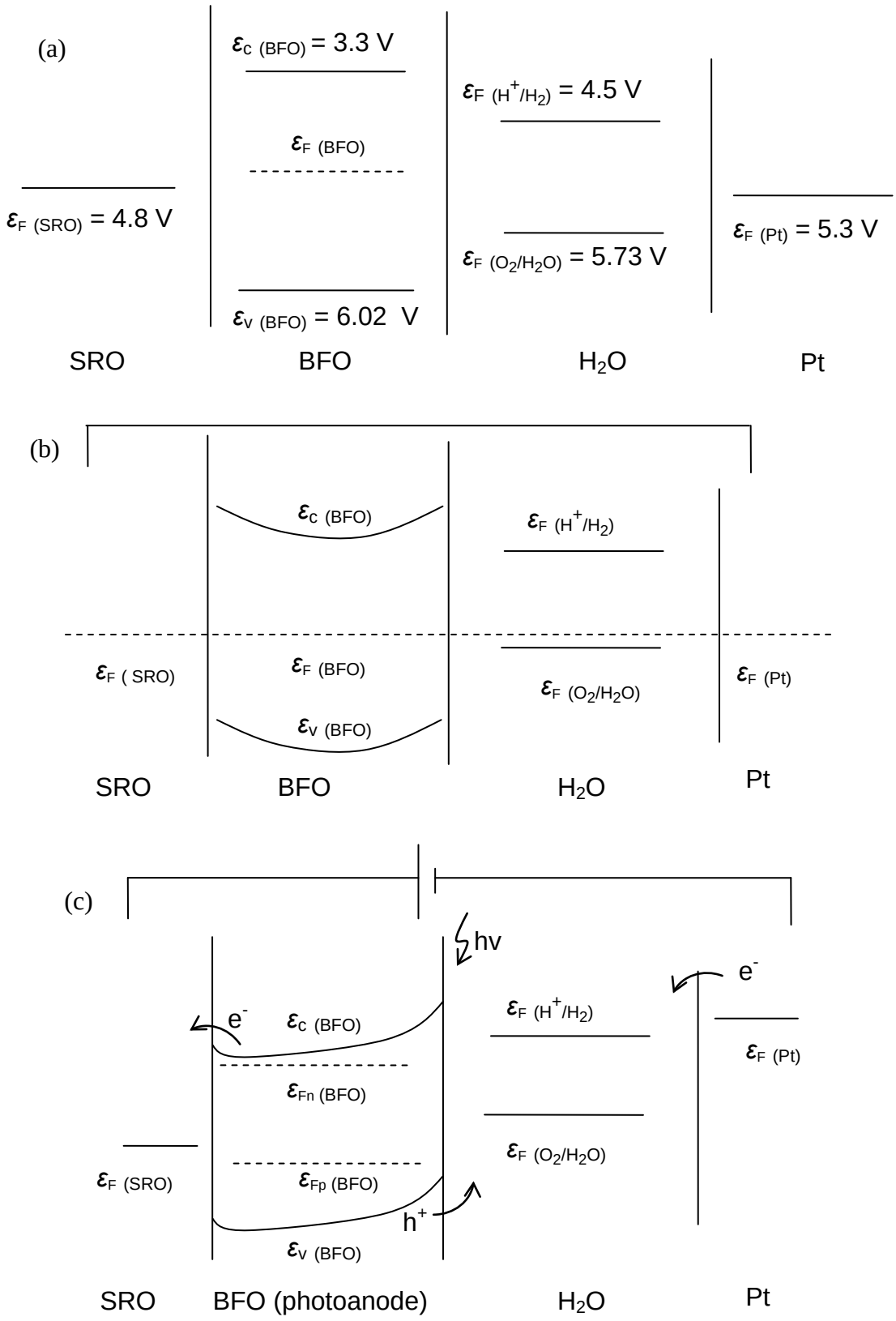

Figure 6.7 Band diagrams of the BFO/SRO/STO(001) in an electrolyte (a) before contact, (b) after contact at equilibrium in dark, and (c) after contact under illumination under anodic bias. Band positions are labeled in volt relative to the vacuum level.

As discussed earlier, the epitaxial BFO films have negative self-polarization (positive polarization charges on the film surface). This can change the surface electronic structure and the catalytic properties of the material. To investigate the effects of the polarization on the photoelectrochemical water splitting process in BFO, linear sweep voltametry measurements were carried out on as-deposited samples and again after they were positively poled. However, the results are inconclusive. One of the difficulties is that the films are easily damaged during poling. This is probably because of the larger electrode areas used in this experiment, which are more likely to contain some defects that can cause electrical shorting. As a result, the effect of the ferroelectric polarization on the photoelectrolytic properties of the BFO thin films could not be ascertained by experimental observations at this point. This difficulty may be overcome by poling the surface using some other electrode-less method, such as the oxygen-plasma poling [162].

6.6. Conclusion

A theoretical study has been carried out on the suitability of BFO as a photoelectrode for the photoelectrolytic water splitting reaction. With a bandgap of 2.7 eV and the energy bands straddling the water redox levels, BFO is very promising for the unassisted water splitting. The evolution of oxygen in BFO thin films has been observed by linear sweep voltammetry under an anodic bias. Thinner films show a Cathodic shift of the photocurrent onset, indicating a smaller Ohmic loss in these samples. The results were explained in terms of the energy band alignment of BFO with the SRO bottom electrode and the water redox levels. Furthermore, the ferroelectric polarization can modify the surface catalytic properties, with positive polarization charges causing downward band bending and negative charges causing

upward band bending. It is possible to promote the hydrogen and the oxygen evolutions at different surfaces with positive and negative polarization charges, respectively. By modifying the band structure with polarization, a monolithic water splitting cell based on the ferroelectric BFO is possible. However, difficulties remain in obtaining relatively large areas of poled surfaces for the experimental investigation of the effect of polarization on the catalytic effect.

Chapter 7. Conclusions and future work

7.1. Conclusions

This research investigated the photovoltaic properties in epitaxial BFO thin films, including an analysis on their application in water splitting. The polarization of ferroelectric BFO is found to have a significant effect on its PV responses. Appreciable photovoltages, of which the polarity is switchable by poling the polarization in different directions, are demonstrated for the first time in the BFO thin films. The evidence for the bulk photovoltaic effect has been obtained in BFO films as thin as 40 nm for the first time. Photoelectrolytic oxygen generation by the BFO thin film is demonstrated and a concept for the monolithic water splitting cell making use of the polarization property of BFO is proposed.

High quality epitaxial BFO films were prepared by the RF magnetron sputter deposition method. The structural, dielectric, optical, ferroelectric and piezoelectric properties of the samples were systematically investigated. The films grown on the STO(001) substrates are compressively strained while those on the STO(111) have the same rhombohedral structure as the bulk BFO. The samples exhibit saturated *P-E* hysteresis loops with minimal leakage currents. The resistivity of the films is on the order of 10^{12} Ω cm. Large remanent polarizations are obtained. The maximum remanent polarization observed in the BFO(111) films is 108.5 $\mu C/cm^2$, similar to the theoretical predictions. These high quality BFO samples are ideal for the investigation of the PV effect in ferroelectric thin films.

Appreciable PV responses in the visible wavelengths have been demonstrated in the epitaxial BFO thin films. The as-deposited BFO films are completely self-polarized and produce large open-circuit photovoltages up to 0.55 V (24.6 kV/cm). In the samples with the sandwich ITO/BFO/SRO structure, the interfacial Schottky barriers are found to be back-to-back and almost symmetrical due to Fermi-level pinning. Consequently, they have little effects on the PV processes. The photovoltage and the photocurrent are switchable in response to the switching of the ferroelectric polarization, with the direction of the photocurrent opposite to that of the polarization vector.

The PV effect in ferroelectric thin films could be caused by many mechanisms, such as the depolarization field and the BPVE. However, in a sandwich structure with top and bottom electrodes, and with the polarization in the thickness direction, such as the ITO/BFO/SRO(001) samples, the measured photocurrent is aligned with the polarization and the depolarization field. Consequently, it is impossible to separate these mechanisms. However, by investigating the photocurrent in the plane perpendicular to the ferroelectric polarization (i.e., perpendicular to the depolarization field) in epitaxial BFO films with symmetric electrodes under linearly-polarized visible light, I successfully measured the BPVE in the BFO samples. This is the first time the BPVE was measured in a ferroelectric thin film. Evidence of the BPVE is obtained in the epitaxial BFO films as thin as 40 nm. The BPVE tensor coefficient β_{22} is calculated to be around 1.1×10^{-4} V^{-1}, about five orders or magnitude larger than the typical values of $LiNbO_3$:Fe and $LiTaO_3$ at visible wavelengths. The photocurrent from the BPVE in the BFO film thickness direction is postulated to be in the same direction as the ferroelectric polarization.

The experimental results in this work clearly demonstrate that the photocurrent in a ITO/BFO/SRO samples is contributed by both the ferroelectric depolarization field and the BPVE. The direction of the photocurrent from these two effects is probably opposite to each other. In order to achieve higher PV efficiency, it will be ideal to have a material with the BPVE photocurrent in the same direction as that from the depolarization field. Furthermore, in the samples with the sandwich ITO/BFO/SRO structure the Schottky barriers at electrode/film interfaces are pinned at comparable levels and therefore they do not contribute significantly to the observed PV processes. The electrode materials should be optimized for the selective charge collections for electrons and holes in order to improve the PV efficiency. Optimization of the electrode materials was attempted but no improvements have been realized so far.

In addition, the photocatalytic effect of BFO on the oxygen evolution was investigated. Significant photocurrents were observed. A monolithic water splitting cell based on BFO with the photocatalytic effect modified by its ferroelectric polarization is an attractive concept for unassisted water splitting.

Although the low efficiencies in these sample make them unsuitable for solar energy harvesting applications, the new understanding from this work can help to improve the PV performance in devices based on ferroelectric thin films. In consideration of the fact that BFO has multiferroic characteristics, the combination of the ferroic-related properties in BFO with the photovoltaics as demonstrated here may lead to many new device functionalities in optoelectronic devices and even solar energy harvesting.

7.2. Future work

The investigation with epitaxial BFO films in this work has provided new insights to the mechanisms of the PV processes in a ferroelectric thin film. However the use of BFO and other ferroelectrics as a PV material remains a challenge. As is shown by the current work, the photocurrents from the depolarization field and the BPVE in BFO are probably opposite to each other, and thus partially cancel out. The Schottky junctions between BFO and electrodes are not optimized for selective charge collection either. One way to improve the efficiency is to find a material with the BPVE photocurrent in the same direction as the depolarization field. Optimization of the electrode to facilitate the selective charge collection is another route to improve the PV efficiency in ferroelectric thin films.

Although BFO has been useful for the investigation of the PV effect in ferroelectric films, its bandgap is too large for the effective solar energy harvesting. A recent study in single crystal BFO also shows significant nonradiative recombination involving complex defects [163], which pose a challenge to any attempts to improve the efficiency. Any ferroelectric material for potential solar cell application will require even smaller bandgap with good carrier mobility and lifetime. Whether such a material can be found and what kind of PV performance one can expect from it are still open questions. Some promising results have come from the use of ferroelectrics in a heterostructure with other materials. As has been shown in this work, ferroelectricity can have a large effect on the PV output. The combination of ferroelectrics with other suitable PV materials may prove fruitful in the search for improved device performance and lower cost.

As the direction and magnitude of the photocurrent in a ferroelectric can be controlled by the incident light polarization, it can lead to novel applications not possible with p-n junctions. This becomes even more interesting when it is coupled with other effects, such as piezoelectricity and multiferroicity.

In addition, ferroelectrics, such as BFO, can be used for photoelectrolytic processes, including water splitting and photooxidation of pollutants. BFO has a bandgap in the visible wavelengths and it is very close to the ideal value for water splitting. The band positions of BFO can allow unassisted water splitting. Furthermore, the ferroelectric polarization can be used to modify the surface properties to enhance different reactions on different surfaces, thus separating the evolution of H_2 and O_2 to different sites. Such a monolithic cell would be highly desirable. For such devices to succeed, it would be necessary to pole a relatively large area of a ferroelectric material, ideally without electrodes being patterned. Possible solutions include ferroelectric switching by the plasma or ion irradiation of the sample surface.

Bibliography

[1] Y. Xu, *Ferroelectric materials and their applications*. New York: North-Holland, 1991.

[2] J. F. Scott, "Applications of modern ferroelectrics," *Science,* vol. 315, pp. 954-959, 2007.

[3] G. H. Haertling, "Ferroelectric ceramics: history and technology," *J. Am. Ceram. Soc.,* vol. 82, pp. 797-818, 1999.

[4] K. Rabe, *et al.*, *Physics of ferroelectrics: a modern perspective*. Berlin, Germany: Springer, 2007.

[5] D. Damjanovic, "Ferroelectric, dielectric and piezoelectric properties of ferroelectric thin films and ceramics," *Rep. Prog. Phys,* vol. 61, pp. 97-98, 1998.

[6] M. Dawber, *et al.*, "Physics of thin-film ferroelectric oxides," *Rev. Mod. Phys.,* vol. 77, pp. 1083-1130, 2005.

[7] M. Dawber, *et al.*, "Depolarization corrections to the coercive field in thin-film ferroelectrics," *J. Phys.: Condens. Matter,* vol. 15, pp. L393-L398, 2003.

[8] A. M. Glass and M. E. Lines, *Principles and applications of ferroelectrics and related materials*. Oxford, UK: Clarendon press, 1979.

[9] C. A. Randall, *et al.* (1st June). *History of the ferroelectric oxide, $BaTiO_3$* [Online]. Available: http://ceramics.org/wp-content/uploads/2009/05/first_ferroelectric_oxide_ba_tio3.pdf

[10] S.-J. Jang, "Ferroelectrics," in *Kirk-Othmer encyclopedia of chemical technology* vol. 11, J. I. Kroschwitz, Ed., ed. Hoboken, NJ: John Wiley & Sons, Inc, 2004.

[11] F. S. Kubel, H., "Structure of a ferroelectric and ferroelastic monodomain crystal of the perovskite $BiFeO_3$," *Acta Cryst.*, vol. B46, pp. 698-702, 1990.

[12] V. V. Lazenka, *et al.*, "Structural transformation and magnetoelectric behaviour in $Bi_{1-x}Gd_xFeO_3$ multiferroics," *J. Phys. D: Appl. Phys.*, vol. 45, p. 125007, 2012.

[13] G. Catalan and J. F. Scott, "Physics and applications of bismuth ferrite," *Adv. Mater.*, vol. 21, pp. 1-23, 2009.

[14] R. Palai, *et al.*, "β phase and γ-β metal-insulator transition in multiferroic $BiFeO_3$," *Phys. Rev. B,* vol. 77, p. 014110, 2008.

[15] M. S. Selbach, *et al.*, "The ferroic phase transitions of $BiFeO_3$," *Adv. Mater.*, vol. 20, p. 3692, 2008.

[16] J. R. Teague, *et al.*, "Dielectric hysteresis in single crystal $BiFeO_3$," *Solid State Commun.*, vol. 8, pp. 1073-1074, 1970.

[17] J. Wang, *et al.*, "Epitaxial $BiFeO_3$ multiferroic thin film heterostructures," *Science,* vol. 299, pp. 1719-1722, 2003.

[18] W. Eerenstein, *et al.*, "Comment on "Epitaxial $BiFeO_3$ Multiferroic Thin Film Heterostructures"," *Science,* vol. 307, p. 1203a, 2005.

[19] J. B. Neaton, *et al.*, "First-principles study of spontaneous polarization in multiferroic $BiFeO_3$," *Phys. Rev. B,* vol. 7, p. 014113, 2005.

[20] D. Lebeugle, *et al.*, "Very large spontaneous electric polarization in $BiFeO_3$ single crystals at room temperature and its evolution under cycling fields," *Appl. Phys. Lett.*, vol. 91, p. 022907, 2007.

[21] N. A. Hill, "Why are there so few magnetic ferroelectrics?," *J. Phys. Chem. B,* vol. 104, pp. 6694-6709, 2000.

[22] T. Zhao, *et al.*, "Electrical control of antiferromagnetic domains in multiferroic $BiFeO_3$ films at room temperature," *Nat. Mater.*, vol. 5, pp. 823-829, 2006.

[23] W. Prellier, *et al.*, "The single-phase multiferroic oxides: From bulk to thin film," *J. Phys. Condens. Matter,* vol. 17, pp. R803-R832, 2005.

[24] F. Zavaliche, *et al.*, "Multiferroic BiFeO3 films: domain structure and polarization dynamics," *Phase Transit.*, vol. 79, pp. 991-1017, 2006.

[25] R. Ramesh and N. A. Spaldin, "Multiferroics: progress and prespects in thin films," *Nat. Mater.*, vol. 6, pp. 21-29, 2007.

[26] A. Roy, *et al.*, "Multiferroic memories," *Adv. Cond. Matter Phys.*, vol. 2012, p. 926290, 2012.

[27] K. Prashanthi, *et al.*, "Fabrication and characterization of a novel magnetoelectric multiferroic MEMS cantilevers on Si," *Sens. Actuators A, Phys.*, vol. 166, pp. 83-87, 2011.

[28] H. Bea, *et al.*, "Spintronics with multiferroics," *J. Phys.: Condens. Matter,* vol. 20, p. 434221, 2008.

[29] H. Bea, *et al.*, "Tunnel magnetoresistance and robust room temperature exchange bias with multiferroic $BiFeO_3$ epitaxial thin films," *App. Phys. Lett.*, vol. 89, p. 242114, 2006.

[30] S. W. Cheong and M. Mostovoy, "Multiferroics: a magnetic twist for ferroelectricity," *Nat. Mater.*, vol. 6, pp. 13-20, 2007.

[31] S. M. Wu, *et al.*, "Reversible electric control of exchange bias in a multiferroic field-effect device," *Nat. Mater.*, vol. 9, pp. 756-761, 2010.

[32] D. Talbayev, *et al.*, "Terahertz wave generation via optical rectification from multiferroic $BiFeO_3$," *App. Phys. Lett.*, vol. 93, p. 212906, 2008.

[33] R. Thomas, *et al.*, "Multiferroic thin-film intergration onto semiconductor devices," *J. Phys.: Condens. Matter*, vol. 22, p. 423201, 2010.

[34] C.-S. Yeh and J.-M. Wu, "Characterization of Pt/multiferroic $BiFeO_3$/(Ba,Sr)TiO_3/Si stacks for nonvolatile memory applications," *App. Phys. Lett.*, vol. 93, p. 154101, 2008.

[35] Fujitsu. (2006, 30th June). *Fujitsu and Tokyo Institute of Technology announce the development of new naterial for 256Mbit FeRAM Using 65-nanometer technology* [Online]. Available: http://www.fujitsu.com/sg/news/pr/fmal_20060808.html

[36] A. Slaoui and R. T. Collins, "Advanced inorganic materials for photovoltaics," *MRS Bulletin*, vol. 32, pp. 211-218, 2007.

[37] A. Zervos, *et al.*, "Mapping renewable energy pathways towards 2020," European renewable energy council, 2011.

[38] V. Fthenakis, *et al.*, "The technical, geograhical, and economic feasibility for solar energy to supply the energy needs of the US," *Energy Policy*, vol. 37, pp. 387-399, 2009.

[39] A. Goetzberger, *et al.*, "Photovoltaic materials, history, status and outlook," *Mater. Sci. Eng. R*, vol. 40, pp. 1-46, 2003.

[40] D. Chapin, *et al.*, "A new p-n junction photocell for converting solar radiation into electrical power," *Appl. Phys*, vol. 25, pp. 676-677, 1954.

[41] J. Nelson, *The physics of solar cells*. London: Imperial College Press, 2003.

[42] M. A. Green, *et al.*, "Solar cell efficiency tables (version 39)," *Prog. Photovoltaics: Research and Applications*, vol. 20, pp. 12-20, 2012.

[43] M. L. Timmons, "Current realities and future prospects for high-efficiency solar cells," *Aerosp. Conf., 1998. Proc., IEEE*, vol. 1, pp. 131-140, 1998.

[44] A. W. Bett, *et al.*, "III-V compounds for solar cell applications," *Appl. Phys. A*, vol. 69, pp. 119-129, 1999.

[45] S. J. Fonash, *Solar cell device physics*. New York: Academic Press, 1981.

[46] J. A. Mazer, *Solar cells: an introduction to crystalline photovoltaic technology*. Boston: Kluwer Academic Publishers, 1997.

[47] R. E. I. Schropp, *Amorphous and microcrystalline silicon solar cells: modeling, materials, and device technology*. Boston: Kluwer Academic, 1998.

[48] H. J. Moller, *Semiconductors for solar cells*. Boston: Artech House, 1993.

[49] A. Goetzberger, *et al.*, "Photovoltaic materials, history, status and outlook," *Mater. Sci. Eng. R*, vol. 40, pp. 1-46, 2003.

[50] M. Gratzel, "Dye-sensitized solid-state heterojunction solar cells," *MRS Bulletin*, vol. 30, pp. 23-27, 2005.

[51] B. A. Gregg, "The photoconversion mechanism of excitonic solar cells," *MRS bulletin*, vol. 30, pp. 20-22, 2005.

[52] B. A. Gregg, "Excitonic solar cells," *J. Phys. Chem. B*, vol. 107, pp. 4688-4698, 2003.

[53] A. G. Chynoweth, "Surface space-charge layers in barium titanate," *Phys. Rev.*, vol. 102, pp. 705-714, 1956.

[54] A. M. Glass, *et al.*, "High-voltage bulk photovoltaic effect and the photorefractive process in $LiNbO_3$," *Appl. Phys. Lett.*, vol. 25, pp. 233-235, 1974.

[55] V. M. Fridkin, "Bulk photovoltaic effect in noncentrosymmetric crystals," *Crystallography Reports*, vol. 46, pp. 654-8, 2001.

[56] W. T. H. Koch, *et al.*, "Bulk photovoltaic effect in $BaTiO_3$," *Solid State Commun.*, vol. 17, pp. 847-850, 1975.

[57] B. I. Sturman and V. M. Fridkin, *The photovoltaic and photorefractive effects in noncentrosymmetric materials*. Philadelphia: Gordon and Breach Science Publishers, 1992.

[58] G. Dalba, *et al.*, "Giant bulk photovoltaic effect under linearly polarized x-ray synchrotron radiation," *Phys. Rev. Lett.*, vol. 74, pp. 988-991, 1995.

[59] G. Chanussot and A. M. Glass, "A bulk photovoltaic effect due to electron-phonon coupling in polar crystals," *Phys. Lett. A*, vol. 59, pp. 405-407, 1976.

[60] P. S. Brody and F. Crowne, "Mechanism for the high voltage photovoltaic effect in ceramic ferroelectrics," *J. Elect. Mater*, vol. 4, pp. 955-971, 1975.

[61] K. Tonooka, *et al.*, "Mechanism of the bulk photovoltaic effect in ferroelectrics," *SPIE*, vol. 3324, pp. 224-232, 1998.

[62] G.-L. Yuan, "Evidences for the depletion region induced by the polarization of ferroelectric semiconductors," *App. Phys. Lett.*, vol. 95, p. 252904, 2009.

[63] S. Y. Yang, *et al.*, "Above-bandgap voltages from ferroelectric photovoltaic devices," *Nat. Nanotechnol.*, vol. 5, pp. 143-147, 2010.

[64] B. Meyer and D. Vanderbilt, "Ab initio study of ferroelectric domain walls in $PbTiO_3$," *Phys. Rev. B*, vol. 65, p. 104111, 2002.

[65] J. Seidel, *et al.*, "Conduction at domain walls in oxide multiferroics," *Nat. Mater.*, vol. 8, pp. 229-234, 2009.

[66] M. Alexe and D. Hesse, "Tip-enhanced photovoltaic effects in bismuth ferrite," *Nat. Commun.*, vol. 2, pp. 1-5, 2011.

[67] P. Wurfel and I. P. Batra, "Depolarization-field-induced instability in thin ferroelectric films-experiment and theory," *Phys. Rev. B*, vol. 8, pp. 5126-5132, 1973.

[68] M. Qin, *et al.*, "Thickness effects on photoinduced current in ferroelectric $(Pb_{0.97}La_{0.03})(Zr_{0.52}Ti_{0.48})O_3$ thin films," *J. Appl. Phys.*, vol. 101, p. 014104, 2007.

[69] M. Qin, *et al.*, "Photovoltaic mechanisms in ferroelectric thin films with the effects of the electrodes and interfaces," *App. Phys. Lett.*, vol. 95, p. 022912, 2009.

[70] M. Qin, *et al.*, "High efficient photovoltaics in nanoscaled ferroelectric thin films," *Appl. Phys. Lett.*, vol. 93, p. 122904, 2008.

[71] I. P. Batra, *et al.*, "Phase transition, stability, and depolarization field in ferroelectric thin films," *Phys. Rev. B*, vol. 8, pp. 3257-3265, 1973.

[72] I. P. Batra and B. D. Silverman, "Thermodynamic stability of thin ferroelectric films," *Solid State Commun.*, vol. 11, pp. 291-294, 1972.

[73] L. Pintilie and M. Alexe, "Metal-ferroelectric-metal heterostructures with Schottky contacts. I. Influence of the ferroelectric properties," *J. Appl. Phys.*, vol. 98, p. 124103, 2005.

[74] L. Pintilie, *et al.*, "Metal-ferroelectric-metal structures with Schottky contacts. II. Analysis of the experimental current-voltage and capacitance-voltage characteristics of $Pb(Zr,Ti)O_3$ thin films," *J. Appl. Phys.*, vol. 98, p. 124104, 2005.

[75] F. S. Chen, "Optically Induced Change of Refractive Indices in $LiNbO_3$ and $LiTaO_3$," *J. Appl. Phys.*, vol. 40, pp. 3389-3396, 1969.

[76] K. Buse, "Light-induced charge transport processes in photorefractive crystals I: Models and experimental methods," *Appl. Phys. B*, vol. B64, pp. 273-291, 1997.

[77] K. Buse, "Light-induced charge transport processes in photorefractive crystals II: materials," *Appl. Phys. B,* vol. 64, pp. 391-407, 1997.

[78] R. R. Mehta, *et al.*, "Depolarization fields in thin ferroelectric films," *J. Appl. Phys.,* vol. 44, pp. 3379-3385, 1973.

[79] K. Yao, *et al.*, "Large photo-induced voltage in a ferroelectric thin film with in-plane polarization," *Appl. Phys. Lett.,* vol. 87, p. 212906, 2005.

[80] B. K. Gan, *et al.*, "An ultraviolet (UV) detector using a ferroelectric thin film with in-plane polarization," *IEEE Electron Device Lett.,* vol. 29, pp. 1215-17, 2008.

[81] J. F. Ihlefeld, *et al.*, "Optical band gap of $BiFeO_3$ grown by molecular-beam epitaxy," *Appl. Phys. Lett.,* vol. 92, p. 142908, 2008.

[82] J. Wang, *et al.*, "Response to comment on "Epitaxial $BiFeO_3$ multiferroic thin film heterostructures"," *Science,* vol. 307, p. 1203b, 2005.

[83] S. R. Basu, *et al.*, "Photoconductivity in $BiFeO_3$ thin films," *Appl. Phys. Lett.,* vol. 92, p. 091905, 2008.

[84] A. J. Hauser, *et al.*, "Characterization of electronic structure and defect states of thin epitaxial $BiFeO_3$ films by UV-visible absorption and cathodoluminescence spectroscopies," *Appl. Phys. Lett.,* vol. 92, p. 222901, 2008.

[85] A. Kumar, *et al.*, "Linear and nonlinear optical properties of $BiFeO_3$," *Appl. Phys. Lett.,* vol. 92, p. 121915, 2008.

[86] T. Choi, *et al.*, "Switchable ferroelectric diode and photovoltaic effect in $BiFeO_3$," *Science,* vol. 324, pp. 63-66, 2009.

[87] C. A. Grimes, *et al., Light, water, hydrogen: the solar generation of hydrogen by water photoelectrolysis*. New York: Springer, 2008.

[88] A. Fujishima and K. Honda, "Electrochemical photolysis of water at a semiconductor electrode," *Nature,* vol. 238, pp. 37-38, 1972.

[89] S. Dunn and D. Tiwari, "Influence of ferroelectricity on the photoelectric effect of $LiNbO_3$," *App. Phys. Lett.,* vol. 93, p. 092905, 2008.

[90] P. M. D. Jones, S., "Photo-reduction of silver salts on highly heterogeneous lead zirconate titanate," *Nanotechnology,* vol. 18, p. 185702, 2007.

[91] L. Lahoche, *et al.*, "Substrate-induced mechanical and dielectric properties of a ferroelectric thin film," *J. Appl. Phys.,* vol. 91, pp. 4973-4982, 2002.

[92] D. G. Schlom, *et al.*, "Strain tuning of ferroelectric thin films," *Annu. Rev. Mater. Res.,* vol. 37, pp. 589-626, 2007.

[93] R. Y. Zheng, *et al.*, "Multiferroic $BiFeO_3$ thin films deposited on $SrRuO_3$ buffer layer by rf sputtering," *J. Appl. Phys.*, vol. 101, p. 54104, 2007.

[94] H. W. Jang, *et al.*, "Strain-induced polarization rotation in epitaxial (001) $BiFeO_3$ thin films," *Phy. Rev. Lett.*, vol. 101, p. 107602, 2008.

[95] H. N. Lee, *et al.*, "Suppressed dependence of polarization on epitaxial strain in highly polar ferroelectrics," *Phys. Rev. Lett.*, vol. 98, p. 217602, 2007.

[96] K. Wasa, *et al.*, "Structure and ferroelectric properties of single crystal PMNT thin films," *Integr. Ferroelectr.*, vol. 70, pp. 131-140, 2005.

[97] W. K. Burton, *et al.*, "The growth of crystals and the equilibrium of their surfaces," *Phil. Trans. Royal Soc.*, vol. A243, pp. 299-358, 1951.

[98] M. Kawasaki, *et al.*, "Atomic control of the $SrTiO_3$ crystal surface," *Science*, vol. 266, pp. 1540-1542, 1994.

[99] G. Koster, "Artificially layered oxides by pulsed laser deposition," Ph.D. dissertation, Universiteit Twente, Enschede, the Netherlands, 1999.

[100] G. J. Collins and D. M. Shaw, "Chapter 4 Introduction to gas discharges and plasmas," in *Plasma and thin film*. 1999

[101] D. K. Schroder, *Semiconductor material and device characterization*, 3rd ed. Hoboken, N. J.: John Wiley & Sons, Inc.

[102] R. Waser, *et al.*, Eds., *Polar oxides: properties, characterization, and imaging*. Weinheim: Viley-VCH, 2005.

[103] L. Pardo, *et al.*, "Impedance measurements for determination of the elastic and piezoelectric coefficients of films," *Adv. Appl. Ceram.*, vol. 109, pp. 156-161, 2010.

[104] K. Yao and F. E. H. Tay, "Measurement of longitudinal piezoelectric coefficient of thin films by a laser-scanning vibrometer," *IEEE Trans. Ultrason. Ferroelectr. Freq. Control*, vol. 50, pp. 113-116, 2003.

[105] H. Yang, *et al.*, "Temperature-dependent leakage mechanisms of $Pt/BiFeO_3/SrRuO_3$ thin film capacitors," *Appl. Phys. Lett.*, vol. 91, p. 072911, 2007.

[106] P. Zubko, *et al.*, "Electrical characterization of $PbZr_{0.4}Ti_{0.6}O_3$ capacitors," *J. Appl. Phys.*, vol. 100, p. 114113, 2006.

[107] J. F. Scott, "Depletion width in $SrTiO_3$ and $Ba_xSr_{1-x}TiO_3$ films," *Ferroelectr.*, vol. 232, pp. 25-34, 1999.

[108] M. S. Bernardo, *et al.*, "Reaction pathways in the solid state synthesis of multiferroic $BiFeO_3$," *J. Eur. Ceram. Soc.*, vol. 31, pp. 3047-3053, 2011.

[109] M. M. Kumar, *et al.*, "Ferroelectricity in a pure $BiFeO_3$ ceramic," *App. Phys. Lett.*, vol. 76, pp. 2764-2766, 2000.

[110] V. V. Shvartsman, *et al.*, "Large bulk polarization and regular domain structure in ceramic $BiFeO_3$," *App. Phys. Lett.*, vol. 90, p. 172115, 2007.

[111] W. Waczmarek, *et al.*, "Differential thermal analysis of phase transitions in $(Bi_{1-x}La_x)FeO_3$ solid solution," *Solid State Commun.*, vol. 17, pp. 807-810, 1975.

[112] T. Kamo, *et al.*, "RF magnetron sputtering growth of epitaxial $SrRuO_3$ films with high conductivity," *Jpn. J. Appl. Phys., 1,* vol. 46, pp. 6987-6990, 2007.

[113] C. B. Eom, *et al.*, "Growth and characterization of epitaxial thin films of conductive ferromagnetic oxide $SrRuO_3$," *J. Appl. Phys.*, vol. 83, pp. 6539-6541, 1998.

[114] M. Hiratani, *et al.*, "$SrRuO_3$ thin films grown under reduced oxygen pressure," *Jpn. J. Appl. Phys.*, vol. 35, pp. 6212-6216, 1996.

[115] P. B. Allen, *et al.*, "Transport properties, thermodynamic properties, and electronic structure of $SrRuO_3$," *Phys. Rev. B,* vol. 53, pp. 4393-4398, 1996.

[116] S. C. Gausepohl, *et al.*, "Hall-effect sign reversal in $CaRuO_3$ and $SrRuO_3$ thin films," *Phys. Rev. B,* vol. 54, pp. 8996-8999, 1996.

[117] H. Liu, *et al.*, "Twinning rotation and ferroelectric behavior of epitaxial $BiFeO_3$(001) thin films," *App. Phys. Lett.*, vol. 96, p. 012901, 2010.

[118] R. J. Zeches, *et al.*, "A strain-driven morphotropic phase boundary in $BiFeO_3$," *Science,* vol. 326, pp. 977-980, 2009.

[119] A. J. Hatt, *et al.*, "Strain-induced isosymmetric phase transition in $BiFeO_3$," *Phys. Rev. B,* vol. 81, p. 054109.

[120] H. Liu, *et al.*, "Origin of a tetragonal $BiFeO_3$ phase with a giant c/a ratio on $SrTiO_3$ substrates," *Adv. Funct. Mater.*, vol. 22, pp. 937-942, 2012.

[121] Powder diffraction data 2. PDF# 01-071-2494.

[122] S. E. Lofland, *et al.*, "Epitaxy, texturing, and second-harmonic generation in $BiFeO_3$ thin films," *Phy. Rev. B,* vol. 73, p. 092408, 2006.

[123] X. Qi, *et al.*, "Ferroelectric properties and dielectric responses of multiferroic $BiFeO_3$ films grown by RF magnetron sputtering," *J. Phys. D: Appl. Phys.*, vol. 41, p. 232001, 2008.

[124] H. Ma, *et al.*, "Strain effects and thickness dependence of ferroelectric properties in epitaxial $BiFeO_3$ thin films," *App. Phys. Lett.*, vol. 92, p. 182902, 2008.

[125] D. Viehland, "Effect of uniaxial stress upon the electromechanical properties of various piezoelectric ceramics and single crystals," *J. Am. Ceram. Soc.*, vol. 89, pp. 775-785, 2006.

[126] O. Lohse, *et al.*, "Relaxation mechanism of ferroelectric switching in Pb(Zr,Ti)O_3 thin films," *J. Appl. Phys.*, vol. 89, pp. 2332-2336, 2001.

[127] G. W. Pabst, *et al.*, "Leakage mechanisms in $BiFeO_3$ thin films," *Appl. Phys. Lett.*, vol. 90, p. 72902, 2007.

[128] S. K. singh, *et al.*, "Enhanced polarization and reduced leakage current in $BiFeO_3$ thin films fabricated by chemical solution deposition," *J. Appl. Phys.*, vol. 100, p. 064102, 2006.

[129] V. P. Afanasjev, *et al.*, "Polarization and self-polarization in thin $PbZr_{1-x}Ti_xO_3$ (PZT) films," *J. Phys., Condens. Matter.*, vol. 13, pp. 8755-8763, 2001.

[130] B. O'Regan and M. Gratzel, "Low-cost, high-efficiency solar cell based on dye-sensitized colloidal TiO_2 films," *Nature*, vol. 353, pp. 737-740, 1991.

[131] A. Luque, *et al.*, "Solar cells based on quantum dots: multiple exciton generation and intermediate bands," *MRS Bulletin*, vol. 32, pp. 236-241, 2007.

[132] L. Pintilie, *et al.*, "Short-circuit photocurrent in epitaxial lead zirconate-titanate thin films," *J. Appl. Phys.*, vol. 101, p. 064109, 2007.

[133] I. Pintilie, *et al.*, "Ferroelectric polarization-leakage current relation in high quality epitaxial Pb(Zr,Ti)O_3 films," *Phy. Rev. B*, vol. 75, p. 104103, 2007.

[134] S. Zafar, *et al.*, "The electronic conduction mechanism in barium strontium titanate thin films," *Appl. Phys. Lett.*, vol. 73, pp. 3533-3535, 1998.

[135] S. J. Clark and J. Robertson, "Band gap and Schottky barrier heights of multiferroic $BiFeO_3$," *Appl. Phys. Lett.*, vol. 90, p. 132903, 2007.

[136] F. Zheng, *et al.*, "Separation of the Schottky barrier and polarization effects on the photocurrent of Pt sandwiched $Pb(Zr_{0.20}Ti_{0.80})O_3$ films," *Appl. Phys. Lett.*, vol. 93, p. 172101, 2008.

[137] A. Anikiev, *et al.*, "Perturbed polariton spectra in optically damaged $LiNbO_3$," *Ferroelectr. Lett. Sec.*, vol. 3, pp. 89-96, 1985.

[138] B. Sturman, *et al.*, "Light-induced charge transport in $LiNbO_3$ crystals," *Phys. Rev. Lett.*, vol. 78, p. 245114, 2008.

[139] W. Eerenstein, *et al.*, "Experimental difficulties and artefacts in multiferroic and magnetoelectric thin films of $BiFeO_3$, $Bi_{0.6}Tb_{0.3}La_{0.1}FeO_3$ and $BiMnO_3$," *Philos. Mag. Lett.*, vol. 87, pp. 249-257, 2007.

[140] T.-H. Yang, *et al.*, "Promising electron field emitters composed of conducting perovskite $LaNiO_3$ shells on ZnO nanorod arrays," *J. Mater. Chem.,* vol. 22, pp. 17071-17078, 2012.

[141] X. Wang, *et al.*, "Transparent, conductive graphene electrodes for dye-sensitized solar cells," *Nano Lett.,* vol. 8, pp. 323-327, 2007.

[142] J. Jia, *et al.*, "Experimental observation on the Fermi level shift in polycrystalline Al-doped ZnO films " *J. Appl. Phys.,* vol. 112, p. 013718, 2012.

[143] Y. Zang, *et al.*, "Enhanced photovoltaic properties in graphene/polycrystaline $BiFeO_3$/Pt heterojunction structure," *App. Phys. Lett.,* vol. 99, p. 132904, 2011.

[144] S. Y. Yang, *et al.*, "Photovoltaic effects in $BiFeO_3$," *Appl. Phys. Lett.,* vol. 95, p. 062909, 2009.

[145] B. Kundys, *et al.*, "Light-induced size changes in $BiFeO_3$ crystals," *Nat. Mater.,* vol. 9, pp. 803-805, 2010.

[146] W. Ji, *et al.*, "Bulk photovoltaic effect at visible wavelength in epitaxial ferroelectric $BiFeO_3$ thin films," *Adv. Mater.,* vol. 22, pp. 1763-1766, 2010.

[147] R. E. Newnham, *Properties of materials: anistropy, symmetry, structure*. Oxford: Oxford University Press, 2005.

[148] M. Ichiki, *et al.*, "Photovoltaic effect of crystalline-oriented lead lanthanum zirconate titanate in layered film structure," *Jpn. J. Appl. Phys.,* vol. 45, pp. 9115-9118, 2006.

[149] S. R. Kim and S. K. Choi, "Effects of grain size and doping on photovoltaic current in (Pb1-xLax)TiO3 ferroelectric ceramics," *Ferroelectr. Lett.,* vol. 31, pp. 63-72, 2004.

[150] M. Qin, *et al.*, "Stability of photovoltage and trap of light-induced charges in ferroelectric WO_3-doped $(PbLa)(ZrTi)O_3$ thin films," *Appl. Phys. Lett.,* vol. 91, p. 092904, 2007.

[151] Y. Yuan, *et al.*, "Efficiency enhancement in organic solar cells with ferroelectric polymers," *Nat. Mater.,* vol. 10, 2011.

[152] D. Cao, *et al.*, "High-efficiency ferroelectric-film solar cells with an n-type Cu_2O cathode buffer layer," *Nano Lett.,* vol. 12, pp. 2803-2809, 2012/06/13 2012.

[153] J. Kreisel, *et al.*, "A photoferroelectric material is more than the sun of its parts," *Nat. Mater.,* vol. 11, p. 260, 2012.

[154] T. Qi, *et al.*, "Band-gap engineering via local environment in complex oxides," *Phys. Rev. B,* vol. 83, p. 224108, 2011.

[155] B. Xu, *et al.*, "Design of a low band gap oxide ferroelectric: $Bi_6Ti_4O_{17}$," *EPL,* vol. 94, p. 37006, 2011.

[156] M. G. Walter, *et al.*, "Solar water splitting cells," *Chem. Rev.,* vol. 110, pp. 6446-6473, 2010.

[157] D. E. Scaife, "Oxide semiconductors in photoelectrochemical conversion of solar energy," *Sol. Energy,* vol. 25, pp. 41-54, 1980.

[158] Y. Xu and M. A. A. Schoonen, "The absolute energy positions of conduction and valence bands of selected semiconducting minerals," *Am. Mineral.,* vol. 85, pp. 543-556, 2000.

[159] W. C. Yang, *et al.*, "Polarization-dependent electron affinity of $LiNbO_3$ surfaces," *App. Phys. Lett.,* vol. 85, pp. 2316-2318, 2004.

[160] Y. Inoue, "Photocatalytic water splitting by RuO_2-loaded metal oxides and nitrides with d^0- and d^{10} -related electronic configurations," *Energy Environ. Sci.,* vol. 2, pp. 364-386, 2009.

[161] J. Deng, *et al.*, "Bismuth iron oxide nanoparticles as photocatalyst for solar hydrogen generation from water," *J. Fund. Renew. Energ. Appl.,* vol. 1, pp. 1-10, 2011.

[162] Y. K. Kim, *et al.*, "Reversible plasma switching in epitaxial BiFeO3 thin films," *App. Phys. Lett.,* vol. 96, p. 202902, 2010.

[163] M. Alexe, "Local mapping of generation and recombination lifetime in $BiFeO_3$ single crystals by scanning probe photoinduced transient spectroscopy," *Nano Lett.,* vol. 12, pp. 2193-2198, 2012.